

THE UNIVERSITY OF CALGARY

Characterization of Composite Photocatalysts

by

Elena Vaisman

A THESIS

SUBMITTED TO THE FACULTY OF GRADUATE STUDIES

IN PARTIAL FULFILMENT OF THE REQUIREMENTS

FOR THE DEGREE OF MASTER OF SCIENCE

DEPARTMENT OF CHEMISTRY

CALGARY, ALBERTA

DECEMBER, 1999

© Elena Vaisman 1999



National Library  
of Canada

Acquisitions and  
Bibliographic Services

395 Wellington Street  
Ottawa ON K1A 0N4  
Canada

Bibliothèque nationale  
du Canada

Acquisitions et  
services bibliographiques

395, rue Wellington  
Ottawa ON K1A 0N4  
Canada

*Your file Votre référence*

*Our file Notre référence*

The author has granted a non-exclusive licence allowing the National Library of Canada to reproduce, loan, distribute or sell copies of this thesis in microform, paper or electronic formats.

The author retains ownership of the copyright in this thesis. Neither the thesis nor substantial extracts from it may be printed or otherwise reproduced without the author's permission.

L'auteur a accordé une licence non exclusive permettant à la Bibliothèque nationale du Canada de reproduire, prêter, distribuer ou vendre des copies de cette thèse sous la forme de microfiche/film, de reproduction sur papier ou sur format électronique.

L'auteur conserve la propriété du droit d'auteur qui protège cette thèse. Ni la thèse ni des extraits substantiels de celle-ci ne doivent être imprimés ou autrement reproduits sans son autorisation.

0-612-49661-9

**Canada**

## ABSTRACT

High photocatalytic activity of titanium oxide supported on the zeolite ZSM-5 is correlated with physical characteristics of the composite photocatalyst including the nature of bonding between  $\text{TiO}_2$  and a zeolite; the character and structure of a photoactive site; and the distribution of photocatalytic sites over the particle. The physical state of the titanium oxide supported on ZSM-5 zeolites is characterized by Solid State Nuclear Magnetic Resonance Spectroscopy, Energy Filtered Transmission Electron Microscopy, Scanning Electron Microscopy, the powder X-ray Diffraction method, and Brunauer, Emmett, and Teller (BET) surface area measurement.

A combination of  $^{29}\text{Si}$  single-pulse Magic Angle Spinning and Cross Polarization NMR experiments is used to quantitatively measure Si-O-Ti bonds on the surface of the composite photocatalyst. The measured coverage by 2.5 wt. %  $\text{TiO}_2$  (equal to 16-18% of the BET surface area) is in good correlation with calculated theoretical monolayer of anatase for this loading level (10% to 20% of the BET surface depending upon the orientation of the anatase unit cell). Loading  $\text{TiO}_2$  above 2.5 wt. % leads to the preferential growth of the titania phase without further increase of the coverage of the surface until a critical loading level is achieved. Formation of the anatase-like phase is registered by XRD at 10 wt. % loading. Energy filtered TEM shows that  $\text{TiO}_2$  growth occurs at irregularities on the ZSM-5 surface.

Photocatalytic activity of the composite photocatalysts is studied with the photodegradation of acetophenone. The rate of the reaction is independent of the loading levels of  $\text{TiO}_2$  but varies with different initial acetophenone concentration. Secondary photolysis is considered to play an important role in the overall rate of the reaction.

Present research, based on  $\text{TiO}_2$  photocatalysis, is applied for the treatment of effluents from the pulp and paper industry. The experiments show that the specially designed UC-210 catalyst produces significant color reduction and almost complete photodegradation of organic matter (up to 93%) at a reasonable time interval corresponding to 10 hours of full sun exposure.

## **Acknowledgments**

This work was supported in part by funds from Sustainable Forest Management Network centers of excellence and by grant from the National Sciences and Engineering Research Council of Canada. The collaboration with Trojan Technologies has been very valuable.

Thanks are due to Dr. Cooper H. Langford who generously provided his guidance, advice, and assistance at all times and made the project a challenge and delight. I am very grateful to Dr. Alex Starosud without whose help I probably would have never been able to bring this project to paper and who supported and encouraged me in many ways. I was also very fortunate to have the assistance of Dr. Robert Cook who has shared his knowledge, discussed ideas, and answered all my questions, whose enthusiasm and support for the project provided many great moments.

Particular thanks are owed to Dr. Raghav Yamdagni who provided stimulating discussions and helpful comments during the course of my project. I am also very grateful to Ms. Qiao Wu, and Dorothy Fox for their technical assistance in nuclear magnetic resonance analysis.

Among those I wish to acknowledge are all the Langfordites who provided valuable friendship during my stay at the University of Calgary. I would also like to extend my appreciation to Miss Greta Prihodko, departmental secretary, for her enthusiastic care and kind help in administration.

*To my family*

## TABLE OF CONTENTS

<b>Approval page</b> .....	ii
<b>Abstract</b> .....	iii
<b>Acknowledgments</b> .....	iv
<b>Dedication</b> .....	v
<b>Table of contents</b> .....	vi
<b>List of Figures</b> .....	ix
<b>List of Tables</b> .....	xii
<b>Chapter One: Introduction</b> .....	1
<b>Chapter Two: Theory</b> .....	5
2.1. Principles of photocatalysis.....	5
2.2. Kinetic studies.....	6
2.3. NMR theory .....	8
2.3.1. Classical mechanics description of nuclei.....	9
2.3.2. Quantum mechanics description of nuclei.....	10
2.3.3. Behavior of a nuclear spin in a magnetic field.....	12
2.3.4. A macroscopic sample in a magnetic field.....	15
2.3.5. The resonance phenomenon.....	16
2.3.6. Rotating axis system.....	18
2.3.7. Chemical shielding, dipole-dipole interaction and spin-spin coupling.....	19
2.3.8. Saturation of the spin system and relaxation processes.....	24
2.3.9. The NMR signal and Bloch equations.....	28
2.3.10. The intensity of an NMR signal.....	32
2.3.11. Fourier transform NMR spectroscopy.....	32
2.4. Solid state NMR theory.....	37
2.4.1. Magic Angle Spinning.....	38
2.4.2. Cross Polarization.....	39
2.5. EFTEM Theory.....	46

<b>Chapter Three: Examination of Physical State of TiO<sub>2</sub> Photocatalyst on the Zeolite Support by CP MAS NMR, XRD, and BET Methods.....</b>	<b>52</b>
3.1. Introduction.....	52
3.2. Experimental Section.....	53
3.2.1. Materials.....	53
3.2.2. Sample Preparation.....	53
3.2.3. Procedures.....	54
3.3. Results.....	56
3.3.1. Solid State <sup>29</sup> Si NMR spectroscopy.....	57
3.3.2. XRD analysis.....	63
3.3.3. BET analysis.....	64
<b>Chapter Four: Investigation of Distribution of Titania over the Surface of the Zeolite by SEM and EFTEM Techniques.....</b>	<b>67</b>
4.1. Introduction.....	67
4.2. Apparatus.....	67
4.2.1. Scanning Electron Microscopy.....	67
4.2.2. Energy Filtered Transmission Electron Microscopy.....	68
4.3. Results.....	68
4.3.1. SEM analysis.....	68
4.3.2. EFTEM.....	69
<b>Chapter Five: Correlation of Physical Characteristics of TiO<sub>2</sub> with Its Photoactivity.....</b>	<b>73</b>
5.1. Introduction.....	73
5.2. Experimental.....	73
5.2.1. Chemicals.....	73
5.2.2. Photocatalytic procedure.....	74
5.2.3. Analytical determination of acetophenone by HPLC and GC.....	75
5.3. Dark adsorption of acetophenone on the supported catalyst.....	76
5.4. Light intensity measurements by ferrioxalate actinometry.....	78

5.5. Photoactivity of TiO <sub>2</sub> supported on ZSM-5.....	80
<b>Chapter Six: Application of Supported Photocatalyst for Oxidation of Organics and Decolorization of Pulp Mill Effluents.....</b>	<b>84</b>
6.1. Introduction.....	84
6.2. Experimental Section.....	85
6.2.1. Materials.....	85
6.2.2. Photolysis procedures.....	86
6.2.3. Analytical methods.....	86
6.3. Results.....	87
6.3.1. Qualitative evaluation using rotating tube reactor.....	87
6.3.2. Product analysis of output from flow reactor.....	90
6.4. Conclusion.....	90
<b>Chapter Seven: Conclusion.....</b>	<b>103</b>
<b>References.....</b>	<b>105</b>
<b>Appendix.....</b>	<b>109</b>

## List of Figures

### Chapter Two

<b>Fig. 2-1.</b> Creation of electron-hole pair in the illuminated TiO <sub>2</sub> and subsequent photocatalytic reactions.....	5
<b>Fig. 2-2.</b> Various representations of nuclei.....	11
<b>Fig. 2-3.</b> Precession of a nuclear moment in an applied field of strength $B_0$ .....	14
<b>Fig. 2-4.</b> Nuclear energy levels ( $I = \frac{1}{2}$ ).....	14
<b>Fig. 2-5.</b> Application of the rotating magnetic field $B_1$ on the magnetization of the sample showing the torque, $F$ , turning $M$ away from $B_0$ .....	17
<b>Fig. 2-6.</b> The dependence of $T_1$ and $T_2$ on the correlation time $\tau_c$ .....	27
<b>Fig. 2-7.</b> The absorption, $M_y$ , and dispersion, $M_x$ , components of the nuclear magnetization as a function of frequency.....	31
<b>Fig. 2-8.</b> The action of r.f. pulses with $\phi = \pi/2$ .....	34
<b>Fig. 2-9.</b> A plot of change in the magnetization with time.....	35
<b>Fig. 2-10.</b> A single pulse of r.f. radiation in a) time domain and b) frequency domain.....	36
<b>Fig. 2-11.</b> A free induction decay curve (a) and its Fourier transform (b). The dashed line corresponds to the resonance condition and the solid line to the off-resonance condition.....	37
<b>Fig. 2-12.</b> The pulse sequence for CP experiment.....	41
<b>Fig. 2-13.</b> The geometry of energy loss spectroscopy in the electron microscope illustrating the scattering angle $\phi$ and the spectrometer acceptance angle $\Omega$ .....	47
<b>Fig. 2-14.</b> An image of TiO <sub>2</sub> thin film. $E_0=200\text{kV}$ , $I_0 = 6.2 \times 10^8$ , $\theta = 100 \text{ mrad}$ ...	48
<b>Fig. 2-15.</b> Diagram of Zeiss 902 column showing prism-mirror-prism filter, energy selecting slit, and CCD detector. The solid line indicates the path along the optical axis of the system followed by electrons with 0 eV loss ( elastic scatter). The dashed line is a representative path for an electron with an energy loss.....	51

### Chapter Three

<b>Fig. 3-1.</b> Binding of titanium oxide onto the zeolite surface.....	54
<b>Fig. 3-2.</b> CPMAS contact time optimization done at BL7 probe spun at 2 kHz with D1=7s, DL0=10.8db, TL0=20.9db.....	55
<b>Fig. 3-3.</b> Solid State <sup>29</sup> Si NMR spectra of ZSM-5, a) 90° pulse sequence, b) <sup>29</sup> Si- <sup>1</sup> H cross-polarization.....	59
<b>Fig. 3-4.</b> Dependence of relative intensities of signals on contact time, a) 1ms, b) 7ms.....	60
<b>Fig. 3-5.</b> CPMAS spectra of a) pure ZSM-5 (SiO <sub>2</sub> /Al <sub>2</sub> O <sub>3</sub> =50), b) 2.5 wt. % TiO <sub>2</sub> , c) 5 wt. % TiO <sub>2</sub> , d) 10% TiO <sub>2</sub> .....	61
<b>Fig. 3-6.</b> CPMAS spectra of a) pure ZSM-5 (SiO <sub>2</sub> /Al <sub>2</sub> O <sub>3</sub> =50), b) pure ZSM-5 (SiO <sub>2</sub> /Al <sub>2</sub> O <sub>3</sub> =280), c) ZSM-5 (SiO <sub>2</sub> /Al <sub>2</sub> O <sub>3</sub> =280) loaded with 2.5 wt. % TiO <sub>2</sub> .....	62
<b>Fig. 3-7.</b> X-ray powder diffraction patterns of a) TiO <sub>2</sub> calcined at 450°, b) 10 wt. % TiO <sub>2</sub> , c) 2.5 wt. % TiO <sub>2</sub> , d) pure ZSM-5 (SiO <sub>2</sub> /Al <sub>2</sub> O <sub>3</sub> =50) .....	65
<b>Fig. 3-8.</b> Surface area measurements of ZSM-5 (Si/Al=50) with different titania loading.....	66

### Chapter Four

<b>Fig. 4-1.</b> X-ray emission spectra of 2.5 wt. % TiO <sub>2</sub> taken at a representative 3×3 mm particle (a), and at its different spots (b), (c), (d).....	70
<b>Fig. 4-2.</b> X-ray emission spectra of 10 wt. % TiO <sub>2</sub> taken at a representative 3×3 mm particle (a), and at its different spots (b), (c), (d).....	71
<b>Fig. 4-3.</b> EFTEM picture of 2.5 wt. % TiO <sub>2</sub> loaded on ZSM-5 (SiO <sub>2</sub> /Al <sub>2</sub> O <sub>3</sub> =50 ) where 1) and 2) are two pre-edge reference images, 3) the post-edge Ti-enhanced image, and 4) the net Ti image after background subtraction and integration of the ionization edge intensity.....	72

### Chapter Five

<b>Fig. 5-1.</b> The absorption spectrum of acetophenone in water at 100 ppm demonstrating that a 320 nm cut off filter prevents direct excitation.....	75
<b>Fig. 5-2.</b> Calibration of HPLC for analysis of acetophenone.....	76
<b>Fig. 5-3.</b> Calibration of GC for analysis of acetophenone.....	76

<b>Fig. 5-4.</b> Dark adsorption isotherm of acetophenone on different zeolites.....	78
<b>Fig. 5-5.</b> Photodegradation of acetophenone by TiO <sub>2</sub> (P25). Initial concentration of acetophenone was 50ppm, mass of the catalyst - 2g/L.....	81
<b>Fig. 5-6.</b> Photoactivity of titania supported on ZSM-5 (SiO <sub>2</sub> /Al <sub>2</sub> O <sub>3</sub> =50). Initial concentration of acetophenone was 120 ppm.....	82
<b>Fig. 5-7.</b> Dependence of the extent of acetophenone photodegradation on its initial concentration.....	83
<b>Chapter Six</b>	
<b>Fig. 6-1.</b> HPLC chromatograms showing photolysis products of MWW after 1 and 3 days in the rotating tube with 0.5 g of UC-210.....	92
<b>Fig. 6-2.</b> HPLC chromatograms showing photolysis products of MWW under rotating irradiation with different loading of UC-210 after 10 days.....	93
<b>Fig. 6-3.</b> HPLC chromatograms showing photolysis products of MWW with 0.5 % H <sub>2</sub> O <sub>2</sub> after 1 and 10 days under rotating irradiation.....	94
<b>Fig. 6-4.</b> HPLC chromatograms showing photolysis products of MWW with 0.5 g UC-210 and 0.5 % H <sub>2</sub> O <sub>2</sub> after 1 day under rotating irradiation.....	95
<b>Fig. 6-5.</b> HPLC chromatograms showing photolysis products of MWW with 0.5 g UC-210 and 0.5 % H <sub>2</sub> O <sub>2</sub> after 2 days under rotating irradiation.....	96
<b>Fig. 6-6.</b> HPLC chromatograms showing photolysis products of MWW with 0.5 g UC-210 and 0.5 % H <sub>2</sub> O <sub>2</sub> after 6 days under rotating irradiation.....	97
<b>Fig. 6-7.</b> HPLC chromatograms showing photolysis products of MWW under rotating irradiation with UC-210 and different % H <sub>2</sub> O <sub>2</sub> after 8 days .....	98
<b>Fig. 6-8.</b> HPLC chromatograms showing photolysis products of MWW with 0.5 g UC-210 and everyday injections of 0.5 % H <sub>2</sub> O <sub>2</sub> after 4 days under rotating irradiation.....	99
<b>Fig. 6-9.</b> HPLC chromatograms showing photolysis products of MWW with 0.5 g UC-210 and everyday injections of 0.5 % H <sub>2</sub> O <sub>2</sub> for the first 4 days and without injections for the last 4 days under rotating irradiation.....	100
<b>Fig. 6-10.</b> HPLC chromatograms showing photolysis products of MWW with 0.2 g UC-210 or Degussa P25 and 0.5 % H <sub>2</sub> O <sub>2</sub> after 2 days under rotating irradiation.	101

<b>Fig. 6-11.</b> HPLC chromatograms showing photolysis products of MWW with 0.2 g UC-210 or Degussa P25 and 0.5 % H <sub>2</sub> O <sub>2</sub> after 11 days under rotating irradiation.....	102
--	-----

**List of Tables**

<b>Table 3-1.</b> Quantitative estimation of “surface Si-OH groups” relative to the kaolinite standard (STD) as the ratio of the -104 ppm peak to the -93 ppm peak....	63
<b>Table 5-1.</b> Adsorption of acetophenone on a composite catalyst (2.5 wt.% TiO <sub>2</sub> - Zeolite) supported on different zeolites. Initial concentration of acetophenone solution was equal 128 ppm.....	77
<b>Table 6-1.</b> Analyses of samples from treatment of Mill White Water from Howe Sound mill in flow reactor for 96 h.....	91

## Chapter One

### Introduction

In XIX century when Pasteur discovered that contaminated water was a cause of many infectious diseases, local municipalities were charged by law to provide pure drinking water to their inhabitants, and to collect and treat wastewater. Since then, water pollution has become a serious global problem. Rivers, lakes, and other reservoirs from which water is abstracted are being polluted by industrial sources such as mining, steel production, the generation of electricity and chemical production; municipal wastewater effluents, domestic wastes, agricultural spraying, and accidents such as oil or chemical spills and contaminated sites. In order to make water potable for consumption, the removal of natural, man-made and synthetic pollutants is necessary. Water quality is regulated stringently by minimum standards related to microbiological, chemical, and physical properties. The Government of Canada is addressing water quality concerns through various actions, including a renewed and strengthened Canadian Environmental Protection Act (CEPA) and the development of a Federal Freshwater Strategy.<sup>1,1</sup>

Currently, several processes are being used for the decontamination of water. The oxidation of organic pollutants in water is often preferred over the other methods or successfully used in combination with them. For example, such chemicals as pesticides, insecticides, and chlorinated organics are difficult to decompose by biodegradation through bacteria. At the same time, oxidation technologies offer an efficient and competitive alternative treatment since it has the potential to convert the organics to environmentally acceptable products such as carbon dioxide and chloride leaving no residuals requiring further handling<sup>1,2-1,4</sup>. Thus, concern over secondary waste production, such as solid or gas-phase residuals, is relieved.

Recently, the photoredox reactions on semiconductor catalysts, such as ZnO, CdS, Fe<sub>2</sub>O<sub>3</sub>, WO<sub>3</sub>, and others have been the subject of attention<sup>1,5</sup>. In particular, TiO<sub>2</sub> is the semiconductor material with the most promise for the photocatalysis<sup>1,6-1,8</sup>. It exhibits very strong oxidation potential in the presence of oxygen when irradiated by UV or

sunlight. It also has many practical advantages: it is inexpensive, relatively non-toxic, and stable, i.e. it does not dissolve or corrode under photooxidation.

In the effort to develop photocatalysts based on  $\text{TiO}_2$ , a great deal of recent research have been devoted to investigation of supported  $\text{TiO}_2$  catalysts<sup>1 9-1.14</sup>. Our efforts are directed towards the development of an integrated photocatalyst-adsorbent matrix suitable for practical applications. The integrated matrix approach combines adsorption with advanced oxidation by photocatalysis. It also introduces the way of regeneration of the adsorbent by photochemical oxidation of the organics adsorbed.  $\text{TiO}_2$  presents a very polar surface to an aqueous medium. Water is more strongly adsorbed than a typical organic contaminant. One of the key properties sought from a support is to provide a hydrophobic surface which adsorbs organics. When the photocatalyst is attached to the adsorbent, there is an additional opportunity to gain in photocatalytic efficiency since the problem of encounter of substrate with the photoactive site is reduced from a three-dimensional to a two-dimensional diffusion problem.

Among various supports for  $\text{TiO}_2$  photocatalysts, the zeolites family seems to be among the most attractive candidates. High silica zeolites provide capacity to adsorb organic contaminants from aqueous streams with subsequent "regeneration" of the adsorbent. Maximal photocatalytic activity was observed earlier<sup>1 15</sup> at low  $\text{TiO}_2$  loading (2.5 wt. %) on the highly siliceous zeolite ZSM-5. This result was achieved in a mainly empirical exploration of various supports, such as silica, glass, alumina, and zeolites.

The suggested explanation of the relatively high efficiency at a low titania loading was that the support can affect the activity of titanium oxide by modification of its structure in the thin films. Combined results of X-ray powder diffraction (XRD), Scanning Electron Microscopy (SEM), and Raman spectroscopy support the conclusion that Ti is not substituted into tetrahedral Si sites of the zeolite, but is anchored on the outer surface as small particles of  $\text{TiO}_2$  (microcrystalline or amorphous) related to anatase<sup>1.16</sup>. High activity of {2.5 wt. %  $\text{TiO}_2$  +ZSM-5} system implies that  $\text{TiO}_2$  absorbs all incident photons at a lower loading than is the case for  $\text{TiO}_2$  alone and that the adsorbed substrate can efficiently reach these light-activated sites. Efficient access to photoactive species by the substrate means that the support itself doesn't prevent

absorption of light by titania. However, controlling factors of high photoactivity remained incompletely elucidated, and structural studies, done before, didn't provide detailed description of the nature of the surface at titanium oxide loading lower than that leading to formation of anatase crystals.

In order to further elucidate high titania activity at a low loading and to manipulate such a system, it is necessary to better understand the physical characteristics of composite  $\text{TiO}_2$  photocatalysts and correlate physical parameters with catalytic activity. Some of the fundamental issues, which require careful examination, include the nature of bonding, which can occur between a  $\text{TiO}_2$  film on the surface and a zeolite surface; the character and structure of a photoactive site; and the distribution of photocatalytic sites over the particle.

Present study describes examination of composite  $\text{TiO}_2$  photocatalysts using Solid State  $^{29}\text{Si}$  Nuclear Magnetic Resonance (NMR) and Energy Filtered Transmission Electron Microscopy (EFTEM). More conventional methods, such as Powder X-ray Diffraction, Scanning Electron Microscopy, and the BET method for surface area measurement, have also been used when applicable.

Solid State NMR is well suited to establish microenvironment of different Si nuclei in zeolites. Moreover, in all highly siliceous materials, including ZSM-5 zeolite, aluminum content is so low that it doesn't affect the  $^{29}\text{Si}$  spectrum. Consequently, the observed resonances are due to only  $\text{Si}[\text{OSi}]_4$  groups and are extremely narrow<sup>1,17</sup>. These spectra can be exploited in a number of ways to obtain information regarding their structure that is not easily obtainable by other techniques. For example, a combination of  $^{29}\text{Si}$  single-pulse Magic Angle Spinning (MAS) and Cross Polarization (CP) experiments was used to characterize the external surface of zeolite MAP and to elucidate its structure with respect to the bulk<sup>1,18</sup>.

In addition to the NMR method, Energy Filtered Transmission Electron Microscopy (EFTEM) technique was used to image cross-sections of micron-size zeolite and to establish the distribution of titanium oxide on the surface. Energy filtered images contain both mass-density and elemental information that can be recorded for elemental distribution maps. This technique was used for mapping various elements<sup>1,19</sup>. EFTEM

technique is known to be two orders of magnitude better than X-ray microanalysis in the scanning electron microscope<sup>1,20</sup>.

The photocatalytic activity of titanium oxide, supported on ZSM-5, was investigated in order to correlate it with physical characteristics of the composite photocatalyst. Photodegradation of acetophenone was chosen as a test reaction. The rate of the reaction was investigated as a function of different loading levels of titania on the zeolite and the concentration of acetophenone in the solution. A parallel unsupported TiO<sub>2</sub> (P25) powder was also used throughout the study to compare with the supported samples. Relative adsorption capacities of the catalysts supported on the zeolites used in this work were estimated.

Finally, the composite TiO<sub>2</sub> photocatalyst was applied for the treatment of synthetic and "real" effluent streams from the Pulp and Paper Mill Industry. Photocatalytic experiments were conducted using different schemes including photocatalysis alone as well as in a combination with UV / H<sub>2</sub>O<sub>2</sub> scheme.

## Chapter Two

### THEORY

#### 2.1. Principles of titanium dioxide photocatalysis

The theory of photochemical processes which occur upon irradiation of semiconductors are now well established.  $\text{TiO}_2$  may be regarded as a wide band gap semiconductor. Solid state quantum physics that considers electrons as complex waves obeying interference phenomenon in a periodic potential field of crystalline material, introduced the concept of allowed energy bands and forbidden energy gaps for the electron<sup>2,1</sup>. The lower energy region is the valence band with binding electrons and the higher region is the conduction band with free ( in a first approximation ) electrons which can produce conductivity similar to that of metals. Between these two bands is a forbidden bandgap. An electron can be photoexcited to the conduction band when the absorption of radiation with energy equal or greater than the band gap occurs. The absence of the electron in the valence band produces an electron vacancy or hole ( $h^+$ ). Solid  $\text{TiO}_2$ , that has a bandgap energy of 3.0 eV, absorbs light in the near UV, promoting an electron from the valence band (essentially oxide ion orbitals) to the conduction band (essentially Ti ion d-orbitals) as shown in Fig. 2-1.

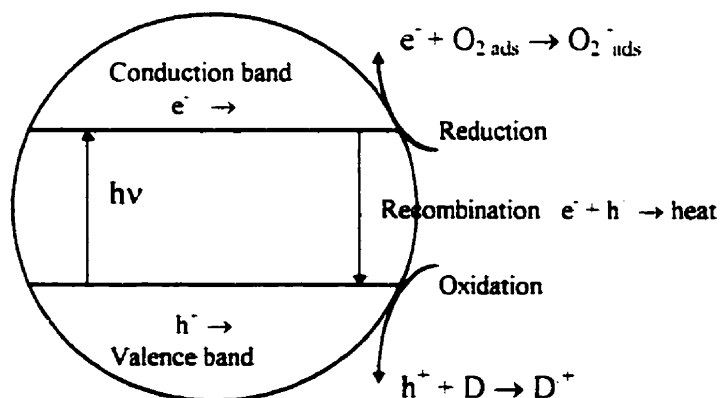


**Fig. 2-1.** Creation of electron-hole pair in the illuminated  $\text{TiO}_2$  and subsequent photocatalytic reactions.

Both carriers can travel to the surface and be trapped at (subsurface lattice oxygen for the hole and  $\text{Ti}^{IV}$  for the electron) or near the particle surface where they can undergo electron transfer reactions across the interface with surface adsorbed electron donors and acceptors from molecules of solution<sup>2,2</sup>. The trapped carriers have effective solution potentials on the hydrogen scale of +3.2 V for the hole and about 0 V for the electron. Thus, the hole is an extremely powerful oxidizing agent and the electron a good reducing agent.

Titanium dioxide is readily hydrated in aqueous solutions (due to partially uncoordinated states of its surface titanium and oxygen atom). The hole can be trapped at the surface where water molecule or hydroxide ion is adsorbed and generate a hydroxyl radical ( $h^{\cdot} + \text{H}_2\text{O}_{\text{ads}} \rightarrow \text{OH}^{\cdot} + \text{H}^+$  or  $h^{\cdot} + \text{OH}^-_{\text{ads}} \rightarrow \text{OH}^{\cdot}$ ). Hydroxyl radicals have been detected in illuminated aqueous  $\text{TiO}_2$  suspensions<sup>2,3-2,5</sup> and are widely believed to be the most important oxidizing species in these systems. The  $\text{OH}^{\cdot}$  radicals that are produced at the surface may attack an organic substrate that is also adsorbed or they may desorb and then react with the organics in the bulk solution ( $\text{RH} + \text{OH}^{\cdot} \rightarrow \text{R}^{\cdot} + \text{HOH}$ )<sup>2,6</sup>. Alternatively, the hole at the surface can directly initiate one electron oxidation of a very wide range of adsorbed organic molecules resulting in the formation of organic radical ( $h^{\cdot} + \text{D} \rightarrow \text{D}^{\cdot+}$ ). The electron is readily captured by  $\text{O}_2$ , adsorbed on the surface, to give the reactive superoxide ion ( $e^- + \text{O}_{2\text{ ads}} \rightarrow \text{O}_2^{\cdot-}_{\text{ ads}}$ ).<sup>2,7</sup>

Trapped carriers may also diffuse from the titania surface into the bulk solution and react at some distance of the solid surface. Hydrogen peroxide can also be formed through various radical reactions<sup>2,8-2,9</sup>. Cleavage of  $\text{H}_2\text{O}_2$  may also result in the formation of  $\text{OH}^{\cdot}$  radicals<sup>2,8</sup>. Thus, the illuminated  $\text{TiO}_2$  is a very attractive catalyst for initiation of oxidation of almost all organic compounds.

## 2.2. Kinetic studies

Most often kinetic data for  $\text{TiO}_2$  are reported as apparent kinetics because of the heterogeneity of the system and adsorption-desorption equilibria which tend to complicate the physical picture of the target organic compound degradation. Most often,

the evaluation of kinetic data and mechanisms involves the use of the Langmuir-Hinshelwood (L-H) model<sup>2,9-2,10</sup>. In this model, the rate limiting reaction in the photocatalytic degradation by titania is assumed to be a surface reaction between species from the solution adsorbed on titania and some oxidizing reagent (e.g. OH<sup>•</sup>), the concentration of which is considered to be constant. Thus, kinetics, in its most general form, can be expressed as a pseudo-first order reaction shown by Eqn (2.2-1)

$$R = \frac{d[C_{ads}]}{dt} = \{k_o[C_{ox}]\} \cdot [C_{ads}] = k[C_{ads}] \quad (2.2-1)$$

where  $C_{ox}$  is a concentration of an oxidizing agent assumed to be constant,  $C_{ads}$  is a concentration of organics adsorbed on the TiO<sub>2</sub> surface,  $k_o$  is a rate constant of the investigated reaction under constant illumination. Since reaction occurs primarily on the surface, further assumptions of the L-H model were made. They include the following: the surface is ideal, i.e. surface adsorption sites are identical, their number is uniform at equilibrium, there is preadsorption equilibrium with only a single substrate bonded at each site thus building a monolayer, that there is no interaction between adjacent adsorbed molecules nor competitive reaction or irreversible inhibition by other substrates (or products) that may be present. In L-H model, the concentration of organic species adsorbed on the TiO<sub>2</sub> surface is expressed as Eqn (2.2-2)

$$[C_{ads}] = \frac{K_{ads}[C]}{1 + K_{ads}[C]} \quad (2.2-2)$$

where  $C$  is the concentration of organics in the bulk at equilibrium, and  $K_{ads}$  is an equilibrium constant of adsorption-desorption process. Combining Eqn (2.2-1) and (2.2-2), the following expression for the rate of the photocatalytic degradation by titania is obtained

$$R = \frac{k_{LH} K_{ads}[C]}{1 + K_{ads}[C]} \quad (2.2-3)$$

where  $R$  is the initial rate of photocatalytic degradation,  $k_{LH}$  is the rate constant for reaction of adsorbed species,  $K_{ads}$  is adsorption-desorption constant, and  $C$  is an initial reactant concentration.

However, this form of rate equation can be derived for a number of different mechanisms. The L-H model was questioned by several authors because of its simplistic assumptions<sup>2.11-2.13</sup>. Some investigators modified it to obtain good correlation for photocatalytic reactions. For example, Serpone<sup>2.14</sup> examined the photocatalyzed oxidation of phenol in irradiated TiO<sub>2</sub> aqueous dispersions and found the interdependence of the rate of the photoreaction on the concentration of phenol and on the incident light intensity. In order to rationalize the photostimulated reactions, the concept of photoinduced surface active centers was applied to kinetic data. However, kinetic studies alone can not distinguish whether photocatalytic oxidation occurs in solution or on the surface. In this work, the rate constant will be used only as a measure of relative efficiency of the investigated reaction under different conditions.

### 2.3. NMR Theory

The basis of NMR is the behavior of the magnetic moments of atomic nuclei under the influence of an external magnetic field and local fields created by the surrounding nuclei and by the electronic charge distribution around the nuclei. The basic theory of NMR is common to all experiments and all nuclei and is applicable to a variety of modern techniques that use different NMR spectrometers. Therefore, there is a necessity to cover briefly the theoretical background in order to better understand more advanced theory of solid state NMR.

Section 2.3., Elementary Aspects of the Theory of NMR, (chapters 2.3.1-2.3.10) includes the key issues of basic NMR pertinent to the present work. This section represents a compilation of materials extracted from reference books and papers 2.15-2.21. The core solid state NMR theory is presented in the section 2.4., Solid State NMR Theory, mainly based on references 2.22 - 2.27.

### 2.3.1. Classical Mechanics Description of Nuclei.

A classical description of NMR starts with angular momentum  $P_{ang}$  associated with rotating mass as given by Eqn (2.3-1)

$$\vec{P}_{ang} = \vec{r} \times m\vec{V} \quad (2.3-1)$$

where  $r$  is the position vector of the particle;  $V$  - is its linear velocity;  $m$  - its mass. The angular momentum is perpendicular to the plane of the circulating mass and the direction of the angular momentum is given by the right hand rule. The magnitude of angular momentum of the particle can be expressed in term of its angular velocity,  $\Omega$  ( $V = \Omega r$ ) as shown by Eqn (2.3-2)

$$P = m\Omega r^2 \quad (2.3-2)$$

Motion of a circulating charge has a magnetic field associated with it. A magnetic moment,  $\mu$ , generated by such motion is given in electromagnetic theory by Eqn (2.3-3)

$$\mu = i \times S = \left( \frac{q \cdot \Omega}{2\pi} \right) \times (\pi \cdot r^2) = \frac{1}{2} q \cdot \Omega \cdot r^2 \quad (2.3-3)$$

where  $i$  is a current producing magnetic field,  $q$  is the circulating charge,  $S$  is its circular orbit. The relationship between angular momentum,  $P_{ang}$ , and magnetic moment,  $\mu$ , can be deduced using equations (2.3-2) and (2.3-3). This relationship is illustrated by Eqn (2.3-4).

$$\mu = \frac{q}{2m} P_{ang} \quad (2.3-4)$$

### 2.3.2. Quantum Mechanical Description of Nuclei.

The expression relating magnetic moment and angular momentum for the circulating charge ( Eqn 2.3-4 ) does not reproduce their relation quantitatively when spin motion is involved. In quantum mechanical theory, Lande factor, or  $g$  - factor, is introduced to take account of this fact. Thus, we write Eqn (2.3-5)

$$\mu = g \frac{q}{2m} P_{ang} \quad (2.3-5)$$

Usually, nuclear magnetic moments are described in terms of magnetogyric ratios,  $\gamma$ , rather than nuclear  $g$ -factors, as shown by Eqn (2.3-6)

$$\mu = \gamma \cdot P_{ang} \quad (2.3-6)$$

Thus,  $g$ -factor includes the charge number and the mass of nucleus itself.

One of the fundamental quantum mechanical postulates is that total angular momentum cannot have any arbitrary magnitude but may only take certain discrete values. Angular momentum is said to be quantized and its magnitude,  $P_{ang}$ , can be specified in terms of spin quantum number  $I$  in units of Planck's constant,  $\hbar$ , by means of Eqn (2.3-7)

$$P_{ang} = \hbar \sqrt{I(I+1)} \quad (2.3-7)$$

Protons and neutron both have a spin quantum number of  $\frac{1}{2}$  in units of  $\hbar$  and, depending on how these particles pair up in the nucleus, the resultant nucleus may or may not have a net non-zero nuclear spin number,  $I$ . If the spins of all the particles are paired, there will be no net spin and the nuclear spin quantum number  $I$  will be zero. This type of nucleus is represented in Fig. 2-2 (a). When  $I = \frac{1}{2}$ , there is one net unpaired spin and it imparts a nuclear magnetic moment,  $\mu$ , to the nucleus. The distribution of the

charge in a nucleus of this type is spherical as shown in Fig. 2-2 (b). When  $I \geq 1$ , the nucleus has spin associated with it and the nuclear charge distribution is non-spherical; see Fig. 2-2 (c). The nucleus is said to possess a quadrupole moment,  $eQ$ , where  $e$  is the unit of electrostatic charge and  $Q$  is a measure of the deviation of the nuclear charge distribution from spherical symmetry.

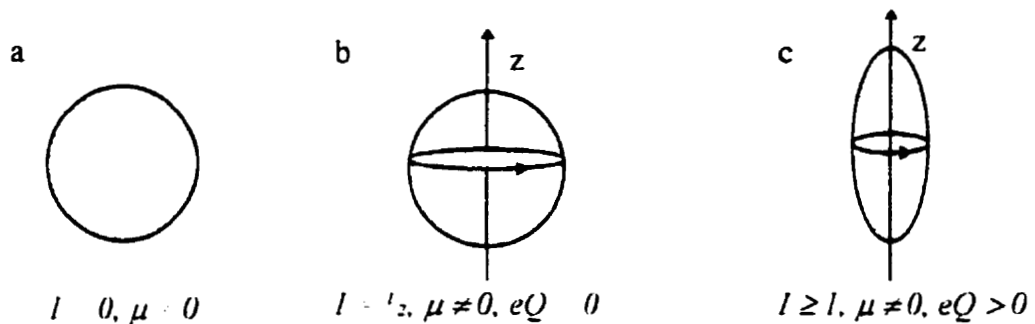


**Fig. 2-2.** Various representation of nuclei.

In order to have a full quantum mechanical description, one should take into consideration not only magnitudes of nuclear angular momentum and magnetic moment but include their directions as well. The allowed orientations of nuclear angular momentum and magnetic moment vectors in a magnetic field are indicated by a magnetic quantum number of the nuclear spin,  $m_I$ , which takes on values  $I, I-1, \dots, (-I+1), -I$ . For example, for  $^1\text{H}$ ,  $^{13}\text{C}$ ,  $^{29}\text{Si}$   $I = 1/2$ ,  $m_I = \pm 1/2$ , that corresponds to alignments of angular momentum and magnetic moment with and opposed to the field.

Eqn (2.3-8) reflects the discrete nature the component of angular momentum,  $P_z$ , along the considered direction,  $z$  which is quantized in terms of magnetic quantum number of nuclear spin,  $m_I$

$$P_z = \hbar m_I \quad (2.3-8)$$

Using Eqn (2.3-6) and Eqn (2.3-8), the component of magnetic moment,  $\mu_z$ , along the direction  $z$  can be given by Eqn (2.3-9)

$$\mu_z = \gamma \cdot P_z = \gamma \hbar m_l \quad (2.3-9)$$

It should be noted that  $g$ -factor can be either positive or negative. Positive  $g$ -factor imply that the spin magnetic moment is parallel to the angular momentum; negative value indicate that  $P_{ang}$  and  $\mu$  are anti-parallel.

### 2.3.3. Behavior of a Nuclear Spin in a Magnetic Field.

In the absence of a magnetic field, there is no preferred direction of the magnetic moment of a nuclear spin, that is, all orientations are degenerate. When a magnetic field of strength  $B_0$  is applied, it exerts a torque,  $\vec{F}_{ang}$  ( a moment of linear force,  $r \times F$  ) on the nuclear moment. This torque is given by the vector ( cross ) product shown by Eqn (2.3-10)

$$\vec{F}_{ang} = \vec{\mu} \times \vec{B}_0 \quad (2.3-10)$$

and can be defined in a Cartesian axis system with  $X$ ,  $Y$  and  $Z$  unit vectors as shown by Eqn (2.3-11)

$$\begin{vmatrix} \vec{X} & \vec{Y} & \vec{Z} \\ \mu_x & \mu_y & \mu_z \\ B_x & B_y & B_z \end{vmatrix} = \vec{X} \cdot (\mu_y B_z - B_y \mu_z) + \vec{Y} \cdot (\mu_z B_x - B_z \mu_x) + \vec{Z} \cdot (\mu_x B_y - B_x \mu_y) \quad (2.3-11)$$

According to Newton's equation of motion applied to rotating particle, the torque,  $\vec{F}_{ang}$ , is equal to the time derivative of the angular momentum,  $P_{ang}$ , as shown by the Eqn (2.3-12)

$$\vec{F}_{\text{avg}} = \frac{d}{dt} P_{\text{avg}} \quad (2.3-12)$$

Combination of Eqn (2.3-6), (2.3-10), and (2.3-12) produces the equation for the precession of the magnetic moment given by Eqn (2.3-13)

$$\frac{d}{dt} \vec{\mu} = \gamma \vec{\mu} \times \vec{B}_0 = -\gamma \vec{B}_0 \times \vec{\mu} \quad (2.3-13)$$

The angular frequency of precession, called Larmor frequency, is given by Eqn (2.3-14)

$$\omega_L = |\gamma| B_0 \quad (2.3-14)$$

The sign of  $\gamma$  determines the sense of the precession.

Eqn (2.3-13) tells us that at any instant the changes in  $\mu$  are perpendicular to both the field  $B_0$  and  $\mu$ . Fig. 2-3 shows that the tip of the vector  $\mu$  is moving out of the paper while the tail of the vector  $\mu$  is fixed. The angle  $\varphi$  that the magnetic moment vector makes with the applied field does not change and  $\mu$ , therefore, generates a cone. In classical mechanical description, it corresponds to Larmor precession about the applied field  $B_0$ . The left hand rule shows that the moment is precessing clockwise.

The energy of the system is given by the scalar product of multiplication of  $\mu$  and  $B_0$  as shown by Eqn (2.3-15)

$$E = -|\mu| \cdot |B_0| \cos \varphi \quad (2.3-15)$$

In the quantum mechanical description, the application of the magnetic field  $B_0$  produces an interaction energy described by a Hamiltonian

$$H = -\mu \cdot B_0 \quad (2.3-16)$$

Pointing the field  $B_0$  along the  $z$ -direction, we can write

$$E = -\mu_z \cdot B_0 = -\gamma \hbar m_l B_0 \quad (2.3-17)$$

Since there are  $(2I + 1)$  allowed orientations of the magnetic moment in a magnetic field, this corresponds to  $(2I + 1)$  non-degenerate energy levels each of which is separated by  $|\gamma \hbar B_0|$ . For a nucleus of spin  $1/2$ , we have  $I = 1/2$ ,  $E = \pm \gamma \hbar B_0 / 2$  as shown in Fig. 2-4.

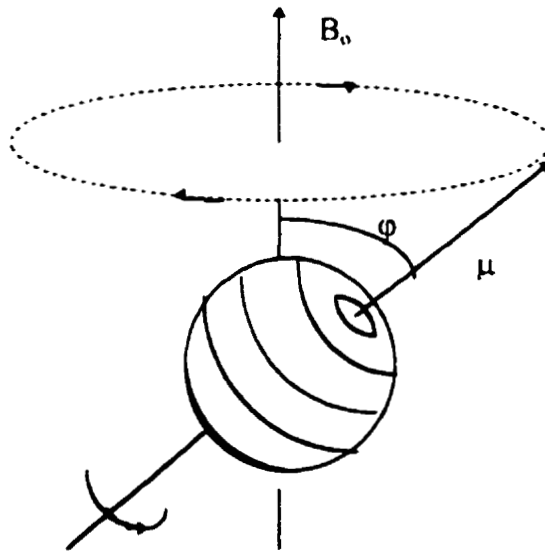


Fig. 2-3. Precession of a nuclear moment in an applied field of strength  $B_0$ .

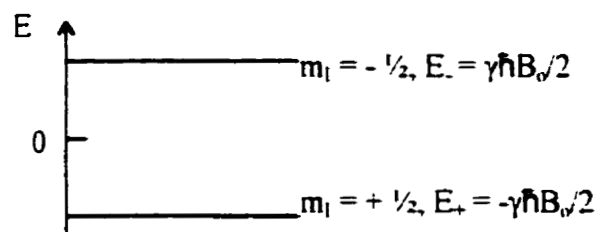


Fig. 2-4. Nuclear energy levels ( $I = 1/2$ )

### 2.3.4. A Macroscopic sample in the magnetic field $B_0$

So far, only the behavior of individual spins has been considered. However, the NMR experiment is done with bulk samples which contain an ensemble of many such spins. The individual moments in the sample add vectorially to give a net magnetization,  $M$  shown in Eqn (2/3-18).

$$\bar{M} = \sum_i \bar{\mu}_i \quad (2.3-18)$$

The magnetization,  $M$ , is affected by magnetic field in the same way as individual magnetic moments, i.e. it will precess. The equation for the motion of precession of net magnetization,  $\bar{M}$ , is similar to Eqn (2.3-13) for a single nuclear spin, i.e.

$$\frac{d}{dt} \bar{M} = -\gamma \bar{B}_0 \times \bar{M} \quad (2.3-19)$$

There are also  $(2I + 1)$  energy levels due to  $(2I + 1)$  values of a magnetic quantum number of  $M$ . The populations of these energy levels of the macroscopic sample can be described using the Boltzmann's distribution expression. For example, if the sample consists of many identical molecules, each with one magnetic nucleus of spin  $I=1/2$ , the populations of two states shown in Fig. 2-5 can be derived using Eqn (2.3-20)

$$N_- / N_+ = \exp(\Delta E / kT) \quad (2.3-20)$$

where  $N_-$  and  $N_+$  are the number of spins in  $E_-$  and  $E_+$  energy levels. Since  $E_-$  is lower in energy than  $E_+$ , there will be an excess population in the lower level at thermal equilibrium. Under normal conditions, the energy difference between the states (see Eqn (2.3-17))  $\Delta E = \gamma \hbar B_0$  is much less than the thermal energy,  $kT$ , therefore, the Eqn (2.3-20) can be regressed to

$$N_- / N_+ \approx 1 - \Delta E / kT \quad (2.3-21)$$

Although the magnetic field usually employed in the NMR experiment is very strong (15-120 kgauss), the excess population in the lower energy level at equilibrium is very low. For example, in the field of 23.5 kgauss at 300 K, it is only 1 in  $10^5$  for protons. It represents only a very small fraction of the maximum possible value which would result for a full alignment of the nuclear moments to the field  $B_0$ . That is the basic reason for the low sensitivity of NMR spectroscopy.

### 2.3.5. The resonance phenomenon.

For detection of the presence of such a set of energy levels (Zeeman splitting), there should be an interaction with some irradiation that can cause transitions between these energy levels. In quantum mechanical terms, there should be an excitation of some nuclei from the lower energy level,  $E_{-}$ , ( Fig. 2-4 ) to the upper level,  $E_{+}$ , via absorption of energy from the external energy source. According to the Bohr frequency condition,  $\Delta E = h\nu = \hbar\omega$ , such transition can be written for a single nucleus as Eqn (2.3-22)

$$\hbar\omega_1 = |\gamma \hbar \Delta m_l B_0| \quad (2.3-22)$$

where the left part represents the energy of the radiation and the right part is the difference between the system's energy levels. The frequency of applied radiation,  $\omega_1$ , should be of a value shown in Eqn (2.3-23)

$$\omega_1 = |\gamma \Delta m_l B_0| \quad (2.3-23)$$

The quantum mechanics selection rule, governing such a transition (  $\Delta m_l = \pm 1$  ), further simplifies the Eqn (2.3-23) to the form of

$$\omega_1 = |\gamma| B_0 \quad (2.3-24)$$

which states that the frequency of applied radiation,  $\omega_I$ , is actually equal to the frequency of Larmor precession,  $\omega_L$ , shown in Eqn (2.3-14). The two are said to be in resonance.

In classical mechanics terms, a resonance condition, allowing energy to be extracted from the source, can be fulfilled by application of a second magnetic field  $B_I$ , perpendicular to  $B_o$ , which should provide a torque to flip the moments aligned with the field  $B_o$  to the opposite direction. However, if  $B_I$  is fixed in direction, it will alternately try to increase and decrease the angle between  $M$  and  $B_o$  leading to a wobbling in the precession of  $M$ . If, on the other hand,  $B_I$  is rotating about  $B_o$  with the same frequency as the precession of  $M$  and in the same direction, its orientation with respect to  $M$  will be constant and the torque exerted on  $M$  by  $B_I$  will always be away from  $B_o$ , increasing the angle between  $M$  and  $B_o$ . The effect of the rotating magnetic field  $B_I$  ( $\omega_I$  is its frequency of rotation around the  $z$ -axis) is shown in Fig. 2-5.

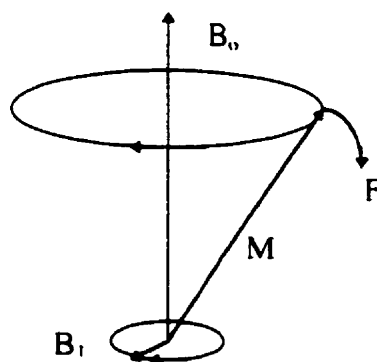


**Fig. 2-5.** Application of the rotating magnetic field  $B_I$  on the magnetization of the sample showing the torque,  $F$ , turning  $M$  away from  $B_o$ .

Normally the resonance is observed when magnetic fields in the range 1.5 - 12 T (15 - 120 kGauss) are used, and energy separation corresponding to  $h\nu$  occurs in the radiofrequency ( r.f. ) region of the spectrum ( tens or hundreds of MHz ).

Now, the equation for motion of the magnetic moment of the sample (2.3-19) must include not only the static magnetic field  $B_o$  but also time-dependent field  $B_I$ . It

should be noted that this equation holds regardless of whether or not  $B$  is time-dependent. Then, the motion is given by a superposition of the Larmor precession around  $B_o$  and a precession around the instantaneous direction of  $B_I$  field. A physical picture of events can be made simpler if they are referred not to the Cartesian axis system but to a special set of axes,  $x' y' z'$ , which has  $z'$ -axis unchanged but rotates in the  $xy$  - plane in the same sense as Larmor precession around the  $z$ -axis.

### 2.3.6. Rotating axis system.

To better understand the picture, let's first consider only the static field  $B_o$  and assume that the rotating frame rotates at some frequency,  $\omega_{frame}$ , less than the Larmor frequency,  $\omega_L$ . It would appear to an observer on the frame that the precessional frequency,  $\omega_L$ , has slowed, which would correspond to a weakening of the applied field,  $B_o$ . Labeling this apparently weaker field as  $B_{eff}$ , the precessing moment can be described in the rotating frame by Eqn (2.3-25)

$$\frac{d}{dt} \vec{M} = -\gamma \vec{B}_{eff} \times \vec{M} \quad (2.3-25)$$

where  $|B_{eff}| < |B_o|$ . If the rotating frame rotates at a frequency faster than the Larmor frequency, it would appear as though the  $z$ -field has changed direction. The effective field,  $B_{eff}$ , can be written as Eqn (2.3-26)

$$B_{eff} = \frac{1}{\gamma} [\omega_L - \omega_{frame}] \cdot \vec{Z} \quad (2.3-26)$$

where  $Z$  is a unit vector along the  $z$ -axis. The time dependence of the magnetization,  $M$ , can be rewritten as Eqn (2.3-27)

$$\frac{d}{dt} \bar{M} = - \left\{ \left| \omega_L - \omega_{frame} \right| \cdot \bar{Z} \right\} \times \bar{M} \quad (2.3-27)$$

Taking into consideration the second magnetic field,  $B_1$ , we can rewrite Eqn (2.3-19) in the rotating frame of reference as

$$\frac{d}{dt} \bar{M} = - \left\{ \left| \omega_L - \omega_{frame} \right| \cdot \bar{Z} + \gamma B_1 \bar{X}' \right\} \times \bar{M} \quad (2.3-28)$$

In a case, when the rotating frame rotates at the same frequency as the Larmor frequency,  $\omega_{frame} = \omega_L = \gamma B_0$ , the magnetic field has no effect on the magnetization, magnetic moment appears to be stationary. We can, therefore, assume that in the rotating reference frame, the sample is subjected only to the field,  $B_1$ . Now, we should remember that under the resonance conditions,  $B_1$  rotates about z-direction with the frequency  $\omega_1 = \gamma B_0$  according to Eqn (2.3-24). Since the reference axes are rotating at the same rate as  $B_1$ ,  $\omega_{frame} = \omega_1 = \gamma B_0$ , this field appears to be static. Thus, the effect of the exciting field,  $B_1$ , is simple to describe: since  $B_1$  is assumed to be applied along  $x'$ -axis, it requires the magnetization,  $M$ , to precess around  $x'$ -axis with the Larmor frequency  $\omega_{1,L} = \gamma B_1$  therefore, contributing only to the magnetization along the  $y'$ -axis. The frequency of Larmor precession about  $B_1$ ,  $\omega_{1,L}$ , should not be confused with  $\omega_1$ , the frequency of the magnetic field,  $B_1$ . Thus, application of rotating frame of reference greatly simplifies the equation of motion of the net magnetization of the sample.

### ***2.3.7. Chemical shielding, dipole-dipole interaction and spin-spin coupling.***

In the discussion of the resonance phenomenon, it was assumed that the presence of sample does not perturb the magnetic field. In fact, when a substance is placed in a magnetic field, it becomes magnetized and modifies the external field itself. The magnetization of the sample may be considered as a macroscopic (bulk) or microscopic (local) effect. The bulk intensity of the magnetization is proportional to the magnetic

field and the constant of proportionality is called the “bulk susceptibility”,  $\chi$ , of the substance. For substances with paired electrons, the magnetization reduces the magnetic field within the sample in accordance with the law of conservation of energy. Such substances are called diamagnetic.

At a molecular level, the strong external field  $B_o$  induces electronic clouds to circulate around the nucleus about the direction of  $B_o$ . The angular velocity of this electronic orbital motion can be expressed by equation similar to Eqn (2.3-24).

$$\omega_e = \frac{e}{2m_e} B_o \quad (2.3-29)$$

Since this circulation involves motion of charge (electron), it produces an electronic magnetic moment  $\mu_e$  and correspondent magnetic field  $B_e$  which in the case of diamagnetic materials, opposes the applied field  $B_o$ . Thus, electrons shield the nucleus from the influence of external magnetic field. The applied field,  $B_o$ , should be corrected for this effect as shown in Eqn (2.3-30)

$$B_{eff} = B_o - \Delta B \quad (2.3-30)$$

where  $\Delta B$  is a nuclear shielding. The resonance frequency becomes lower

$$\omega_1 = |\gamma| B_{eff} \quad (2.3-31)$$

Since the resonance frequency depends on the local field at the site of the resonating nucleus, therefore, it is possible to distinguish nuclei of the same species with different chemical environments which make NMR spectroscopy a powerful tool for the determination of the structure of molecules. It should be noted that differences in the magnetogyric ratios of different nuclei are much larger than the effects from  $\Delta B$ , so there is no trouble distinguishing different nuclei.

The nuclear shielding,  $\Delta B$ , is usually measured as a chemical shift which is the nuclear shielding divided by the applied field. It is convenient to measure it relative to a certain nuclei in a suitable reference material in parts per million

$$\delta = \frac{B_{reference} - B_{eff}}{B_{reference}} \times 10^6 \text{ ppm} \quad (2.3-32)$$

where  $B_{reference}$  is the magnetic field of the reference nuclei. The recommended reference for  $^{13}\text{C}$  and  $^1\text{H}$  is tetramethylsilane (TMS) -  $\text{Si}(\text{CH}_3)_4$ . An alternative reference, dissolved in water, is sodium 2,2-dimethyl-2-silapentane-5-sulphonate (DSS) -  $\text{Me}_3\text{SiCH}_2\text{CH}_2\text{CH}_2\text{SO}_3\text{Na}$ .

There is another contribution to nuclei shielding produced by unpaired  $p$ - or  $d$ -electrons ( $s$ -electrons are spherically symmetrical with no orbital angular momentum and no magnetic moment to contribute). It opposes the diamagnetic effect and is known as paramagnetism. Electronic magnetic moments (which are usually  $10^3$  as large as nuclear magnetic moment due to the effect of the charge to mass ratio) will try to align themselves along  $B_0$ , thus reinforcing the applied field and causing "deshielding". It leads to large chemical shifts and line broadening which makes difficult the NMR observation of paramagnetic systems.

Another source which also generates small, localized magnetic fields at the site of the resonating nucleus (but does not involve electrons) is the nuclear magnetic moments of neighbouring nuclei that are dipoles, themselves. For a nuclear magnetic field  $\mu$ , this local field  $B_{dipole}$  can be calculated using classical electromagnetic theory

$$B_{dipole} \approx \frac{\mu}{r^3} \cos \theta \quad (2.3-33)$$

where  $r$  is the distance of the first dipole from the second and  $\theta$  is the angle between the axis of the first dipole and the line joining their centers. This is a direct through-space

interaction equivalent to an interaction between magnets. The classical energy of such interaction is given by Eqn (2.3-34)

$$E \approx \frac{\mu_1 \cdot \mu_2}{r^3} - 3 \frac{(\mu_1 \cdot r)(\mu_2 \cdot r)}{r^5} \quad (2.3-34)$$

The strength of the interaction varies with the position of the inter-nuclear axis with respect to the field and is indicated by a coupling constant  $J^{dir}$  that can be derived from Eqns (2.3-33) and (2.3-34)

$$J^{dir} = -\frac{h}{4\pi^2} \gamma_1 \gamma_2 \frac{1}{2} \left( \frac{3 \cos^2 \psi - 1}{r^3} \right) \quad (2.3-35)$$

where  $\psi$  is the angle that inter-nuclear axis makes with the external field direction.

In liquids, where all values of  $\psi$  are possible because of rapid and random rotation of molecules in the sample, dipole-dipole interactions are averaged to zero. This is not the case in solids where the local magnetic fields are not averaged to zero but vary from point to point throughout the sample due to different orientations of neighboring nuclei giving the whole range of resonance frequencies resulting in a broadened NMR line. It should be noted, however, that the direct dipole-dipole interactions in solids have a very local effect due to the term  $1/r^3$ .

Second type of dipole-dipole interactions occurs between chemically bonded nuclei through the bonding electrons and, therefore, is known as indirect dipole-dipole or spin-spin interactions. The coupling (which is often referred as scalar coupling to distinguish it from dipole-dipole coupling which proceed directly through space) occurs by more than one mechanism. First, the nuclear moment  $I_1$  can be transmitted through the electronic orbital momentums thus affecting the nucleus  $I_2$ . Second, there can be dipole-dipole interaction between the electron and nuclear spins.

Since spin-spin interactions involve chemical bonds, molecular motion is not capable of averaging this type of interaction to zero as was the case with direct dipole-

dipole interaction in liquid samples. However, attempts to calculate the indirect interactions using classical analysis (Eqn (2.3-34)) gave negligible couplings not corresponded to the experimentally found results. Obviously, classical mechanics assumption that the involved particles are point dipoles, is not adequate when  $r \rightarrow 0$ . It does not allow for the possibility that the electron may be in the same region of space as the nucleus. Quantum mechanics covers this situation and introduces an electron nuclear interaction, referred to as Fermi contact interaction, which allows for the finite probability of a bonding electron being found at the nucleus.

Spin -spin coupling occurs regardless of the orientation of the molecule in the external field. It means that the strength of coupling depends on the energy difference of the two different kinds of molecules containing the spin in different spin states but is independent of the external field strength. It provides a criterion for determining whether two peaks in a spectrum are the result of spin-spin coupling or electron shielding since in the former case, the peak separation will remain the same if the spectrometer frequency changes but will differ in the latter case.

In NMR spectra, the hyperfine structure of spin-spin coupling appears as a splitting of the bands due to different nuclei. If there are only two nuclei with  $I_1$  and  $I_2$  spins, then the resonance of spin  $I_1$  is split into  $(2I_2 + 1)$  lines of equal intensity and that of spin  $I_2$  is split into  $(2I_1 + 1)$ . It arises because there are  $(2I_1 + 1)$  values of magnetic quantum number (chapter 2.3.4) for each nucleus. The band splitting of the line of nucleus with  $I_1$  arises from the shift in energy levels of the  $I_2$  nucleus between the cases in which  $I_1$  is up or down.. In most system, more than two spin will interact producing more complicated spectrum. There is a technique, called "decoupling", which allows to simplify the spectrum in both liquid and solid state NMR. It can be roughly pictured as a procedure in which spin  $I_1$  is making rapid transitions between spin up and spin down states, thus averaging to zero the effect of the coupling on spin  $I_2$ . These decoupling transitions are induced by irradiation with radio frequency at the resonance frequency of the nuclear spin to the decoupled spin.

### 2.3.8. Saturation of the spin system and relaxation processes.

There is another physical phenomenon complicating the NMR experiment. If the power of the electromagnetic radiation is high enough, eventually there will be no signal from the observed system even though initially, some absorption was detected. The system is said to become "saturated". To explain this phenomenon, we need to return to the populations of the energy levels of the macroscopic sample in the magnetic field and the definition of the resonance condition (chapters 2.3.4 and 2.3.5).

As the energy is absorbed from the r.f. radiation of  $B_1$  during the resonance, a series of transitions between the energy levels will take place. It will increase the number of spins aligned opposite to the field  $B_0$  and decrease the number of spins aligned with the field  $B_0$ , reducing the population difference. Thus, the ratio  $N_+ / N_-$  in Eqn (2.3-20) will increase and approach unity if the power of the field is high enough. When the populations of the two levels become equal, there will be an equal number of transitions  $(+ 1/2) \rightarrow (- 1/2)$  as well as  $(- 1/2) \rightarrow (+ 1/2)$  because the photon which has exactly the right (resonance) energy to stimulate upward transition, also has the right energy to stimulate (with the same probability as was shown by quantum mechanics selection rule) a downward transition. Since upward transitions correspond to energy absorption and downward transitions correspond to induced emission, no net change would be detected in the system under such condition.

Thermodynamic view. An alternative view to this situation is to consider it in terms of non-equilibrium temperature. An increase of spin population  $N_+$  can be viewed as an increase in "spin temperature",  $\Theta$ , where "spin temperature" is defined as an instantaneous population of the spin states in Eqn (2.3-20), although Boltzmann's distribution law can be properly used only for a system at thermal equilibrium.

$$N_+ / N_- \approx 1 - \Delta E / k\Theta \quad (2.3-36)$$

Approach to the "saturated" condition ( equal populations ) can be viewed as a heating up of the spin system.

If the NMR experiment is operated properly, saturation does not usually occur. The spin system will be able to return to the lower state ( cool down ) without emitting radiation. The process with which the thermal equilibrium populations reestablish is called relaxation. This is actually the process which allows to perform NMR spectroscopy since there can be no signal from “saturated” system.

The process of relaxation involves the interaction of the spin system with the rest of the sample, called “lattice” or “thermal bath”. This nuclear magnetic relaxation can be viewed from thermodynamic point of view as reapproach of the spin temperature,  $\Theta$ , to the temperature of the lattice,  $T$ . It can only occur via transitions between nuclear spin levels which allow nuclear spins to reach their equilibrium orientations with respect to  $B_0$ . Since changing the orientation of the nucleus of spin-  $\frac{1}{2}$  means changing its magnetic moment, this process can only be induced by magnetic fields in the sample.

There are, in fact, random local fluctuating fields in the sample due to the magnetic moments of nuclei in other molecules if, for example, the molecules execute Brownian ( rotational and diffusional ) motion in the liquid. Such field can act like microscopic radio frequency field and can be resolved into static component parallel to  $B_0$  and a fluctuating component perpendicular to  $B_0$ . The component perpendicular to  $B_0$  which oscillates with the Larmor frequency can induce transitions between the energy levels in a similar way as the electromagnetic radiation of the field  $B_1$  did. The x-component of this local magnetic field may be written as

$$B_x^{local} = \bar{B}_x^{local} f(t) \quad (2.3-37)$$

where  $\bar{B}_x^{local}$  is the average amplitude of the field and  $f(t)$  describes its time dependence. In quantum mechanics, this local field contributes a perturbation,  $H'(t)$ , to the Hamiltonian,  $H$ , expressed by Eqn (2.3-16). The rate of  $H'(t)$  induced transitions between the energy levels depends on the probability of such transition per unit time as shown in Eqn (2.3-38)

$$R \approx \langle \alpha | H'(t) | \beta \rangle^2 f(\omega) = \gamma^2 (\bar{B}_x^{local})^2 f(\omega) \quad (2.3-38)$$

where  $\alpha$  and  $\beta$  are the energy levels between which the transition occurs and  $f(\omega)$  is a frequency-domain function corresponding to  $f(t)$  and known as spectral density. For the relaxation processes, it is important to know how  $f(t)$  decays with time (its “memory”). Each particular motion of molecules which causes random fluctuating fields can be characterized by a specific correlation time,  $\tau_c$ , which is defined, for example, as the average time between molecular collisions for translational motion, or the average time for a molecule to rotate by one radian for reorientation motion. For mobile solutions, molecular tumbling typically gives  $\tau_c \sim 10\text{ps}$ . Eqn (2.3-39) gives a form of  $f(\omega)$  as a function of  $\tau_c$

$$f(\omega) = \frac{2\tau_c}{1 + \omega^2\tau_c^2} \quad (2.3-39)$$

Thus, the rate of adsorption of energy from the fluctuating magnetic field,  $H'(t)$ , (Eqn(2.3-38)) can be rewritten as Eqn (2.3-40)

$$R = \gamma^2 (\overline{B_r^{local}})^2 \frac{2\tau_c}{1 + \omega^2\tau_c^2} \quad (2.3-40)$$

To measure the speed with which the perturbed system relaxes back towards its equilibrium condition when  $B_1$  is removed, another term, the relaxation time, should be introduced. Practically, there are two different relaxation times:  $T_1$ , the longitudinal or the spin-lattice relaxation time, and  $T_2$ , the transverse or the spin-spin relaxation time.

The spin-lattice relaxation occurs when a local fluctuating magnetic field arising from the motion of magnetic nuclei in the lattice couples the energy of the nuclear spin to the other degrees of freedom in the sample, e.g., translational or rotational energy. This leads to the loss of energy from excited nuclear spins to the surrounding molecular lattice.  $T_1$  reflects the efficiency of the coupling between the nuclear spin and its surroundings, i.e. the rate at which the component of the magnetization parallel to the external magnetic field  $B_0$  approaches its thermal equilibrium value. The shorter this

time, the more efficient the coupling is.  $T_1$  can range from  $10^{-3}$  to  $10^2$  sec for liquids and the range is even larger for solids. It was a very long spin-lattice relaxation time which defeated the first experiments to detect NMR in the solid state.

Spin-spin relaxation arises from a redistribution of energy among the nuclear spins system. If one nucleus undergoes a transition from one spin state to another and at this point of time a second nucleus of the same type and the opposite spin state is close by, then the two nucleus can exchange energy. Spin-spin relaxation is an entropy effect as opposed to spin-lattice relaxation which is an energy effect.  $T_2$  measures the rate at which the magnetization in the plane normal to  $B_0$  approaches equilibrium. Since spin-spin relaxation does not require a change of the energy of the spin system, while spin-lattice relaxation lead to its decrease, it is clear that  $T_1$  and  $T_2$  are not necessarily equal.

The dependence of the times of nuclear relaxation processes on the correlation time of random molecular motion producing local magnetic fields can be expressed by Eqns (2.3-41) and (2.3-42) and shown as Fig. 2-6.

$$\frac{1}{T_1} \approx \frac{\tau_c}{1 + \omega^2 \tau_c^2} \quad (2.3-41)$$

$$\frac{1}{T_2} \approx \tau_c \quad (2.3-42)$$

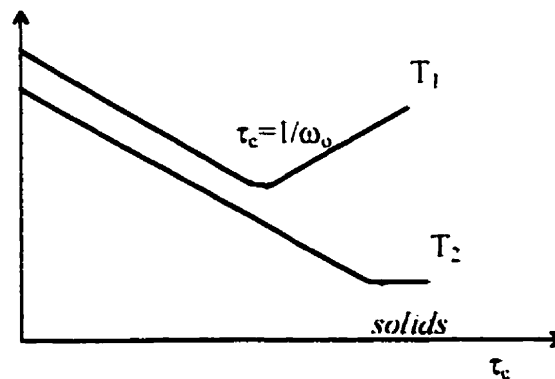


**Fig. 2-6.** The dependence of  $T_1$  and  $T_2$  on the correlation time  $\tau_c$ .

In the region where  $\omega^2 \tau_c^2 \ll 1$  (which is usually valid for mobile solutions),  $T_1$  decreases down to min value at  $\tau_c \cdot \omega_0^{-1}$  and starts to increase afterwards.  $T_2$  decreases monotonically as  $\tau_c$  increases. When  $\tau_c \rightarrow \infty$  (the region of the rigid lattice) the theory describing  $T_2$  is not valid anymore.

### 2.3.9. The NMR signal and Bloch equations.

The equations for motion of the magnetization of the sample play a major role in the NMR experiment. The NMR spectrum reflects, in fact, the behavior of the nuclear magnetization as a function of frequency,  $M(\nu)$ . NMR spectrometers receive the signal with respect to the exciting field,  $B_1$ , which rotates about z-direction with Larmor frequency, thus making the application of rotating frame very useful.

Let's consider the equation for motion of the magnetization of the sample in the rotating frame of reference including not only Larmor precession as in Eqn (2.3-28) but the relaxation processes as well. Bloch, in his classical macroscopic approach, assumed that the components of  $M$  decay to its equilibrium value,  $M_0$ , exponentially as shown by Eqns (2.3-43) and (2.3-44)

$$\frac{d}{dt} M_z = -\frac{M_z - M_0}{T_1} \quad (2.3-43)$$

$$\frac{d}{dt} M_x = -\frac{M_x}{T_2} \quad \frac{d}{dt} M_y = -\frac{M_y}{T_2} \quad (2.3-44)$$

Combining Eqn (2.3-28) with Eqns (2.3-43) and (2.3-44), we obtain the Bloch equation (2.3-45) which include the Larmor precession as well as the relaxation process:

$$\frac{d}{dt} \vec{M} = -\left\{(\omega_L - \omega_1)\vec{Z} + \gamma B_1 \vec{X}'\right\} \times \vec{M} - \frac{1}{T_2}(M_x \vec{X}' + M_y \vec{Y}') - \frac{1}{T_1}(M_z - M_0)\vec{Z}$$

where  $x'$ ,  $y'$  - axes of rotating frame of reference are rotating with angular frequency  $\omega_1$  corresponding to the frequency of the oscillating field  $B_1$ . Eqn (2.3-45) is a vector equation which can be rewritten in terms of the components of the magnetization,  $M_x$ ,  $M_y$ , and  $M_z$  as Eqn (2.3-46), (2.3-47), and (2.3-48):

$$\frac{d}{dt} M_x = (\omega_L - \omega_1) M_y - \frac{M_x}{T_2} \quad (2.3-46)$$

$$\frac{d}{dt} M_y = -(\omega_L - \omega_1) M_x - \frac{M_y}{T_2} + \gamma B_1 M_z \quad (2.3-47)$$

$$\frac{d}{dt} M_z = -\gamma B_1 M_y + \frac{M_0 - M_z}{T_1} \quad (2.3-48)$$

The steady state solution of the above equations, i.e. where the equilibrium is always maintained, can be calculated at

$$M_x = M_0 \frac{\gamma B_1 T_2^2 (\omega_L - \omega_1)}{1 + T_2^2 (\omega_L - \omega_1)^2 + \gamma^2 B_1^2 T_1 T_2} \quad (2.3-49)$$

$$M_y = M_0 \frac{\gamma B_1 T_2^2}{1 + T_2^2 (\omega_L - \omega_1)^2 + \gamma^2 B_1^2 T_1 T_2} \quad (2.3-50)$$

$$M_z = M_0 \frac{1 + T_2^2 (\omega_L - \omega_1)^2}{1 + T_2^2 (\omega_L - \omega_1)^2 + \gamma^2 B_1^2 T_1 T_2} \quad (2.3-51)$$

In a mathematical terms, using the similarity between the mathematics of vector (with coordinates  $M_x$  and  $M_y$  in Argand diagram) and the complex number algebra, the complete NMR spectrum can be described by a complex number with a frequency-dependent argument shown by Eqn (2.3-52)

$$M_{\perp} = M_x + iM_y = |M_{\perp}| (\cos \phi + i \sin \phi) \quad (2.3-52)$$

where  $M_{\perp}$  is the projection of the magnetization on the  $x'y'$  plane with  $x'$ -axis as a real and  $y'$ -axis as imaginary axes. At the same time in polar coordinates,  $M_{\perp}$  is described by the length  $|M_{\perp}|$  and the phase  $\phi$ . The Bloch theory predicts that the NMR signal contains  $M_x$  and  $M_y$  components which are  $90^\circ$  out of phase with each other.  $M_x$  component is along  $B_1$ , i.e. in phase with  $B_1$  and reflects dispersion, while  $M_y$  component is perpendicular to both  $B_0$  and  $B_1$ , i.e. out of phase and reflects adsorption. The output from the sample contains both components. The  $M_y$  signal is usually selected for the analysis.

Under the conditions where  $\gamma B_1 \ll (T_1 T_2)^{1/2}$ , i.e. when the r.f. power applied is sufficiently low so that saturation does not occur, Eqn (2.3-50) describing the motion of  $M_y$  can be further simplified to the following form

$$M_y = M_0 \gamma B_1 \frac{T_2}{1 + (\omega_L - \omega_1)^2 T_2^2} \quad (2.3-51)$$

Eqn (2.3-51) describes the line shape known in spectroscopy as a Lorentzian line shape defined by Eqn (2.3-52)

$$g(\omega)_{\text{Lorentz}} = \frac{1}{a} \left[ \frac{1}{1 + (2\pi \Delta\omega / a)^2} \right] \quad (2.3-52)$$

where the line width at the half height,  $a$ , is written as Eqn (2.3-53) and measured in Hertz

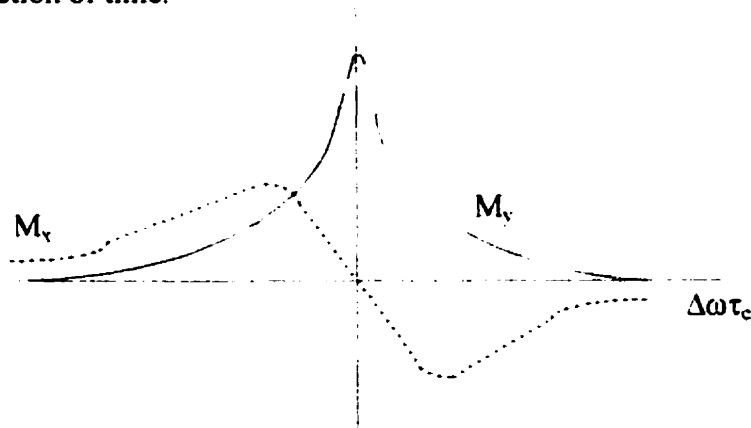
$$a = 1 / \pi T_2 \quad (2.3-53)$$

Fig. 2-7 illustrates the shape of absorption,  $M_y$ , and dispersion,  $M_x$ , components of the nuclear magnetization as a function of frequency.

Eqn (2.3-53) shows that the linewidth is inversely proportional to  $T_2$ , which means that relaxation causes the spectral line broadening. The explanation of this phenomenon lies in the physical nature of the spectrum. The linewidth is actually a measure of the uncertainty in the energies of the two energy states. According to Heisenberg's Uncertainty Principle

$$\Delta E \cdot \Delta t \leq \hbar \quad (2.3-54)$$

uncertainty in measuring the energy is inversely proportional to the lifetimes of these states. Thus, the decrease of the lifetime of the excited state, caused by relaxation, increases  $\Delta E$ , i.e. the spectral linewidth. If there were no relaxation effects and no field inhomogeneities, the excited state would have an infinite life, and the line shape would be a delta function of time.



**Fig. 2-7.** The absorption,  $M_v$ , and dispersion,  $M_r$ , components of the nuclear magnetization as a function of frequency.

Another line shape function frequently found in spectroscopy is the Gaussian line defined by Eqn (2.3-55)

$$g(\omega)_{\text{Gauss}} = \exp\left[-(2\pi \Delta\omega / a)^2\right] \quad (2.3-55)$$

### 2.3.10. *The intensity of an NMR signal.*

The signal,  $I$ , in the NMR spectrum depends, in fact, on the rate at which the system can absorb irradiation from radiofrequency radiation,  $R$ . However, NMR spectrometers do not detect the rate of energy adsorption directly, but rather the rate of induced magnetization change in the direction of receiver coil,  $dM_x/dt$ . This turns out to be  $R B_1$ .

The rate of energy adsorption,  $R$ , depends, in turn, on three factors: the probability of the induced transition per spin per unit time, the energy change corresponding to this transition, and the population difference between the spin states. A detailed quantum-mechanical treatment shows that the signal intensity can be expressed by Eqn (2.3-56)

$$I \approx \frac{\gamma^4 \cdot N \cdot B_0^2 \cdot B_1}{T} \quad (2.3-56)$$

where  $N$  is the total number of nuclei of the sample. Thus, the NMR signal obtained is directly proportional to the number of nuclei producing it. It is the adsorption line in Fig. 2-7 whose area is proportional to the number of nuclei generating the signal. It allows to use NMR for quantitative studies such as obtaining concentrations for a given chemical compound if standard concentration is provided.

### 2.3.11. *Fourier transform NMR spectroscopy.*

The main problem of the application of NMR is its generally poor sensitivity because the intensity of an NMR signal in the spectrum depends on the magnitude of the magnetization which is a small value by itself and is further reduced by the limited number of NMR active nuclei,  $N$ , available in the system of interest (see Eqn(2.3-56)). For example, natural abundance of the isotope  $^{29}\text{Si}$  is only 4.67% which gives the relative sensitivity of only 0.08 when compared to 1 for  $^1\text{H}$ <sup>2,17</sup>. To enhance it, different techniques

including pulse Fourier transform NMR spectroscopy have been developed. This technique is also more efficient than swept experiments (continuous wave approach) with regard to information content, as all the nuclei are simultaneously and not sequentially studied.

In pulsed Fourier transform NMR experiments, the resonance condition is achieved by application of a short high power oscillating magnetic field,  $B_1 \cos \omega_1 t$ . How can the motion of the magnetization be described under such condition? If the duration of pulse is short with respect to  $T_1$  and  $T_2$ , so that there is no time for any relaxation to occur during the pulse, then the equation for motion of the magnetization (2.3-45) will include only first term responsible for precession and no relaxation terms. In the rotating frame of reference which rotates with angular velocity  $\omega_1$ ,  $M$  will precess with constant angular frequency  $\gamma B_1$  in a plane perpendicular to the direction of  $B_1$  (chapter 2.3.8). By the end of the pulse, the magnetization will have precessed by the angle  $\varphi$  with respect to  $z$ -axis:

$$\varphi = \gamma B_1 t_{pulse} \quad (2.3-57)$$

where  $t_{pulse}$  is a duration of the pulse. Let's take a closer look onto the action of r.f. pulse. First, consider the case when  $\varphi = \pi/2$ . When  $B_1$  is switched on and directed along  $x'$ -axis (the net magnetization is along  $z$ -axis),  $M$  begins to precess around  $x'$ -axis. However, the duration of pulse is chosen to be very short, usually in the range 1-50  $\mu s$ , which is much shorter than the time required to one full precession about  $x'$ . Thus, the magnetization does not have time to precess around  $x'$ -axis and it merely tips toward  $y'$ -axis as shown on Fig. 2-8 so that  $M = M_0 Y'$ . If  $B_1$  is applied parallel to the  $y'$ -axis (the phase of  $B_1$  is shifted by an angle  $-\pi/2$ ), the magnetization points in the  $x'$ -direction. In terms of individual spins, a  $90^\circ$  pulse causes them to become coherent.

If  $\varphi = \pi$ , then by the end of the pulse  $M$  will lie in the  $-z$  direction which means that it simply inverts the population of the  $E_+$  and  $E_-$  states, thus inverting the net magnetization. Thus, the use of pulses allow to place the magnetization in any chosen direction, without any loss in magnitude of  $M$  (provided that the pulse is short,  $t_{pulse} \ll T_1, T_2$ ).

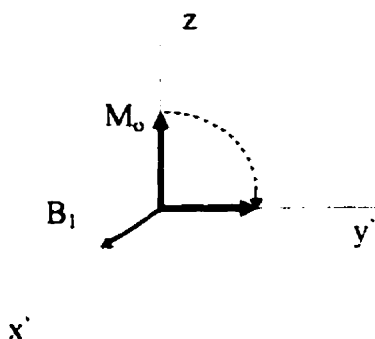


**Fig. 2-8.** The action of r.f. pulses with  $\varphi = \pi/2$ .

Following the pulse when  $B_1$  is switched off, Boltzmann equilibrium is slowly restored by relaxation processes, i.e. the motion of the magnetization is reduced to relaxation processes. Under such condition, the first term in Eqn (2.3-45), describing Larmor precession, vanishes leaving only the terms responsible for relaxation processes.

A  $180^\circ$  degree pulse is followed by purely spin-lattice relaxation expressed by Eqn (2.3-58)

$$M_z(t) - M_0 = (M_z(0) - M_0) \exp(-t / T_1) \quad (2.3-58)$$

where the process of relaxation is treated as a first-order kinetics process with  $1/T_1$  as a relaxation rate constant. In a graphical way,  $T_1$  gains the meaning of a characteristic time required for the magnetization to return to its original direction after being inverted by  $B_1$  through  $180^\circ$  as discussed above.

The decay of the  $y'$ - component of the magnetization ( transverse relaxation) is usually measured in the NMR experiment. Since a  $90^\circ$  pulse causes individual spins to become coherent,  $T_2$  is a characteristic time required for individual spins to lose their phase with each other after being rotated through  $90^\circ$  by  $B_1$ . One of the mechanisms of losing coherence is a "flip-flop" mechanism in which nuclei with equivalent spins on different energy levels exchange energy. It happens when the downward transition of one nucleus, originally at a higher energy state, occurs simultaneously with the upward transition of the other nucleus that was initially at a lower energy state.

The integrated form of Eqn (2.3-45), describing motion of  $M_y$  as a function of time, takes form of Eqn (2.3-59) and can be shown as Fig. 2-9.

$$M_y(t) = M_0 \exp(-t / T_2) \quad (2.3-59)$$

For a more general case, we should include the Larmor precession as well as the relaxation process into the motion of the magnetization and express it as Eqn (2.3-60).

$$M_{\perp} = M_0 e^{-t/T_2} e^{-i\omega t} \quad (2.3-60)$$

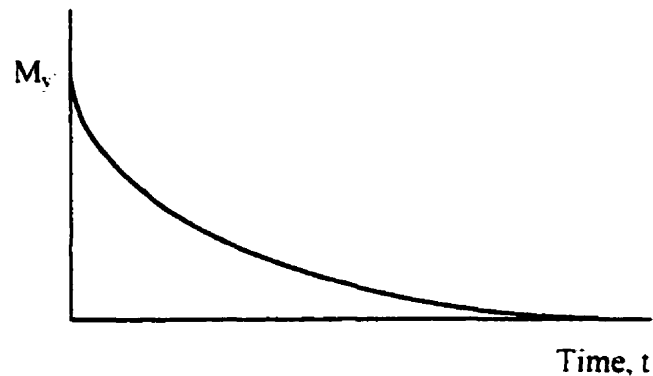


**Fig. 2-9.** A plot of change in the magnetization with time.

The plot of the decay of the x'-y' component of the magnetization with time, i.e. signal intensity attenuated as transverse relaxation occurs with time, is referred as free induction decay (FID). The Fourier transform of the resulting FID curve gives the spectrum. The Fourier transform is a generalized transformation in function space which can convert a pulse in the time domain,  $f(t)$ , to the corresponding range of  $B_1$  amplitudes in the frequency domain,  $F(\omega)$ , built from a series of sine and cosine function with different frequencies  $\omega$ 's. This transformation is shown in Eqn (2.3-61)

$$F(\omega) = 2\pi \int_{-\infty}^{\infty} e^{-i\omega t} f(t) dt \quad (2.3-61)$$

In other words, the spectrum is the frequency-domain equivalent of the time-domain and can be converted back by opposite Fourier transformation shown in Eqn (2.3-62)

$$f(t) = 2\pi \int_{-\infty}^{\infty} e^{i\omega t} F(\omega) d\omega \quad (2.3-62)$$

Fig. 2-10 represents a time plot of a single pulse and corresponding frequency plot.

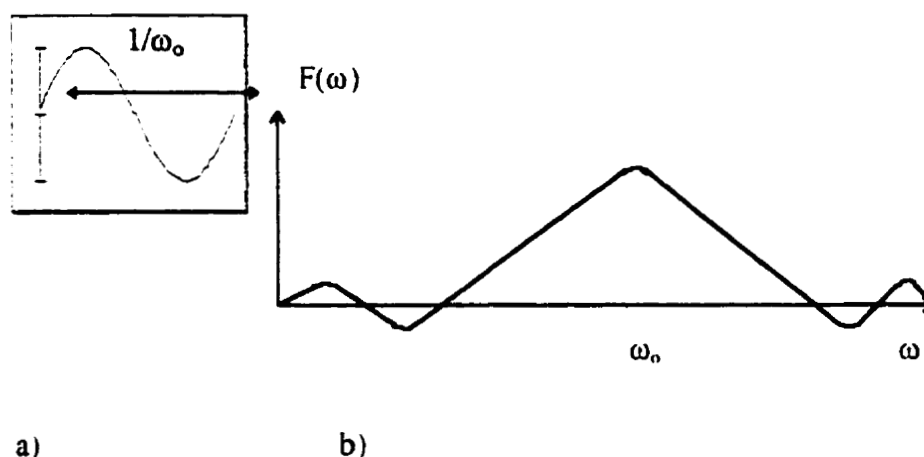


**Fig. 2-10.** A single pulse of r.f. radiation in a) time domain and b) frequency domain.

If the nucleus were sensitive enough, just one pulse would give an FID curve that could be Fourier transformed to give the spectrum. When it is not sensitive enough, the entire spectrum is run many times with the interval  $T$  between pulses and stored in a computer. If all spins being monitored were equivalent, and the frequency of the pulse were exactly on resonance, a simple exponential decay would be observed as shown by dotted line in Fig. 2-11. In this case, the rotating frame of reference is stationary with respect to the rotation of the  $x'$ - $y'$  component of the magnetization vector of the sample. When the frequency of the r.f. pulses,  $\omega_I$ , is chosen to be near the resonance, i.e. the frequency of Larmor precession,  $\omega_L$ , but not equal it, the solid line in Fig. 2-11 is obtained. In the latter case, the rotating frame of reference and the  $x'$ - $y'$  component of the magnetization vector of the sample are not moving in phase and the oscillation that is observed is the result of interference of the two waves moving in and out of phase. If the

sample contains many different spins, each with its own resonance frequency, the FID will be a complicated interferogram.

For many experiments, it is necessary to calibrate  $B_1$  to secure the maximum signal height obtainable from a single pulse. Measurement of peak height as a function of  $t_{pulse}$  should yield a sine curve. Distortions from a sine curve often imply that the r.f. magnetic field  $B_1$  is inhomogeneous over the volume of the sample, a condition desirable to avoid.

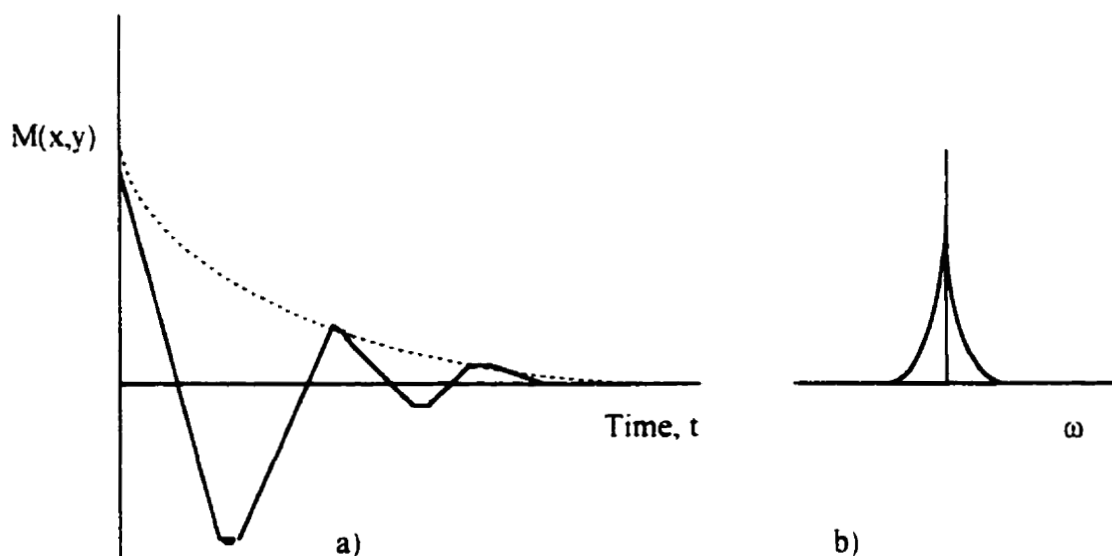


**Fig. 2-11.** A free induction decay curve (a) and its Fourier transform (b). The dashed line corresponds to the resonance condition and the solid line to the off-resonance condition.

## 2.4. Solid State NMR Theory

There are a number of contributions to the NMR spectra of solids, including Zeeman, dipolar, electron shielding, scalar, and quadrupolar interactions (for  $I > 1/2$ ) as shown by a general Hamiltonian expressed by Eqn (2.4-1).

$$H = H_{Zeeman} + H_{dipolar} + H_{chem.shift} + H_{scalar} + H_{quadrupolar} \quad (2.4-1)$$

Their relative importance depends on the nucleus being observed in the system under study. In a particular solid state system, one or two of the terms will usually dominate the Hamiltonian and hence, determine the characteristics of the spectrum.

The critical feature of the interactions in solids is that they are anisotropic (i.e. orientation dependent) due to the fixed orientations of the molecules. In liquids, the interactions are averaged due to the rapid (on the NMR time-scale) and random (isotropic) tumbling of the molecules as was explained in chapter 2.3.7. In the case of chemical shifts and scalar couplings, discrete average values are found in solution. In the case of dipolar and quadrupolar couplings, the average values are exactly zero and these effects are not observed in solution spectra at all.

The restricted motion of the molecules in solids does not allow these interactions to be averaged. There is a significant spread in the resonance frequencies which may result in a line of several tens of kHz wide (several orders of magnitude broader than a typical liquid NMR signal). The characteristics of NMR spectra of solids are thus more complex and contain an orientation dependence but potentially they may yield more information than solution spectra. To simplify the analysis of NMR spectra, several procedures including dipolar decoupling (introduced in chapter 2.3.7) and Magic Angle Spinning (MAS) have been developed.

#### 2.4.1. Magic Angle Spinning

As was shown in chapter 2.3.7, the coupling constant,  $J^{dr}$ , can be expressed by Eqn (2.3-35)

$$J^{dr} = -\frac{h}{4\pi^2} \gamma_1 \gamma_2 \frac{1}{2} \left( \frac{3 \cos^2 \psi - 1}{r^3} \right) \quad (2.3-35)$$

where  $\psi$  is the angle that inter-nuclear axis makes with the external field direction. The geometric factor  $(3 \cos^2 \psi - 1)$  causes the line broadening for solids. The MAS is the

technique which has a similar effect for solids as the rapid and random rotation of molecules in liquids, i.e. it averages this geometric factor to zero. In such experiments, the sample is caused to spin around the axis inclined at some specific "magic" angle,  $\beta$ , to the external magnetic field direction so that  $(3\cos^2\beta - 1) = 0$ . This angle  $\beta = 54.7^\circ$ .

There may be a problem however, since the rate of rotation at this magic angle should be greater than the static linewidth to average the dipolar interactions properly. In practice, mostly weak interactions between dilute spins causing low broadening can be removed by MAS, while strong dipolar interactions with abundant spins require such spinning speed that may be hard to achieve experimentally. Those interactions can be removed by irradiation at the resonance frequency of the abundant nuclei, i.e. decoupling technique which was introduced in chapter 2.3.7.

Another source of linebroadening in the solid state NMR is anisotropic electron shielding that arises from non spherical density distribution of electrons around nuclei. Since the chemical shift depends on the orientation of the molecule with respect to the external field, and molecular orientation varies from crystallite to crystallite, there will be a continuous spread in the shifted lines. This effect is called Chemical Shift Anisotropy (CSA). Linebroadening caused by CSA can be removed by MAS, since the chemical shielding parameter depends on the geometric factor  $(3\cos^2\psi - 1)$  in the way similar to the dipolar coupling. It can be averaged to zero by MAS at the speed achievable on modern NMR instruments.

#### **2.4.2. Cross Polarization**

Dipole-dipole interactions, that cause spectral broadening, are not the only difficulty in the solid state NMR experiments. It was already mentioned in chapter 2.3.11 that the main shortcoming of NMR is its poor sensitivity that in turn causes a low intensity NMR signal. The reason for low sensitivity is a small magnitude of the net magnetization of the nuclei in the sample. Today's use of high  $B_0$  fields together with fast data accumulation made possible by the application of Fourier transform technique have solved the problem of low sensitivity for protons and some other nuclei with relatively

large magnetic moments. All other active NMR nuclei including  $^{29}\text{Si}$  are less sensitive than protons, and this situation is often aggravated by low natural abundance and long relaxation times. For example, natural abundance of the isotope  $^{29}\text{Si}$  equal to 4.67% compared to 99.98% for  $^1\text{H}$  <sup>2.17</sup>. It results in low intensity of the signal since the net magnetization depends on the number of NMR active nuclei.

Another problem arises from the fact that the spin-lattice relaxation time in solids can be so long, so that even multipulse methods, known to be more efficient than swap experiments, can be problematic in terms of the time required for the experiment because there should be a necessary delay time equal to  $\sim 5T_1$  between successive acquisitions in order to avoid saturation of the system. If the time between successive runs can be decreased, more runs can be made in a given period of time and this would increase the signal-to noise ratio. (It is known that the signal is proportional to the number of runs obtained while the noise increases as a square root of the number of runs).

The cross polarization (CP) method introduces a way of enhancing the sensitivity by overcoming both “the low intensity” and “long time requirement” problems for dilute spin systems. The first problem was solved by deriving the magnetization of nuclei with low abundance, labeled as  $S$ , from the highly abundant nuclei, labeled as  $I$  ( $I$  and  $S$  nuclei are  $^1\text{H}$  and  $^{29}\text{Si}$  respectively for the purpose of this discussion). The second problem can be solved by cutting down the time between successive FID's. In the CP method, the delay between acquisition is dictated by the protons rather than the silicon nuclei, even though it is silicon nuclei that are being monitored. Since protons relax much faster than silicons, many more acquisitions may be obtained in a set amount of time.

Let's discuss a two-spin system consisting of a sensitive,  $I$ , and an insensitive nucleus,  $S$ . The population of the energy levels in equilibrium is given by the Boltzmann law, and according to Eqns (2.3-17) and (2.3-20) can be written as Eqn (2.4-2)

$$\frac{N_-}{N_+} = \exp \frac{-\gamma \hbar B_0}{kT} \quad (2.4-2)$$

The population difference between the energy states  $N_+$  and  $N_-$  is, therefore, determined by the gyromagnetic ratio,  $\gamma$ , of the nucleus that changes its spin state during the transition. For sensitive nucleus,  $I$ , with larger gyromagnetic ratio, a larger population difference will result than for insensitive nucleus,  $S$ , with small gyromagnetic ratio. If it were possible to govern the spin populations of the insensitive nucleus,  $S$ , by the Boltzmann distribution of the sensitive nucleus,  $I$ , then, it would result in enhanced absorption and emission for the  $S$  transition. It is actually possible through interchange of respective spin populations. The phenomenon is called polarization transfer and the method using polarization transfer is known as cross polarization.

Cross polarization is achieved in the rotating frame of reference by using the pulse sequence shown in Fig. 2-12. The sequence of a CP experiment will be explained in the following paragraphs from a thermodynamic point of view using the spin temperature concept. This theory leads to a few sets of simple equations which play the same role, for nuclear magnetic resonance in solids, as Bloch equations for the case of liquids.

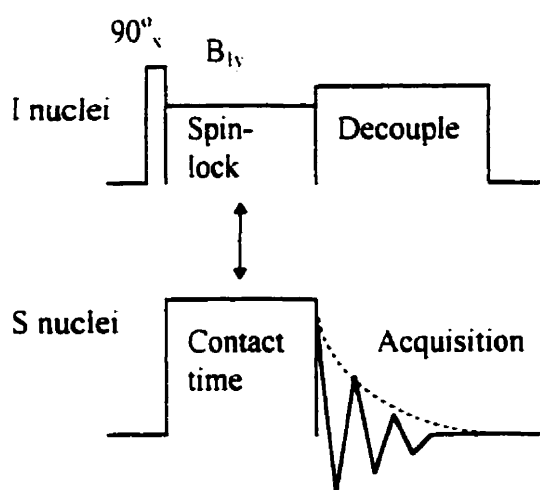


Fig. 2-12. The pulse sequence for CP experiment.

In the first step, the abundant spin system should be transferred into a state with an artificially low temperature. This is done by applying a  $90^\circ$  pulse of radiation along the  $x'$ -axis at the resonance frequency of  $I$  spins that turn the magnetization along the  $y'$ -axis in the rotating frame of reference. Next, in opposition to a traditional pulse experiment,

the pulse of  $B_1$  is not turned off but its phase is changed by  $90^\circ$  so that it is now aligned with the magnetization along  $y'$ -axis. (In this situation, the behavior of the  $M_{y'}$  reminds us of that of  $M_z$  in the laboratory frame aligned with  $B_0$  without  $B_1$ ). The magnetization,  $M_{y'}$ , is said to be spin-locked by  $B_{1y'}$ , since it appears in the rotating frame as constant and is maintained at that constant value for the duration of spin-locking process. However, since the magnetization was developed in  $B_0$  which is much greater than  $B_1$ , the magnitude of the magnetization will be far larger than can be maintained by  $B_1$ . Therefore,  $M_{y'}$  will decay with time. The process of decay can be expressed by Eqn (2.4-3)

$$M_{y'}(t) = M_0 \exp(-t / T_{1\rho}) \quad (2.4-3)$$

where  $T_{1\rho}$  is a characteristic relaxation time constant for  $I$  spin system in the rotating frame of reference.

According to Eqn (2.4-2), the magnetization is proportional to the excess number of spins in the lower energy state,  $E_-$ , created by the static external field  $B_0$  at equilibrium conditions as shown by Eqn (2.4-4)

$$\frac{N_-}{N_+} (\text{equilibr}) = \exp \frac{-\gamma_I \hbar B_0}{kT_{\text{lattice}}} \quad (2.4-4)$$

Under the spin-locking condition of the field  $B_{1y'}$ , the excess number of spins can be expressed by Eqn (2.4-5)

$$\frac{N_-}{N_+} (\text{spin-locked}) = \exp \frac{-\gamma_I \hbar B_{1y'}}{kT_I} \quad (2.4-5)$$

The relation between the spin and the lattice temperatures can be deduced from the Curie Law that connects the external magnetic field with the induced magnetization in the sample. For the  $I$  spins, the Curie Law shows that the magnetization induced in the laboratory frame by equilibration with the lattice can be written as Eqn (2.4-6)

$$M'_o = \frac{1}{4} \hbar^2 \gamma_I^2 N_I B_o / T_{lattice} \quad (2.4-6)$$

where  $N_I$  is the total number of  $I$  nuclei per unit volume. Since this magnetization is transferred by the spin-locking procedure into the rotating frame of reference, it can be written as Eqn (2.4-7)

$$M^I = \frac{1}{4} \hbar^2 \gamma_I^2 N_I B_I^I / T_I \quad (2.4-7)$$

although there is no equilibrium anymore, it is still possible to consider the instantaneous temperature of the  $I$  spin system from a semi-classical point of view. Since the experiment was set so that  $B_{Iv}$  is much weaker than  $B_o$ , then, the temperature of the  $I$  spins,  $T_I$ , is much less than the temperature of the lattice,  $T_{lattice}$  as shown by Eqn (2.4-8)

$$\frac{T_I}{T_{lattice}} = \frac{B_I^I}{B_o} \quad (2.4-8)$$

Thus, the abundant spin system is transferred to a low temperature state by the spin-locking procedure. While the temperature of the  $I$  spins is very low, the  $S$  spin system has an infinite temperature because there is no magnetization of the  $S$  spins in the rotating frame of reference.

In the next step, the dilute spin system,  $S$ , should be brought into the thermal contact with the cold system of abundant spin  $I$ . Dipole-dipole interaction is a main physical mechanism in solids which can provide the needed thermal contact between the two systems. As was explained before, a time-dependent dipole-dipole interaction can give rise to transition between different energy levels in a given system. In the case of two spin systems, there is a probability of their energy exchange ( by a flip-flop mechanism ) if the time dependence of the energy coupling between  $I$  and  $S$  has a frequency that matches the Bohr condition for the difference between energy states. In other words, the resonance frequencies of the two systems should be close to each other.

$$\omega_1^I = \omega_1^S \quad (2.4-9)$$

However, since the magnetogyric ratios of the  $I$  and  $S$  systems are typically quite different ( e.g.  $\gamma_H / \gamma_{Si} \sim 5$  ), their natural Larmor frequencies ( $\omega_L = |\gamma| B_o$ ) are also different, and the probability of energy exchange between the two systems is very low. In CP experiment, the match between Larmor frequencies of the two systems is achieved using a special double resonance technique where two r.f. fields  $B_1^S$  and  $B_1^I$  are applied to the  $I$  and  $S$  spin systems respectively so that

$$\gamma_I B_1^I = \gamma_S B_1^S \quad (2.4-10)$$

Equation (2.4-10) is known as the Hartmann-Hahn condition and implies that in their respective rotating frames of reference, the  $I$  and  $S$  spins are precessing at equal rates with comparable energies. As a result of such thermal contact, heat will flow from the high temperature  $S$  system to the low temperature  $I$  system. The spin energy will be redistributed among the  $I$  and  $S$  spins to give an average spin temperature  $T_{spin}$ . The abundant spin system will warm up slightly while the artificial temperature of the dilute spin system will be significantly reduced since the heat capacity of the abundant spin system is much greater than the heat capacity of the dilute spin system. Another way of saying that the temperature of the dilute spin system decreased is to say that the population difference between the energy levels increased when the Zeeman levels of the two system were matched by CP. Thus, the  $I$  spins lose only small portion of their total magnetization while the  $S$  spins derive a significant magnetization from the  $I$  spin system. Since the  $I$  spin system has a larger magnetogyric ratio than the  $S$  spin system, then it can be seen from Eqn (2.4-11) (substituted by Eqns (2.4-8) and (2.4-10)) that the  $S$  spin magnetization increased by a factor of  $\gamma_I / \gamma_S$

$$M_S = \frac{1}{4} \hbar^2 \gamma_S N_S B_1^S / T_S = \frac{1}{4} \hbar^2 N_S \frac{\gamma_I}{\gamma_S} B_o / T_L \quad (2.4-11)$$

Thus, the signal, derived from the enhanced by CP magnetization of the  $S$  spin system, increases leading to increased sensitivity of measurement.

Also, by bringing the two systems into contact in the manner discussed above, the second problem of long spin-lattice relaxation times is overcome. At the end of acquisition of  $S$  system, the magnetization of  $S$  spins is near zero as in the beginning of the experiment. Since the energy exchange occurred through flip-flop mechanism,  $T_{IS}$  is irrelevant and the delay between acquisition is dictated by the protons rather than the silicon nuclei. The  $I$  spin system will decay with time constant  $T_{1p}$  expressed by Eqn (2.4-3). Since  $I$  spins (i.e. protons) relax much faster than  $S$  spins (i.e. silicons), more acquisitions may be obtained in a given amount of time.

The CP method can be used as a filtering mechanism, because it is sensitive to the distance between the spin systems as  $1/r^6$ . This local effect of CP is caused by the dipole-dipole interactions in the sample which is the main contributor to the relaxation processes in solids. The spin-lattice relaxation rate,  $T_1^{-1}$ , (or the rate of energy adsorption,  $R$ , in Eqn (2.3-38) ) is calculated from the classical electromagnetic definition of the nuclear magnetic field using Eqn (2.3-33)

$$T_1^{-1} = R \approx \gamma^4 \mu^2 \tau_c / r^6 \quad (2.4-12)$$

Thus, the greater the isolation of the  $S$  nuclei from the  $I$  nuclei, the less is signal enhancement of these nuclei by CP. For all practical purposes, the CP enhancement of an  $S$  nucleus more than four bonds away from an  $I$  nucleus can be considered zero.

If this is now applied to a zeolite system, this means that the use of the CP technique makes possible the detection of silicon atoms to which hydroxyl groups are attached, even the ones, whose signals detected without CP were very weak and poorly resolved. In the CP spectra, the peak intensities of silicon atoms bearing OH groups are selectively and strongly enhanced owing to CP process. If it can be assumed that Si-OH groups are mostly at the surface of the zeolite system, then, by application of the CP technique one can monitor the surface of the zeolite system.

## 2.5. Theory of Energy Filtered Transmission Electron Microscopy

It is well known that electrons are scattered much more strongly by matter than X-rays or visible light is. A single atom can scatter enough electrons to allow it to be detected in an electron microscope. Monomolecular layers can give strong diffraction effects with electrons while the thickness of micrometer or more is necessary for comparable relative diffraction intensity for X-rays. It is only because of such strong electron scattering effect, that fine details, at an atomic level, can be seen in an electron microscope<sup>2,28</sup>.

Electron Energy Loss Spectroscopy (EELS), in turn, explores the energy distribution of electrons which have interacted with a specimen. This technique, when combined with an electron microscope, provides a powerful microanalytical method called EFTEM. It gives detailed information about the chemical, physical and electronic nature of our sample. For example, energy filtered images or diffraction patterns can be recorded for elemental distribution maps. In this technique, electrons are separated according to their energy loss by a spectrometer which also acts as a lens<sup>1,19</sup>. All the information that can be obtained about the sample is contained in the angular and energy distribution of the electrons that have passed through the specimen.

A consistent theory of electron diffraction and microscope image was built up using direct analogies with the concepts of elementary physical optics<sup>2,28</sup>. When an electron wave is transmitted through the potential field of the charged particles in a sample, it changes its phase. Any assembly of atoms is considered to be the phase object for the electron wave in the same way as a thin piece of glass does for light waves. The resulting wave has a distribution of relative phase values depending on the variations of the potential field it has traversed, plus small changes of amplitude corresponding to the loss of electrons by the inelastic scattering process. The angular distribution of electron wave intensity detected is then given by squaring the magnitude of the wave amplitude in the diffraction pattern, given by a Fourier transform of the exit complex wave amplitude distribution.

The three components of any EELS experiment are (1) a source of electrons, (2) a suitable sample of material, (3) a spectrometer for analyzing the energy of the scattered electrons. We will limit our discussion to an experimental arrangement which is compatible with the operation of a conventional transmission microscope. In this case, the source of electrons is the gun of the microscope. Since we are using a microscope, the incident beam is capable of being focused on to a specimen area, which can be imaged using the normal optical system of the instrument. The specimen itself should be a "thin" section of the material, thin enough to give a good conventional TEM image. Section thickness is an important parameter in minimizing secondary energy loss events that interfere with element-specific mapping. The spectrometer is then placed after the specimen to analyze the transmitted electrons as shown in the Fig. 2-13.

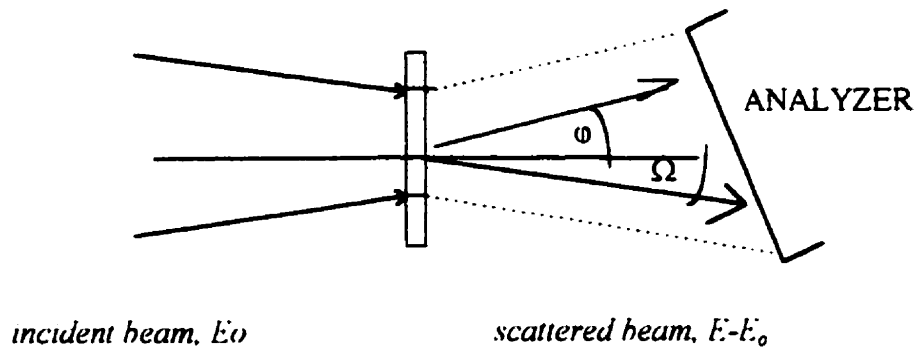


**Fig. 2-13.** The geometry of energy loss spectroscopy in the electron microscope illustrating the scattering angle  $\phi$  and the spectrometer acceptance angle  $\Omega$ .

In EELS experiments, the transmitted signal intensity  $I(E)$  is measured at some energy loss ( $E$ ) over the angle  $d\Omega$  about some angle  $\phi$  from its original direction. If the intensity of the incident beam is  $I_0$ , then  $I(E, \phi) / I_0$  is the fraction of the incident electrons which lost some energy  $E$  and were deflected into spectrometer. This fraction is directly proportional to the probability that any incident electron will suffer an energy loss  $E$  while being scattered into the solid angle  $d\Omega$  about  $\phi$ ,  $d^2\sigma(E, \phi)$ . This probability

is called a “doubly differential cross-section”. The constant of proportionality is  $N$ , the number of atoms per unit area in the volume investigated. Thus,

$$I(E, \varphi) / I_0 = N \times d^2\sigma(E, \varphi) / dE d\Omega \quad (2.5-1)$$

The result of the measurements is an EELS spectrum in which transmitted signal intensity is plotted as a function of the energy loss. Fig. 2-14 shows a typical electron energy loss spectrum recorded from a thin film of titania using 200 kV incident beam with  $\theta = 100$  mrad.

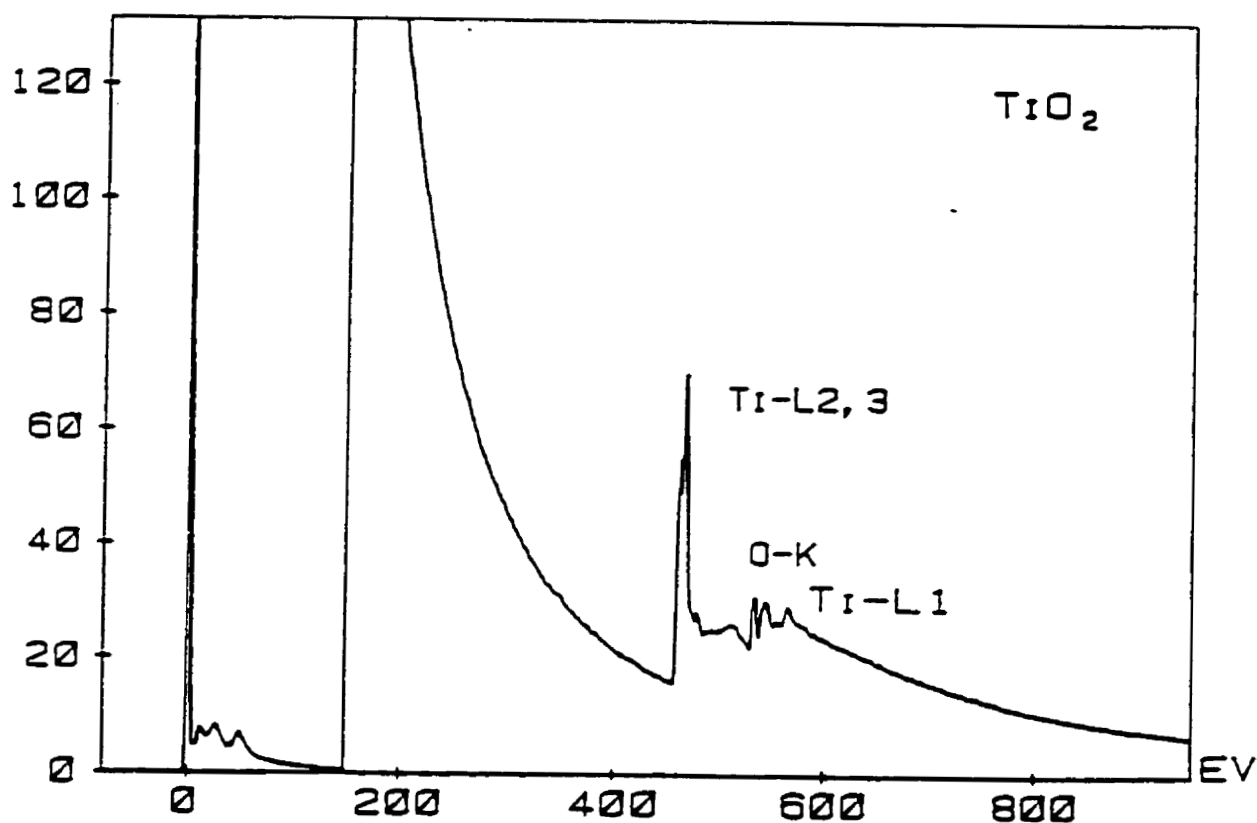


Fig. 2-14. An image of  $\text{TiO}_2$  thin film.  $E_0=200\text{kV}$ ,  $I_0 = 6.2 \times 10^8$ ,  $\theta = 100$  mrad.

The most prominent feature is a large maximum in the intensity centered at  $E=0$ . This is usually called “zero-loss peak”. It contains (1) unscattered electrons which have suffered no interactions while passing through the sample and so retain their original

energy and the direction of motion, (2) elastically scattered electrons which have been deflected by the nuclear charge of atoms and haven't lost any significant amount of energy, and (3) electrons which have been scattered by phonons, i.e. vibrations of the atoms. Energy losses of the latter ones lie within the region of a few meV to a few hundred meV and can only be studied with energy resolution significantly better than that of EELS systems.

The remainder of the spectrum contains the inelastically scattered electrons, those which have suffered both a deflection, and a loss of energy as the result of some interaction with the sample. The most obvious characteristic of this part of the spectrum is the rapid fall of the average intensity as  $E$  increases. The change in the gain of the recording system is required to keep the detail on the spectra visible.

The area with a broad peak in the spectrum extending from the edge of the zero-loss contain energy losses from interactions in which valence or conduction electrons are excited and inter- or intraband transitions are possible. The best known of these events is the plasmon excitations, i.e. collective oscillations of valence electrons occurring in metals and alloys. For those materials where valence electrons are not free enough to participate in such collective oscillations, the low energy loss are mainly due to the excitation or ionization of electrons in molecular orbitals.

As the broad peak decays away, one observes step-wise increases in the intensity at characteristic positions corresponding to ionization energies of the inner shell electrons ( K-shell, L-shell, etc. ) of specific atoms. It is interesting to note that X-ray emissions that are produced are relaxation of the ionized atoms from the well known localized characteristic intensity peaks in X-ray spectra. The final region is the most important for microanalysis providing a convenient method of identifying atoms of different types.

The background contains no microanalytical information but is the dominant feature of the spectrum. It comes form a variety of effects such as the excitations from valence states to vacuum, multiple plasmon losses and the tails of features at lower energy losses. The characteristic edges of interest are riding on this falling background which, therefore, must be stripped from the spectrum before progress can be made.

Background subtraction is usually achieved by fitting the energy differential cross-section for the background to the form shown in Eqn (2.5-2)

$$d\sigma / dE = AE^{-r} \quad (2.5-2)$$

where E is the energy loss and A and r are parameters depending on the acceptance angle of the spectrometer. It is done in the region before the ionization edge. Next step is the extrapolation of this fitted background beyond the edge threshold. Details of this procedure are given in<sup>2,29</sup>.

The most important edges for microanalytical purposes are the K- and the L-edges as can be seen from the Fig. 2-14. The edge which is of interest for us is L<sub>2,3</sub> edge of Ti which is lying at 460 eV. Net titanium map can be obtained by subtracting energy loss pre-image collected at 430 eV from post-image collected at 460 eV. The difference between two images corresponds to the electrons that have initiated titanium L<sub>2,3</sub> ionization events.

A schematic diagram of the column of the Zeiss 902 energy-filtering microscope is presented on Fig. 2-15. The features of interest in this diagram are the prism-mirror-prism type spectrometer located after the first set of lenses. This spectrometer disperses the electrons into their different energy components and forms an energy-loss spectrum in the spectrometer exit plane. An energy-selecting slit is located in this plane to select the portion of the energy-loss spectrum that will be used to form the energy-filtered image on the microscope viewing screen or CCD detector. The microscope can be operated in image mode, diffraction mode, or spectrum mode. When the microscope is run in spectrum mode, an energy-loss spectrum can be acquired and processed using the CCD detection system.

Thus, the image is first magnified by the objective lens. The beam then passes through the prism-shaped magnetic field to exit at an angle of 90°. To help correct most second-order aberrations in the image, the beam is reflected at an electrostatic mirror on the symmetrical axis of the device, passes through the prismatic field a second time and emerges on the original optic axis of the microscope. Curvature of the entrance and exit

surfaces of the magnetic prism is used to correct some of the aberrations in the energy spectrum as well. A slit system below the magnetic prism can select any small energy band, filtering out images of all other energies.

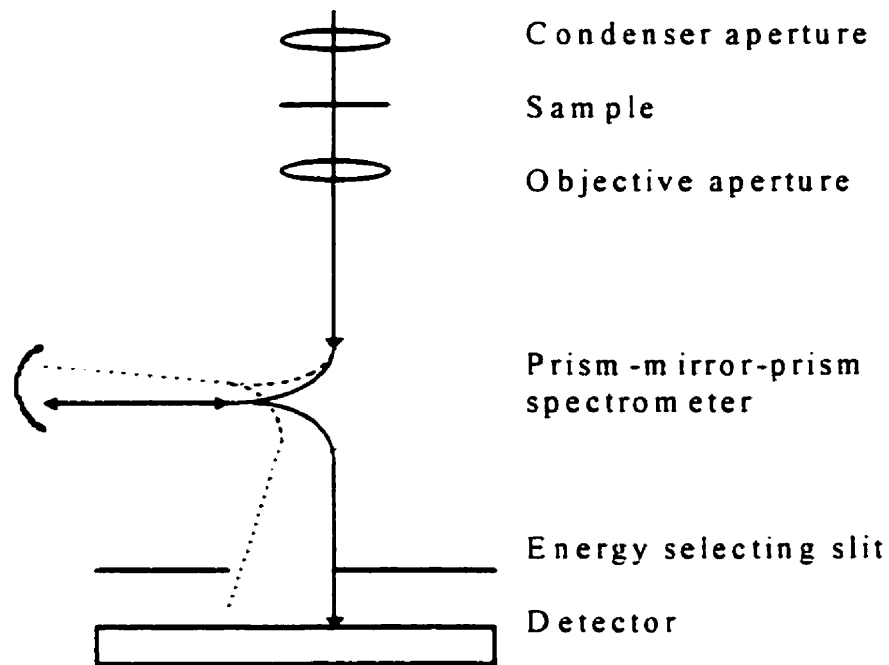


**Fig. 2-15.** Diagram of Zeiss 902 column showing prism-mirror-prism filter, energy selecting slit, and CCD detector. The solid line indicates the path along the optical axis of the system followed by electrons with 0 eV loss ( elastic scatter). The dashed line is a representative path for an electron with an energy loss.

## Chapter Three

### Examination of Physical State of a TiO<sub>2</sub> Photocatalyst on the Zeolite Support by CP MAS NMR, XRD and BET Methods

#### 3.1. Introduction

The present study concentrates on using the Solid State <sup>29</sup>Si NMR method to characterize the physical state of titanium oxide on the support. Conventional methods have also been used when applicable. Solid State NMR is well suited to establish the microenvironment of different Si nuclei in zeolites because it probes the local magnetic environment and is generally very sensitive to any deviations from a general structure. By comparison, X-ray diffractometry, which is perfectly suitable for obtaining the geometric structure of crystals, is at the same time limited by its own nature, because it senses long-range orderings and periodicities even if they are imperfect<sup>31</sup>. Application of high-resolution Solid State NMR has additional advantage in the case of highly siliceous materials including ZSM-5 zeolite. Al content is so low in them that it doesn't affect the <sup>29</sup>Si spectrum. Consequently, the resonances observed are due to only tetrahedrally coordinated silica "centers", Si(OSi)<sub>4</sub>, and are extremely narrow according to [1.17]. Because of their excellent resolution, these spectra can be exploited in a number of ways to obtain subtle information regarding their structure not easily obtainable by other techniques.

For example, in one of the first applications of MAS NMR spectroscopy to the investigation of zeolites<sup>32</sup>, five possible Si environments in various zeolites were established and characteristic ranges of their chemical shifts were assigned. In [1.18], a combination of <sup>29</sup>Si single-pulse MAS and CP MAS experiments was used to characterize the external surface of zeolite MAP and to elucidate its structure with respect to the bulk.

The <sup>29</sup>Si-<sup>1</sup>H CP MAS method can be used for surface analysis of zeolites because of the two following reasons. First, there are usually no <sup>1</sup>H nuclei covalently bonded to

the framework of zeolites<sup>3,3</sup> and it can therefore be assumed that Si-OH groups are only at the surface. The presence of an -OH group may be chosen as an “operational” definition of a “surface” Si atom. In this sense, surface means an Si atom which can form a new Si-OE linkage ( where E is any appropriate element ) by elimination of water between Si-OH and HO-E. Second, since CP is sensitive to the distance between the spin systems of interest as  $1/r^6$  (see Eqn (2.4-12)), it will greatly discriminate in favor of silicon atoms close to the OH groups. Practically, the influence of magnetic fields at the distance more than four bonds away can be considered zero. If this is now applied to a zeolite system, this means that surface Si-OH groups can be selected via CP.

In the present work, the CP MAS technique is exploited for monitoring of surface coverage versus physical loading of TiO<sub>2</sub> on ZSM-5 zeolite. If TiO<sub>2</sub> loads onto the surface of a zeolite by chemical attachment to the zeolite via the zeolite’s Si-OH groups, the -OH groups might be eliminated from the surface. Hence, these former Si-OH groups do not contribute to the signal obtained via CP. If it is now assumed that remaining Si-OH groups are unaffected by the TiO<sub>2</sub>, then one can quantitatively measure the chemical surface coverage of TiO<sub>2</sub>. Thus, one can compare the chemical surface coverage versus the physical loading via CP.

## **3.2. Experimental Section**

### **3.2.1. Materials**

The ZSM-5 zeolites (ammonium form, SiO<sub>2</sub>/Al<sub>2</sub>O<sub>3</sub>=50 and 280) were purchased from Zeolyst International. Kaolinite KGA-1 was received from Dept. of Geology, University of Missouri, Columbia. Sodium 2,2-dimethyl-2-silapentane-5-sulfonate (DSS) was purchased from Aldrich.

### **3.2.2. Sample Preparation**

The  $\text{TiO}_2$  sol was synthesized by the method called acid-catalyzed sol-gel formation<sup>1,15</sup>. The reactant composition was 200ml of water, 1ml of nitric acid, and 28.1g of titanium (IV) tetraisopropoxide dissolved in 10 ml ethanol. The resulting slurry was peptized for 8 hours.

The composite photocatalyst was prepared by thermally binding titanium dioxide onto the surface of the ZSM-5<sup>1,15</sup>. ZSM-5, saturated with water for half an hour, was mixed with  $\text{TiO}_2$  sol by stirring for 1 h. Then, this mixture was dried by evaporation at  $50^\circ\text{C}$  for 2-3h. This was followed by heating at  $120^\circ\text{C}$  overnight and finally the solid was calcined at  $450^\circ\text{C}$  for 11-12h. Fig. 3-1 illustrates how titania can become anchored on the surface of the zeolite through silanol groups. By this procedure, a series of samples with 2.5%, 5%, and 10 wt. % of titanium oxide on ZSM-5 were prepared. It was confirmed earlier<sup>1,15</sup> that the measured content of  $\text{TiO}_2$  in the samples was close to that calculated from synthetic conditions, as expected.

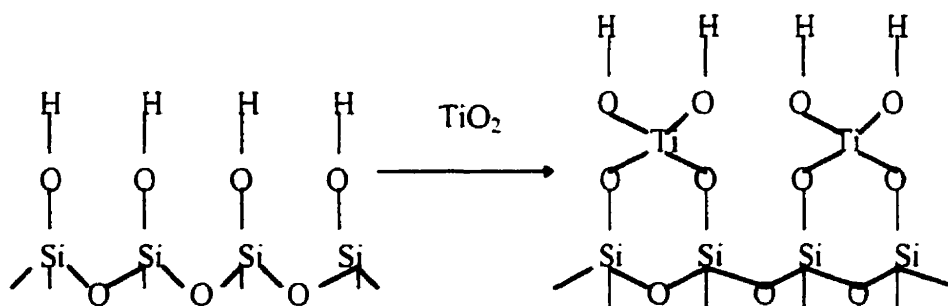


**Fig. 3-1.** Binding of titanium oxide onto the zeolite surface.

### 3.2.3. Procedures

**Nuclear Magnetic Resonance.** Solid State  $^{29}\text{Si}$  FT-NMR spectra were obtained at 59.63 MHz under Magic Angle Spinning (MAS) conditions at ambient temperatures on a Bruker AMX-300 spectrometer. Silicon chemical shifts were referenced to sodium 2,2-dimethyl-2-silapentane-5-sulfonate (DSS). Samples were packed in zirconia rotors 7 mm in diameter. Conventional Bloch decay (solid cycle) and cross polarization (CP MAS)

from  $^1\text{H}$  were acquired for  $^{29}\text{Si}$ . Solid cycle spectra were recorded at 5MHz spinning rate using a  $90^\circ$  fixed pulse with 5s delay time.  $^{29}\text{Si}$ - $^1\text{H}$  CPMAS experiments were performed with low power square pulse proton decoupling at 2 MHz spinning rate. All conditions were optimized on the original samples. Fig 3-2 shows an example of the CP MAS contact time optimization experiment performed at 2 kHz spinning rate with 7s delay time. The transmitter power (TL0), that drives the  $^{29}\text{Si}$  amplifier, was set to 20.9db and the decoupler power (DL0) was set to 10.8db so as to have the optimal HH match with available  $^{29}\text{Si}$  power. The experimentally found optimal delay time, equal to 5s, and contact time, equal to 4ms, are close to the reported values for ZSM-5<sup>34-35</sup>.

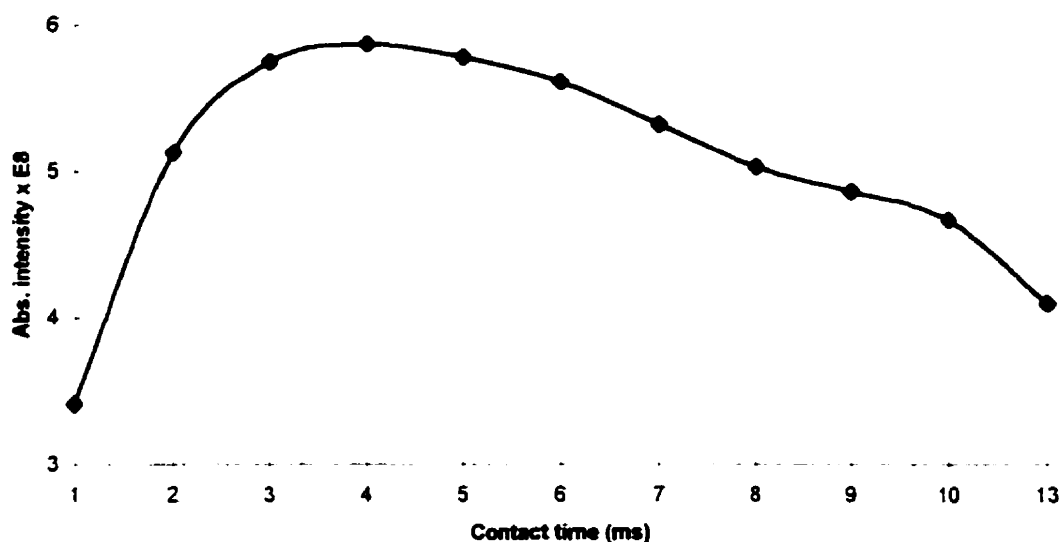


**Fig. 3-2.** CPMAS contact time optimization done at BL7 probe spun at 2 kHz with D1=7s, DL0=10.8db, TL0=20.9db.

It should be noted that samples were spun at a low rate of 2 MHz during CPMAS experiments in spite of the danger of introducing spinning side bands. The lower spinning rate was chosen because it was reported<sup>36</sup> that higher MAS rates may interfere with the cross polarization process leading to loss of signal and distortion of relative intensities. This was the case in CP-MAS experiments at the 5 kHz spinning rate.

The instrument was linked to the 1D WIN-NMR data processor. Data processing involved phase and baseline correction, integration of the areas under the peaks of interest, and interactive deconvolution using a Gaussian function for bandfitting.

**The BET method.** Surface area measurements were performed on a ASDI-RXM 100 system representing liquid nitrogen adsorption isotherms at  $-196^{\circ}\text{C}$ . Prior to experiments, samples were degassed at  $250^{\circ}\text{C}$  for at least 3 hours until the pressure of  $10^{-7}$  Torr was obtained. The volume of adsorbed  $\text{N}_2$  was normalized to standard temperature and pressure. The results were calculated using the four points BET method.

Surface area,  $S$ , was obtained by applying the BET equation to the adsorption data over relative pressure,  $x = P/P_0$ , of  $0.05 \div 0.3$  as shown in Eqn (3.2-1) and (3.2-2)

$$\frac{x}{V_r(1-x)} = \frac{1}{kV_{\max}} + \frac{(k-1)x}{kV_{\max}} \quad (3.2-1)$$

$$S = V_{\max} N_A s_N / 22414 \quad (3.2-2)$$

where  $V_{\max}$  and  $V_x$  represent the maximal adsorption volume at monolayer coverage and the adsorption volume at certain pressure  $x$ , respectively, in the units of ml/g at STP.  $N_A$  and  $k$  are the Avogadro's and the BET constants, respectively.  $S_N$  is the area occupied by each nitrogen molecule ( $0.162 \text{ nm}^2/\text{molecule}$  at  $77.4 \text{ K}$ )<sup>3,7</sup>.

**Powder X-ray Diffraction.** Structures of the samples were analyzed using an XDS 2000 (Scintag Inc.) instrument.  $\text{Cu K}_\alpha$  radiation source ( $\lambda=0.154 \text{ nm}$ ) with a generator voltage of 45 kV and the current of 40 mA was employed. Diffraction patterns were taken over the  $2\theta$  range of  $5^{\circ} - 60^{\circ}$  and the results were treated with the Jade program for XRD pattern processing (Material Data Inc.)

### 3.3. Results

### 3.3.1. Solid State $^{29}\text{Si}$ NMR spectroscopy

The simple MAS spectrum obtained with a  $90^\circ$  pulse sequence is shown in Fig. 3-3a. The signal peak occurs near -115 ppm with a shoulder near -108 ppm. The  $^1\text{H} - ^{29}\text{Si}$  cross polarization technique yields the spectrum in Fig. 3-3b. In this figure, the signal near -105 ppm is substantially enhanced in relation to the -115 ppm signal compared to that of the shoulder in Fig. 3-3a. The difference is readily explained<sup>2,23</sup>. The  $90^\circ$  pulse interrogates all the Si atoms, bulk and surface. The CP-MAS experiment requires short H - Si distance since CP depends on distance as  $1/r^6$ . Thus, the CP signal will be dominated by those Si atoms with -OH groups.

Following several precedents<sup>2,23, 38, 39</sup>, we assign the peak at near -115 ppm in Fig. 3-3a to bulk Si atoms with four Si neighbors and the partially resolved shoulder to surface Si atoms with -OH groups. Absolute numbers of Si atoms in CP experiment can not be determined because the enhancement factor (CP efficiency) is not known. This enhancement factor is sensitive to both Si-H distance and the chemically different Si atom environments in the zeolite. There is also dependence of the relative intensities of the signals on the contact times as shown in Fig. 3-4. At a short contact time, the -OH bearing surface Si groups (signal near -105 ppm), i.e. those silicons having the shortest Si-H distance, are most effectively cross-polarized and show the highest intensity. With increasing contact time, Si atoms located as next neighbors to surface Si-OH groups give rise to increasing intensity of the signal near -114 ppm. The optimal contact time (4 ms) was chosen to secure the maximal and reproducible signal obtainable from surface Si groups.

In order to estimate surface coverage by titanium oxide, we should compare relative intensities ( peak areas ) of similar samples differentiated only by titania loading, and recorded at identical, optimized, and reproducible CP-MAS conditions. An internal standard is required. Kaolinite,  $\text{Al}_2(\text{Si}_4\text{O}_{10})(\text{OH})_2$ , was chosen for the following reasons. First, it is crystalline, giving a sharp, well resolved signal. Second, its chemical shift, equal to -95.5 ppm<sup>2,23</sup>, lies in the range of the zeolite signals but the peak can be resolved. Finally, the high concentration of -OH groups in kaolinite allows the use of a

small quantity so as not to decrease the sample signal. Fig. 3-5 shows a series of  $^{29}\text{Si}$  spectra of  $\text{TiO}_2$  loaded ZSM-5 ( $\text{SiO}_2/\text{Al}_2\text{O}_3=50$ ) samples with kaolinite as the internal standard. The same content of kaolinite was used in all experiments. The noise levels of the spectra are constant, the signals are normalized to the intensity of the kaolinite signal (-93 ppm). Thus, the difference between the "surface Si signal" (-104 ppm) of the zeolite with titanium oxide (Fig. 3-5 b, c, d) and without it (Fig. 3-5 a) is real.

Similar difference in the intensity of the "surface Si signal" was observed for the spectra obtained from the sample of pure ZSM-5 ( $\text{SiO}_2/\text{Al}_2\text{O}_3=280$ ) and the sample loaded with 2.5 wt. %  $\text{TiO}_2$  as shown in Fig. 3-6 b) and c) respectively.

It is also worth mentioning that the "surface Si signal" obtained from ZSM-5 ( $\text{SiO}_2/\text{Al}_2\text{O}_3=50$ ) is much stronger than the one from ZSM-5 ( $\text{SiO}_2/\text{Al}_2\text{O}_3=280$ ) as can be seen by comparing the spectra in Fig. 3-6 a) and b). This observation is in agreement with the well known fact that hydrophobicity of zeolites increases with the increase of  $\text{SiO}_2/\text{Al}_2\text{O}_3$  ratio.

Overall, the cross-polarization technique confirms that thermally loaded  $\text{TiO}_2$  displaces surface -OH and is chemisorbed on the surface of the zeolite. This result confirms a suggestion described in [1.15] based on Raman spectra of titanium oxide on ZSM-5. The authors<sup>1 15</sup> reported a new band at  $380 - 382 \text{ cm}^{-1}$  at a low titania loading and suggested that it was associated with the formation of Ti-O-Si linkages between titanium oxide and ZSM-5 support. With the increase of titanium oxide loading, this peak shifted smoothly towards the  $396 \text{ cm}^{-1}$  frequency characteristic of anatase.

Quantitative estimation of the relative surface silanol groups requires either integration of the areas under the peaks of interest or deconvolution of the CP-MAS spectra. The latter technique was applied in order to reduce overlapping of the peaks and, consequently, more accurate measuring of the area under the peaks of interest. Since only the units very close to the surface Si-O-H groups contribute to the signal at -105 ppm, the area under the peak is directly proportional to the population of these groups. ( Contact times are chosen to maximize the desired filtering ).

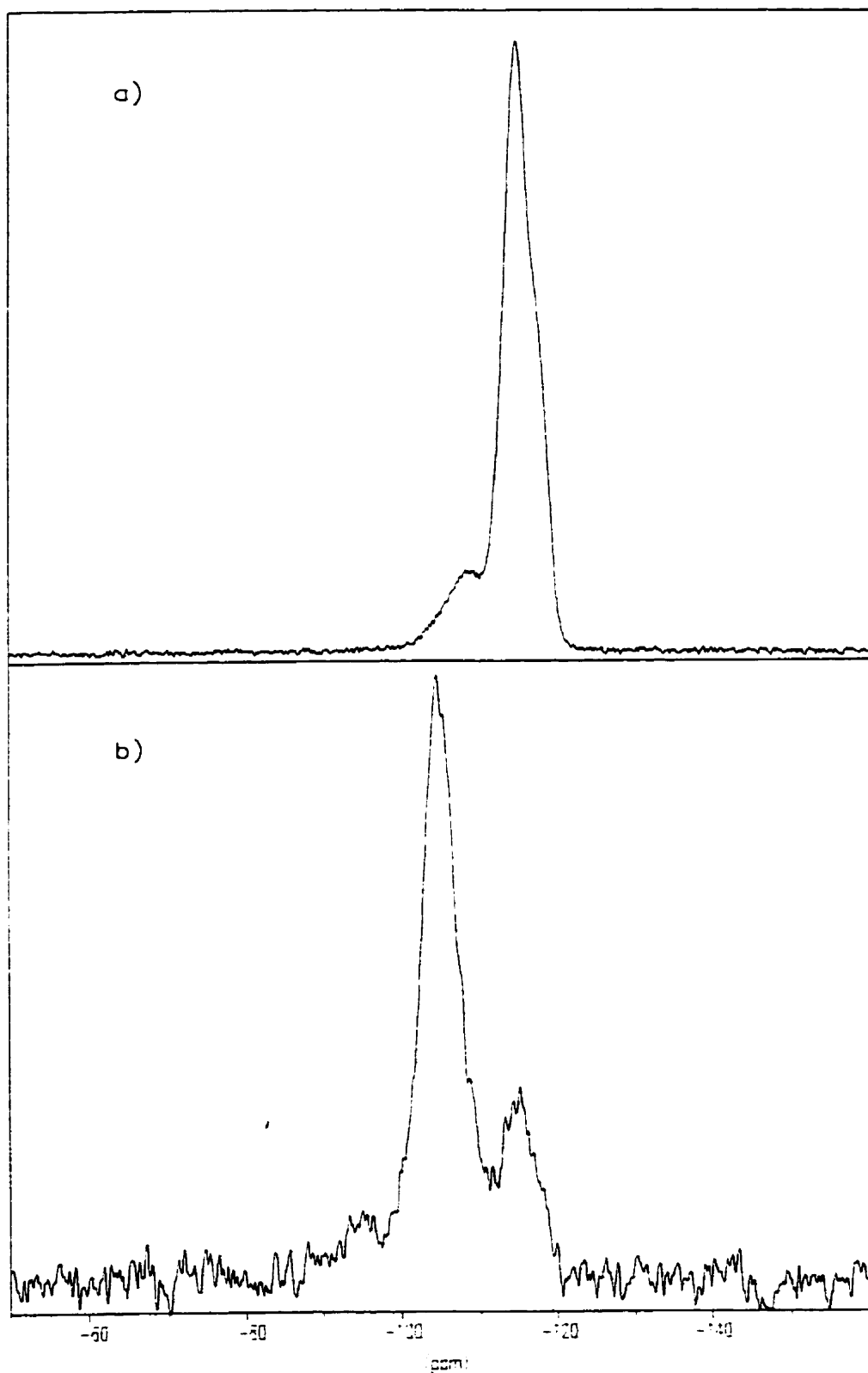


**Fig. 3-3.** Solid State  $^{29}\text{Si}$  NMR spectra of ZSM-5, a)  $90^\circ$  pulse sequence, b)  $^{29}\text{Si}$ - $^1\text{H}$  cross-polarization.

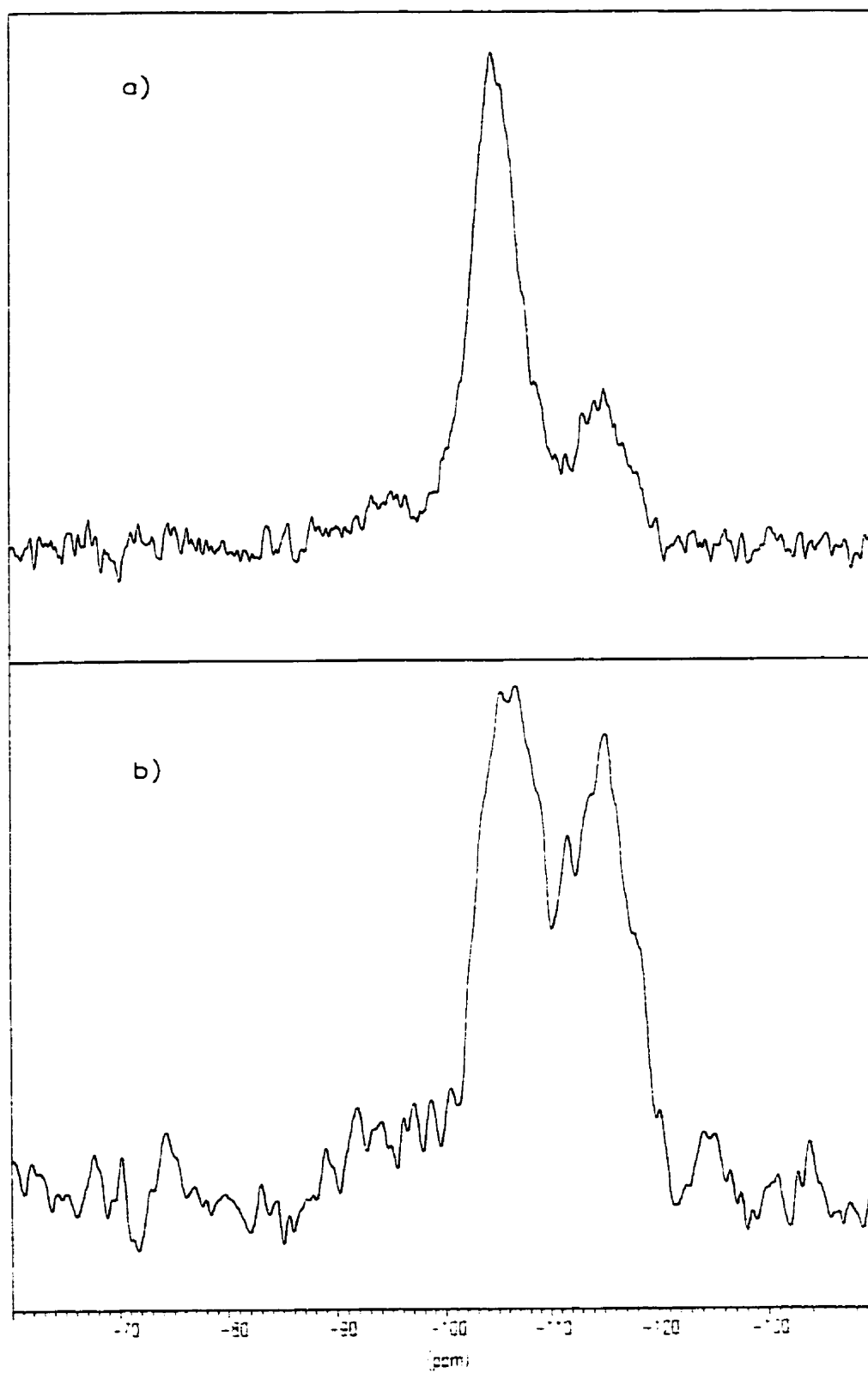


**Figure 3-4.** Dependence of relative intensities of signals on contact time, a) 1ms, b) 7ms.

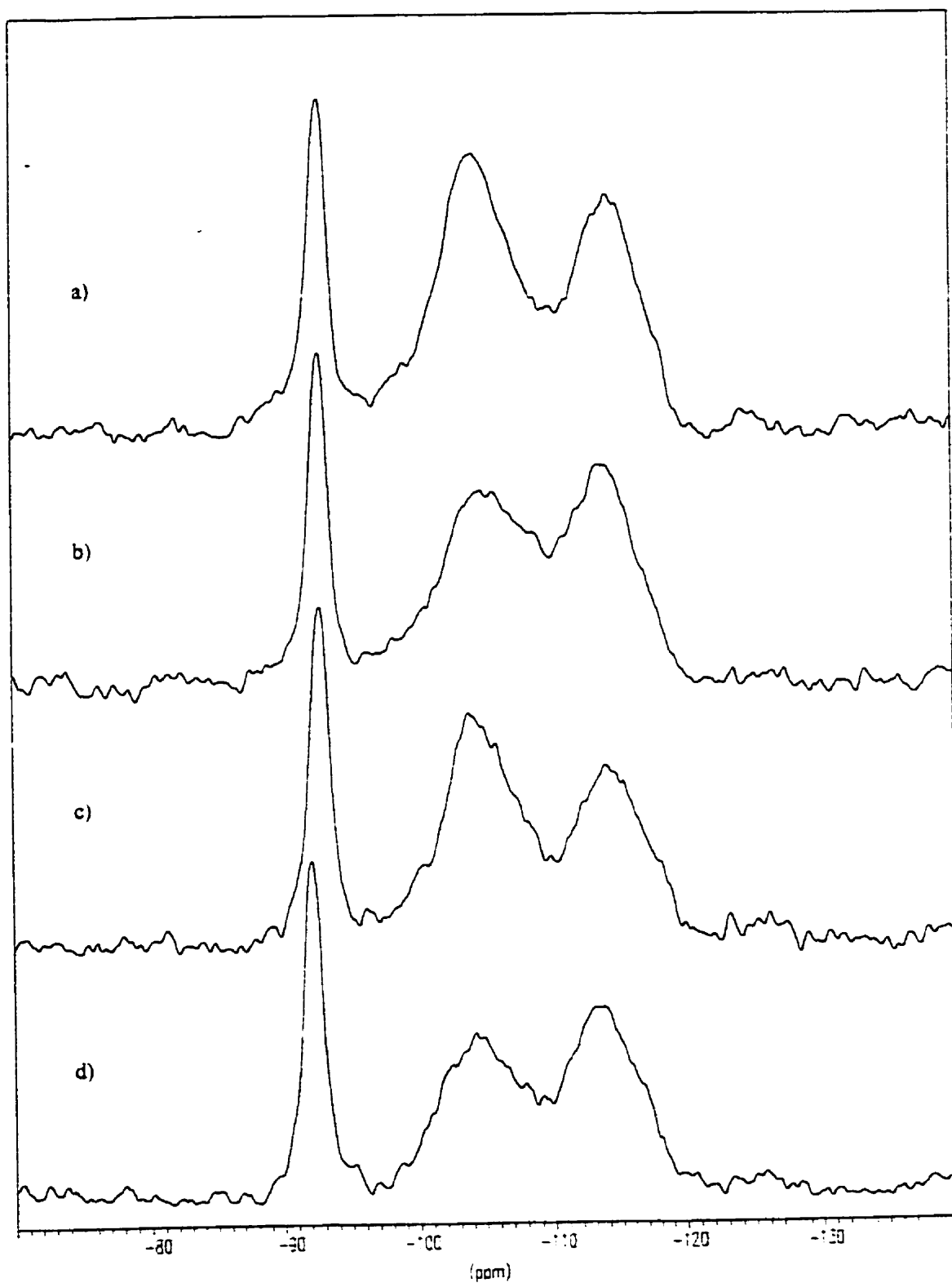


**Figure 3-5.** CPMAS spectra of **a)** pure ZSM-5 ( $\text{SiO}_2/\text{Al}_2\text{O}_3=50$ ), **b)** 2.5 wt. %  $\text{TiO}_2$ , **c)** 5 wt. %  $\text{TiO}_2$ , **d)** 10%  $\text{TiO}_2$ .

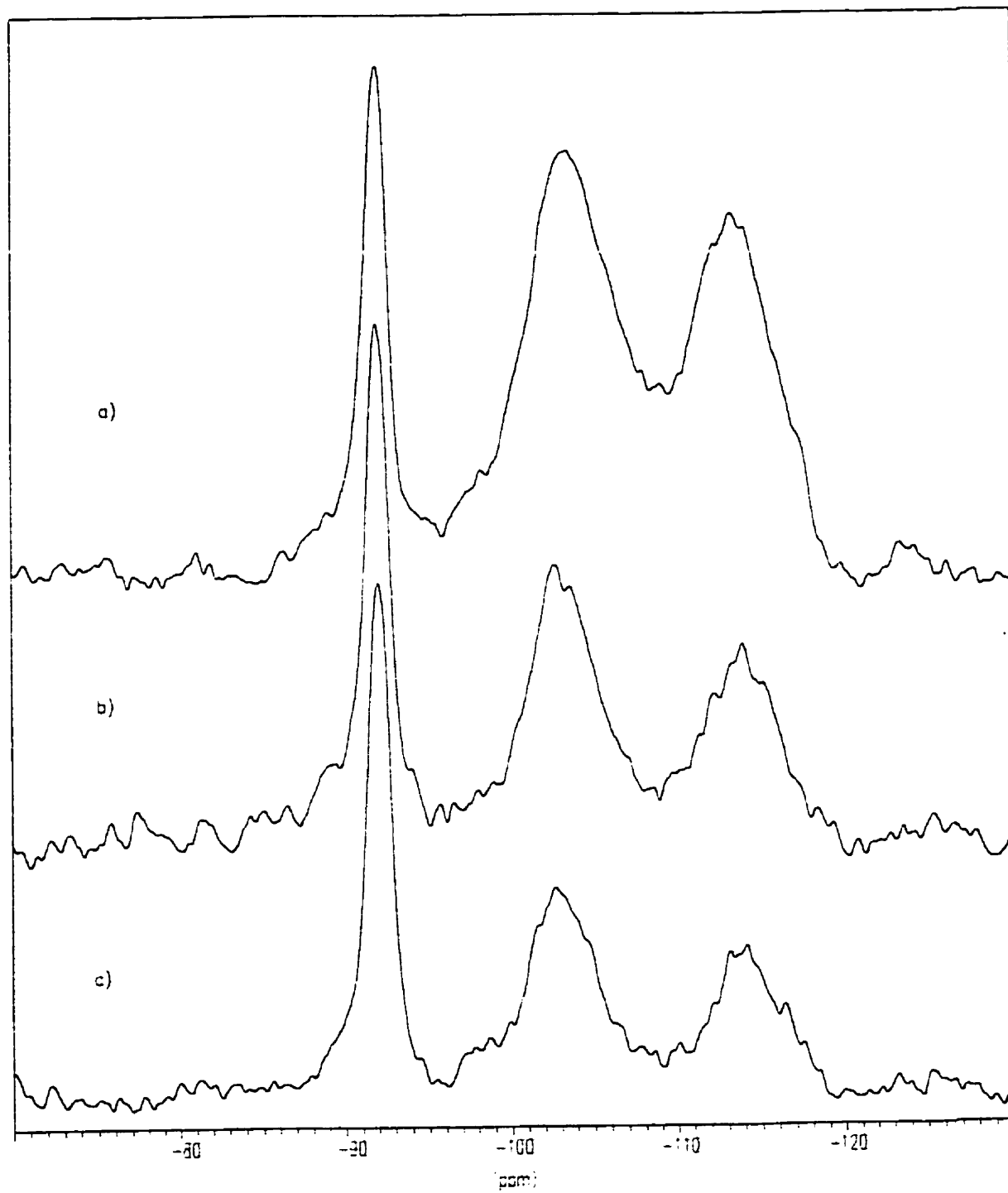


**Figure 3-6.** CPMAS spectra of **a)** pure ZSM-5 ( $\text{SiO}_2/\text{Al}_2\text{O}_3=50$ ), **b)** pure ZSM-5 ( $\text{SiO}_2/\text{Al}_2\text{O}_3=280$ ), **c)** ZSM-5 ( $\text{SiO}_2/\text{Al}_2\text{O}_3=280$ ) loaded with 2.5 wt. %  $\text{TiO}_2$ .

Results, calculated by two methods (integration and deconvolution followed by peak area measurement), are collected in Table 3-1. Both calculations show that, first, pure zeolite has the highest amount of surface Si-OH groups, second, that both {2.5 wt. % TiO<sub>2</sub>} and {5 wt. % TiO<sub>2</sub>} samples have approximately same surface Si-OH coverage remaining after TiO<sub>2</sub> loading (since the peak area under -104 ppm signal remains closely similar), and finally, that {10 wt. % TiO<sub>2</sub>} sample has the lowest content of surface Si-OH groups.

**Table 3-1.** Quantitative estimation of “surface Si-OH groups” relative to the kaolinite standard (STD) as the ratio of the -104 ppm peak to the -93 ppm peak.

	“Surface Si”/ STD, (-104 ppm / -93 ppm )			
	Pure ZSM-5	2.5% TiO <sub>2</sub>	5% TiO <sub>2</sub>	10% TiO <sub>2</sub>
Intensity of -104 ppm peak	0.83	0.59	0.68	0.48
Integrated areas of the peaks	2.83	2.35	2.29	1.74
Deconvoluted areas of the peaks	2.65	2.17	2.10	1.62

The experimental data may be interpreted in the following way: titanium oxide creates Ti-O-Si bonds with the zeolite when it is added in the amounts up to about 2.5 wt. %. Further additions of TiO<sub>2</sub> (up to 5 wt. %) do not lead to the formation of new bonds between titania and zeolite. Instead, titanium oxide tends to aggregate on top of existing titanium species forming a Ti phase that minimizes the surface area of the phase as surface free energy considerations require. In other words, a titanium oxide phase grows preferentially above some critical mass. Larger additions of titania (e.g. to 10 wt. %) lead to further growth of the titanium oxide phase. If TiO<sub>2</sub> crystallites grown at the surface are large enough, they can be sensed by X-ray powder diffraction technique. The following are the results of XRD analysis of the supported photocatalyst.

### 3.3.2. XRD analysis

XRD analysis of {2.5 wt. %}, {5 wt. %}, and {10 wt. % TiO<sub>2</sub>} on ZSM-5, indeed, support the idea of the preferential titania growth above some critical mass. XRD pattern of 10 wt. % TiO<sub>2</sub> exhibits peaks at angles corresponding to those for anatase crystals, but with the line width which suggest a very small particle size. Particle sizes calculated from standard equations are smaller than the particle size in the colloids used for loading. At low loading (2.5 wt. % and 5 wt. %), no sign of TiO<sub>2</sub> crystallinity can be resolved, the XRD pattern is broad and featureless ( Fig. 3-7). The results are similar to [1.15]. The absence of lines from the crystalline phase at low loading does not necessarily rule out the presence of small ordered particles of TiO<sub>2</sub>. The small size of the crystallites causes significant broadening in XRD powder patterns and the X-ray pattern of the support complicates resolution.

### 3.3.3. BET Analysis

Surface area measurement indicates that there is a slight decrease of the specific surface area with loading TiO<sub>2</sub> on the zeolite. Specific surface areas of a pure support and ZSM-5 covered with different loading of TiO<sub>2</sub> are shown on Fig.3-8. It should be noted that TiO<sub>2</sub> particles can not penetrate the pores of ZSM-5 zeolite, since its pore diameters do not exceed 0.5 - 0.6 nm. The colloidal particles used to load ZSM-5 are larger than 10 nm and earlier EFTEM results from our group show that TiO<sub>2</sub> particles in the colloid do not lead to TiO<sub>2</sub> in the interior of the zeolite if the colloidal particles are even slightly larger than the zeolite pore opening<sup>3,10</sup>. Therefore, all of titania loading should be on the surface.

BET results allows one to measure the area of the zeolite covered by TiO<sub>2</sub>. For example, for 2.5wt. % loading on ZSM-5(Si/Al=50), it is equal to 11%. If the interpretation of titanium oxide growth suggested is correct, then it is possible to estimate theoretically what part of ZSM-5 surface would be covered by a hypothetical anatase monolayer of a given weight using lattice parameters of anatase. According to JCPDS data<sup>3,11</sup>, the tetragonal unit cell has the following parameters: a=0.3776 nm and c=0.9486 nm.

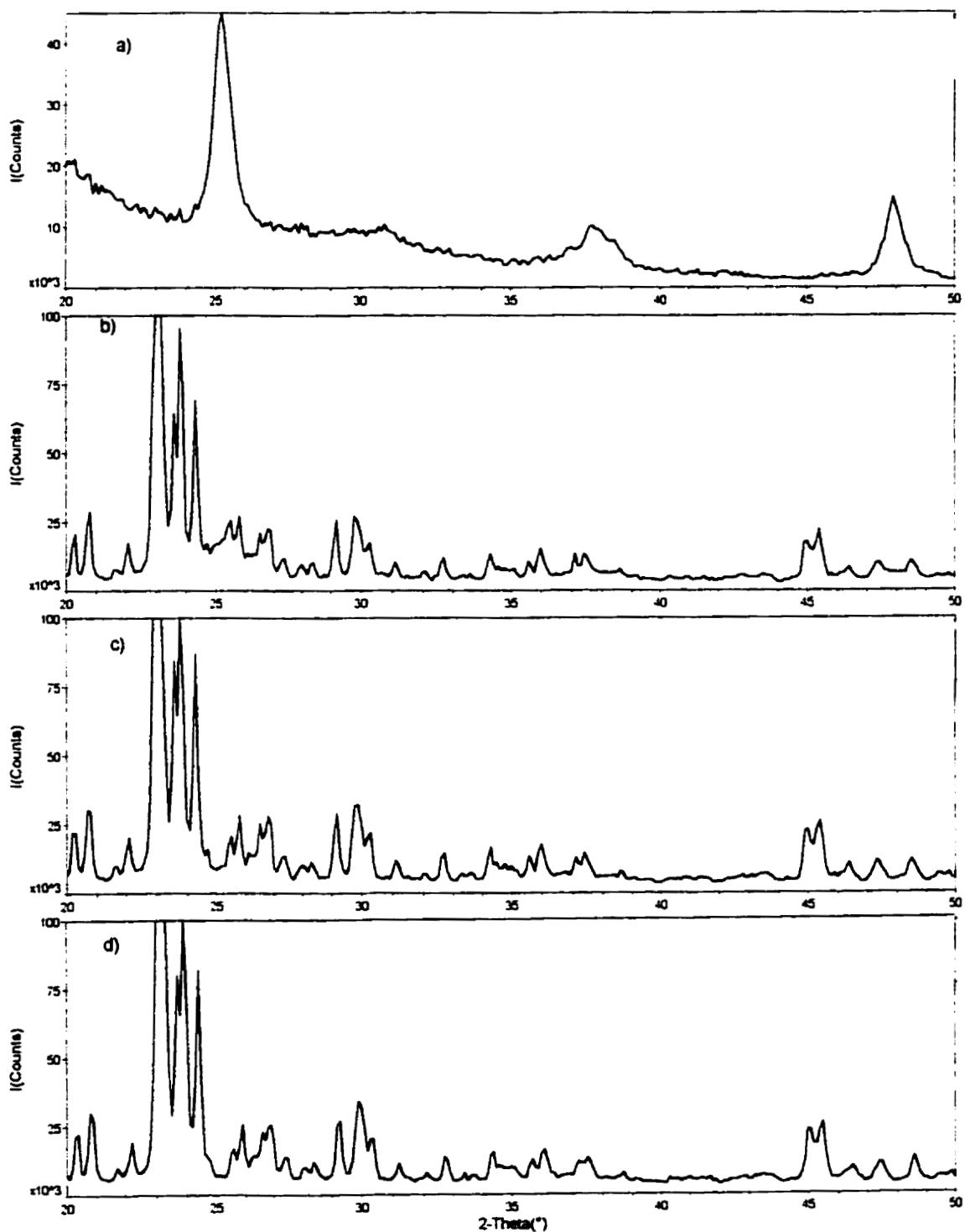


**Figure 3-7.** X-ray powder diffraction patterns of a)  $\text{TiO}_2$  calcined at  $450^\circ$ , b) 10 wt. %  $\text{TiO}_2$ , c) 2.5 wt. %  $\text{TiO}_2$ , d) pure ZSM-5 ( $\text{SiO}_2/\text{Al}_2\text{O}_3=50$ ).

Assuming that a hypothetical titania monolayer has a thickness of 0.3776 nm, one can calculate the surface that would be covered by one unit cell. Then, it is possible to calculate the covered surface area using the number of particles in 2.5 wt. %  $\text{TiO}_2$  and the specific surface area of ZSM-5 from BET measurements. The theoretical calculations, shown in Appendix 1, suggest that a layer of 2.5 wt. % covers from 10 % to 20 % of zeolite surface (depending on which side of the unit cell, long or short one, it is anchored to the surface). The theoretically estimated  $\text{TiO}_2$  coverage, of 10%-20%, is in a striking agreement with the surface not covered by titanium oxide from NMR. CPMAS measurements shown in Table 3-1 give 16%-18% (for the integrated and the deconvoluted -104 ppm peak area respectively).

The calculations and the NMR experiment suggest that  $\text{TiO}_2$  is not covering the whole surface as the  $\text{TiO}_2$  phase grows. It probably corresponds to growth of  $\text{TiO}_2$  islands from favorable nucleation sites that are saturated at about 2.5 wt. % coverage. The next question is how  $\text{TiO}_2$  is distributed over the surface of the zeolite. Can the growth sites for  $\text{TiO}_2$  be identified? These issues are addressed using Scanning Electron Microscopy and Energy Filtered Transmission Electron Microscopy to map Ti atoms on the zeolite.

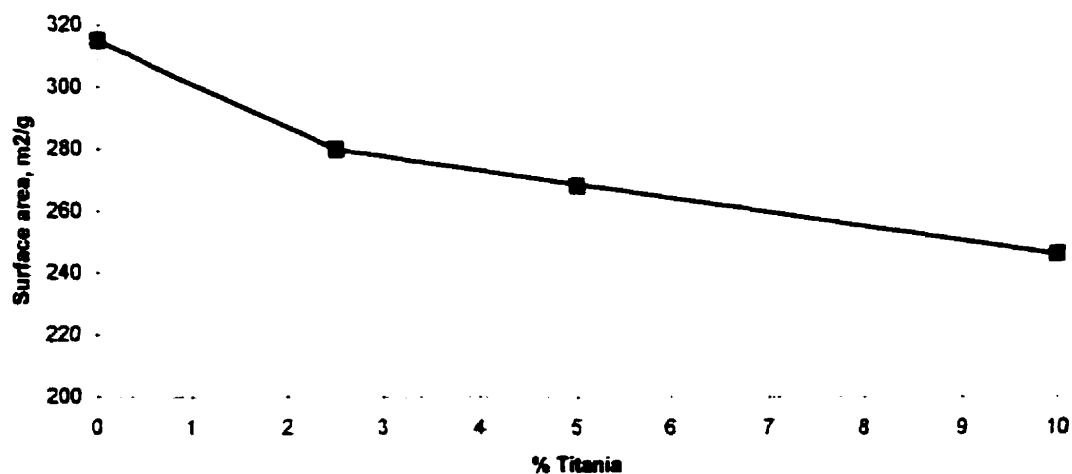


**Fig. 3-8.** Surface area measurements of ZSM-5 (Si/Al=50) with different titania loading.

## Chapter Four

# Investigation of Distribution of Titania over the Surface of the Zeolite by SEM and EFTEM Techniques

### 4.1. Introduction

In order to obtain a complete characterization of the composite photocatalyst, it is necessary to have a representation of its microstructure. Direct visualization of the catalyst morphology can help in identifying critical factors in catalytic properties. Modern scanning and transmission electron microscopy techniques provide powerful tools for direct visualization of the microstructure. For example in [4.1], TEM was used to characterize the structure of hydrous  $\text{TiO}_2$  precipitates and their aging products. SEM is a widely used technique to investigate surface morphology and produce a semi-quantitative elemental composition of the surface using the X-ray emitted by the elements after primary electron beam irradiation<sup>1,2</sup>. EELS allows the determination of the local elemental composition of regions from spectra of energy losses that contain ionization edges resulting from inner shell excitations characteristic of the elements of the catalyst<sup>1,20</sup>. In conjunction with energy filtered imaging, this spectroscopy allow elemental mapping to be obtained from regions as small as 1 nm in diameter<sup>4,3</sup>. The EFTEM has been used for mapping various elements range from hydrogen to uranium as described in<sup>4,3-4,4</sup>.

In this chapter, the application of SEM and EFTEM techniques to determining the titanium distribution on the composite photocatalyst  $\text{TiO}_2 + \text{ZSM-5}$  is described.

### 4.2. Apparatus

#### 4.2.1. Scanning Electron Microscopy

Examination of TiO<sub>2</sub> distribution on the surface of support was performed on Kevex SEM (Cambridge Stereoscan 250) operated at 20kV. The instrument was coupled with an emission microprobe and linked to an Analytical Spectrometer 6100 data processor. A semi-quantitative elemental analysis of the surface was done by monitoring microprobe X-ray emissions using the K<sub>α</sub> lines of Ti and Si. The powders were supported on carbon stubs.

#### ***4.2.2. Energy Filtered Transmission Electron Microscopy***

Energy loss micrographs were recorded with a Zeiss EM902 instrument equipped with electron imaging spectrometer. The instrument operated at an accelerating voltage of 80 kV. A 500 μm condenser aperture, a 60 μm objective aperture, and a 20 eV energy selecting split aperture were used. Images were recorded at a magnification of x20000 using retractable Gatan MultiScan CCD camera. The procedure was similar to the one described in<sup>3 10</sup>. Two images were recorded: one at the titanium L-shell ionization edge, which occurs at 456 eV, and a reference image at the energy loss before the ionization edge at 430 eV. Energy-loss spectra were processed with ERGO-vista 4.4 software to produce the net Ti image. Processing involved normalizing the two digitized images over background regions, subtracting the background contribution, and integrating the ionization edge intensity.

Samples were imbedded in QUETOL, thin-sectioned with an ultramicrotome to sections 40nm thick and mounted on copper grids as described in<sup>1 19</sup>.

### **4.3. Results**

#### ***4.3.1. SEM Analysis***

The SEM method was used earlier to examine the surface of TiO<sub>2</sub> anchored on a specially prepared zeolite ZSM-5<sup>1 15</sup>. SEM coupled with an emission microprobe provided a view of the surface of TiO<sub>2</sub>-zeolite composite. The preparation method used

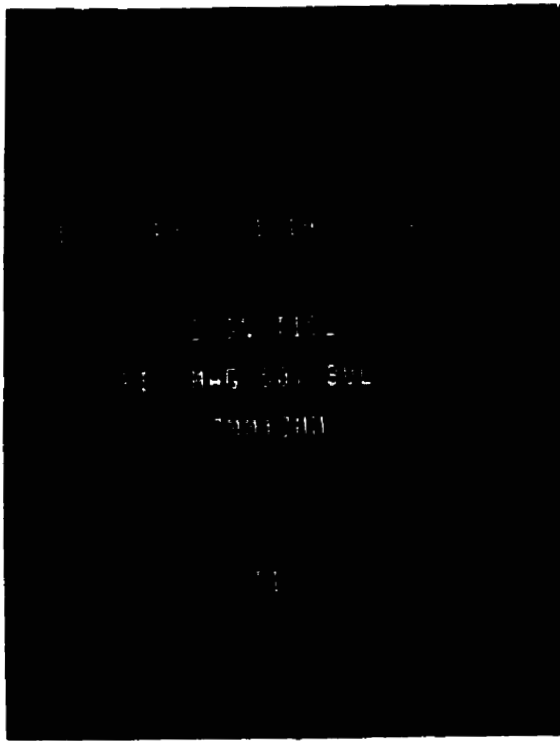
produced an irregular rough surface. Microphotos showed no change in the typical morphology of the support after 2.5% titania loading and no identifiable  $\text{TiO}_2$  particles were resolved at 2.5 wt. % or 5wt. % loading.

Fig. 4-1 and 4-2 show the X-ray emission spectroscopy spot probe analysis done on samples with 2.5 wt. %  $\text{TiO}_2$  and 10 wt. %  $\text{TiO}_2$  loading respectively. It can be seen from Fig. 4-1 (a) and 4-2 (a), that show a representative part of the whole sample, that Ti is present over most of the samples. Further examination of the surface performed at different regions of the sample shows that Ti loading is not uniform. In the 10%  $\text{TiO}_2$  sample, it varies from 8% to 11% in different spots ( particles (b) to (d) in Fig. 4-2 ).

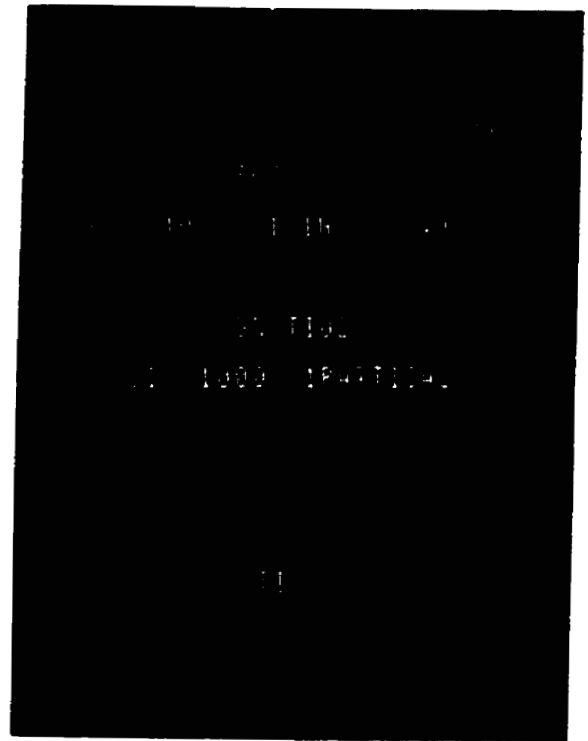
SEM analysis indicates uneven distribution of titania over the sample with high titania content, however it doesn't provide detailed description of the surface at the titanium oxide loading lower than that leading to the formation of anatase crystals.

#### **4.3.2. EFTEM**

Since the efforts to map  $\text{TiO}_2$  using SEM and microprobe elemental analysis were not successful at low coverage, a more detailed investigation using the EFTEM technique were performed. It is known to give two orders of magnitude better resolution. Fig. 4-3 represents a TEM picture of 2.5%  $\text{TiO}_2$  loaded on ZSM-5 (Si /Al=50) where the upper panels (1, 2) represent two pre-edge reference images, and lower panels represent a post-edge Ti-enhanced image (3) and a net image (4). The latter was produced by normalizing the two digitized images over background regions, subtracting the background contribution (pre-edge), and integrating the ionization edge. From the net image, one can see that the surface structure of the sample consists mostly of small point-like primary  $\text{TiO}_2$  particles ( white spots with an average size of 10-20 nm). It should be noted here that we cannot control the orientation of the particles with respect to cutting direction of the ultramicrotome. According to the theory of crystal growth,  $\text{TiO}_2$  is expected to grow at specific surface "defects", since the anatase lattice is quite different from the underlying zeolite lattice. Thus, the surface "roughness" of a support is an essential aspect of the anchoring of  $\text{TiO}_2$ .



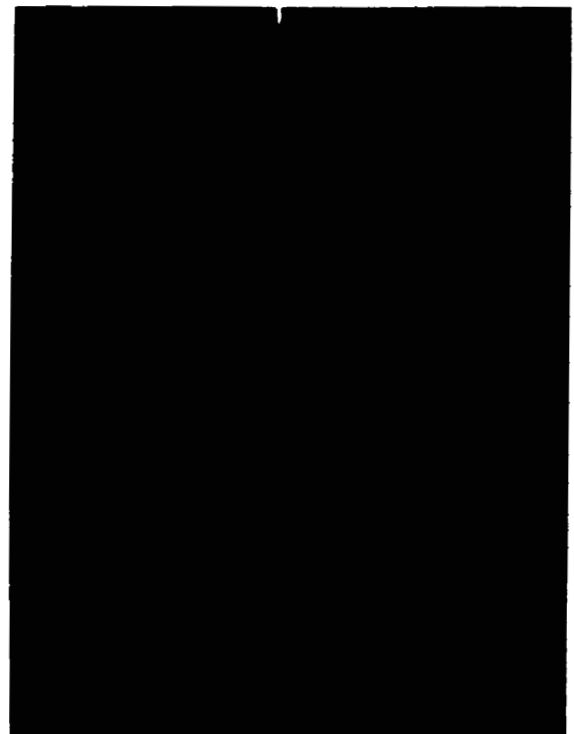
a)



b)



c)



d)

**Fig. 4-1.** X-ray emission spectra of 2.5 wt. %  $\text{TiO}_2$  taken at a representative  $3 \times 3$  mm particle (a), and at its different spots (b), (c), (d).





**Fig. 4-3.** EFTEM picture of 2.5 wt. %  $\text{TiO}_2$  loaded on ZSM-5 ( $\text{SiO}_2/\text{Al}_2\text{O}_3=50$ ) where 1) and 2) are two pre-edge reference images, 3) the post-edge Ti-enhanced image, and 4) the net Ti image after background subtraction and integration of the ionization edge intensity. The size of one panel corresponds to  $2.3 \mu\text{m} \times 2.3 \mu\text{m}$ .

## Chapter Five

### Correlation of Physical Characteristics of TiO<sub>2</sub> with Its Photoactivity

#### 5.1. Introduction

The photocatalytic activity of titanium oxide supported on ZSM-5 was investigated in order to correlate it with physical characteristics of the composite photocatalyst. It has been reported that ZSM-5 is not photocatalytic by itself<sup>15</sup>. For evaluation of photoactivity of TiO<sub>2</sub> supported on ZSM-5, acetophenone was chosen as a model substrate for a test reaction. Acetophenone is a relatively strong organic pollutant and one of the most common test substrate for TiO<sub>2</sub>. It is water-soluble, photochemically inactive, non-volatile, insensitive to pH, and easily analyzed.

The photocatalytic activity was evaluated by measuring the loss of acetophenone in solution. Before irradiating, the composite photocatalyst was equilibrated in the dark to complete acetophenone adsorption on the catalyst. The final concentration of acetophenone in the solution after the process of equilibrating in the dark was used for the calculation of the extent of dark adsorption on the catalyst and also as the initial value for further kinetic treatment of the photocatalytic degradation of acetophenone.

#### 5.2. Experimental Procedures

##### 5.2.1. Chemicals

Titanium (IV) tetraisopropoxide (97%) and acetophenone (99%) were purchased from Aldrich. P25 titanium oxide was a gift from the Degussa Corp. The ZSM-5 zeolites (ammonium form, SiO<sub>2</sub>/Al<sub>2</sub>O<sub>3</sub>=50 and 280) and silicalite were purchased from Zeolyst International. Doubly distilled water was used throughout this work.

A series of samples with 2.5%, 5%, and 10 wt. % of titanium dioxide supported on ZSM-5 were used in this work. The preparation procedure is described in Chapter 3.2.2. A parallel unsupported  $\text{TiO}_2$  powder was also prepared under the same synthetic conditions as the supported samples and used as the control sample throughout this study. Commercial P25 Degussa powder was also used for comparison purposes.

Individual stock solutions of 50-130 ppm (0.42-1 mM) acetophenone were prepared in distilled water. Catalysts were added at 2.0 g/L concentration into 100ml solution of acetophenone.

### ***5.2.2. Photocatalytic procedure***

Since absorption of light by a chosen compound is a first concern for photochemical studies, the UV-vis absorption spectrum of aqueous solution of acetophenone (AP) was obtained. Fig. 5-1 shows the spectrum of acetophenone at the concentration of 100ppm (  $8.4 \times 10^{-4}$  M ) which is a typical concentration used in this work for photocatalytic oxidation. To avoid direct photolysis, a cut-off filter at 320 nm (rejecting 98% of light below 320 nm) has been used to isolate active wavelengths for subsequent experiments.

The light source was a 200 Watt Xe-Hg lamp powered to 0-180 W by a LPS-250 PTI (Photon Technology International) power supply. A photocatalytic reactor consisted of a 120 ml cylindrical Pyrex cell with a quartz window. The container was foil-covered leaving the quartz window exposed to irradiation. A magnetic stirring bar was placed inside the reactor. In all experiments, merely atmospheric oxygen was used as a source of oxygen without any deliberate addition into the vessel.

Sampling from the reactor during irradiation was done using disposable plastic syringes at regular time intervals (20 min, 40 min, 60 min, etc.). The total irradiation time was kept the same for each experiment for the purpose of comparison. A withdrawn sample was filtered through a Millipore membrane filter ( 0.45  $\mu\text{m}$  pore diameter ) and analyzed by the standard methods, either by High Performance Liquid Chromatography (HPLC) and/or Gas Chromatography (GC).

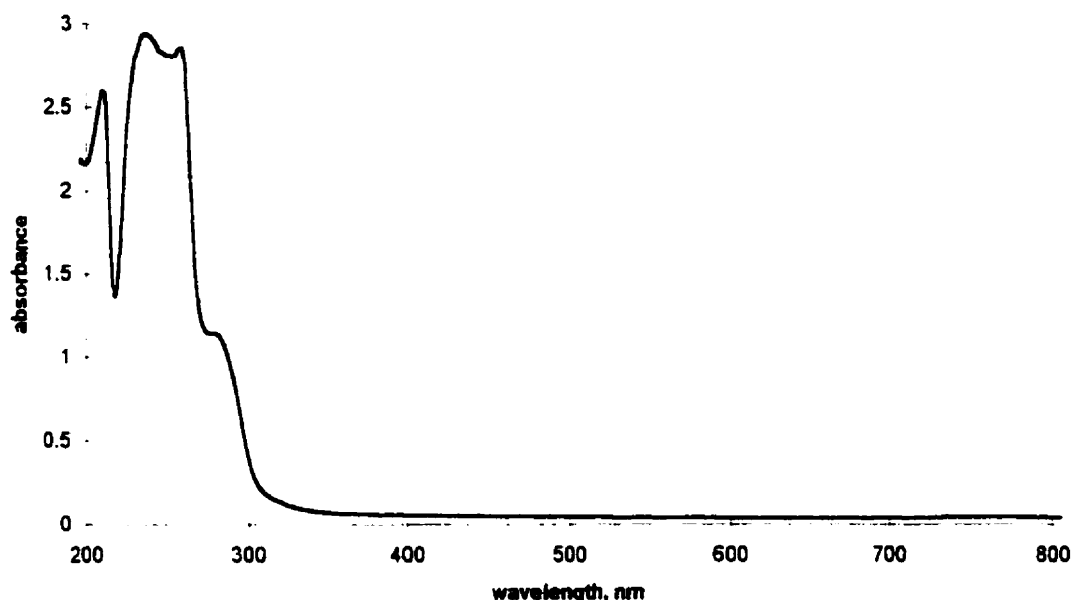


**Fig. 5-1.** The absorption spectrum of acetophenone in water at 100 ppm demonstrating that a 320 nm cut off filter prevents direct excitation.

### **5.2.3. Analytical determination of acetophenone by HPLC and GC.**

The HPLC instrument with a  $C_{18}$  column operated under the following conditions: the wavelength of the UV detector set up at 246 nm. A 50:50 mixture of  $CH_3CN$  and  $H_2O$  was used as eluent with flow rate equal to 1.00 ml/min. The GC instrument was HP 5880 GC with a flame ionization detector and a copper coil column packed with 3% OV-225 on Chromosorb.

Analytical results were calibrated each time using a series of standard solutions corresponding to a range of concentrations used in the experiment. Both instruments have a linear response as shown in Fig. 5-2, 5-3. The difference between results obtained from HPLC and GC does not exceed 4%.

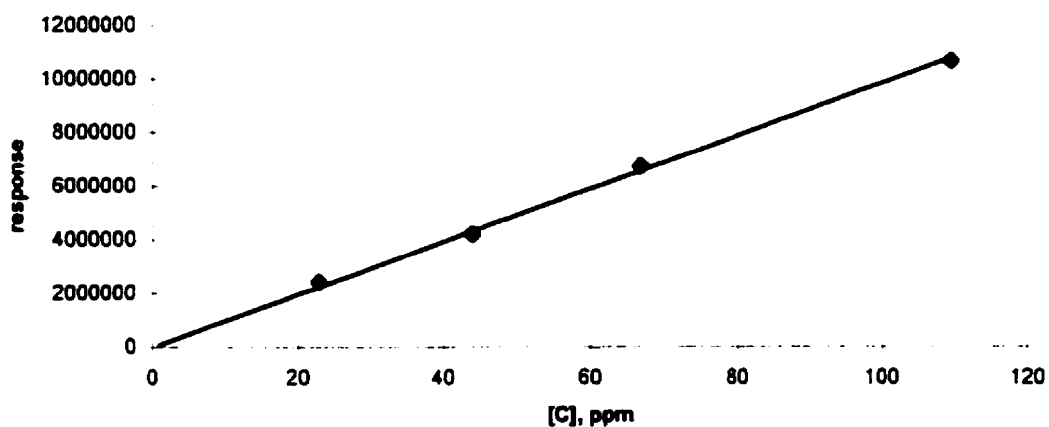


Fig. 5-2. Calibration of HPLC for analysis of acetophenone.

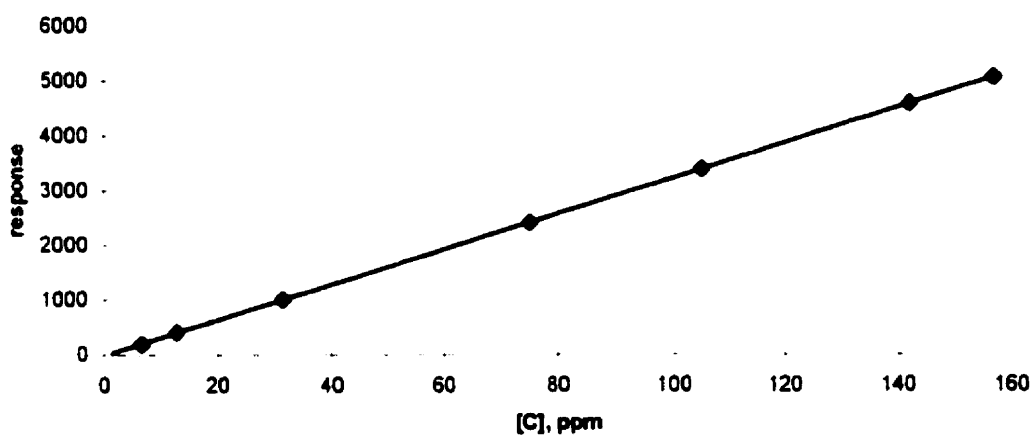


Fig. 5-3. Calibration of GC for analysis of acetophenone

### 5.3. Dark adsorption of acetophenone on the supported catalyst

Since zeolites provide capacity to adsorb organics from aqueous solutions, the relative adsorption capacities of the catalysts supported on the zeolites used in this work were estimated. This was done by stirring a dispersion of a photocatalyst in the acetophenone solution in the dark at a constant temperature. The concentration of acetophenone left in the solution after timed intervals was measured to determine the

extent of adsorption on a catalyst. According to the data shown in the Table 5-1, 1 hour equilibration time was chosen to assure that complete dark adsorption equilibrium was reached (no further decrease of acetophenone concentration in the bulk was detected after more than 1 hour).

The final concentration of acetophenone in the solution after the process of equilibrating in the dark was used for the calculation of the extent of dark adsorption on the catalyst and also as the initial value for further kinetic treatment of the photocatalytic degradation of acetophenone. Fig. 5-4 shows an example of acetophenone adsorption isotherm on different zeolites, where  $C_{bulk}$  is the molar concentration of acetophenone in the bulk at equilibrium and  $N_{ads}$  is the number of moles of acetophenone adsorbed per gram of the zeolite.

**Table 5-1.** Adsorption of acetophenone on a composite catalyst (2.5 wt.% TiO<sub>2</sub>-Zeolite) supported on different zeolites. Initial concentration of acetophenone solution was 128 ppm.

% of acetophenone adsorbed	15 min	60 min
ZSM-5 (SiO <sub>2</sub> /Al <sub>2</sub> O <sub>3</sub> =50)	58%	63%
ZSM-5 (SiO <sub>2</sub> /Al <sub>2</sub> O <sub>3</sub> =280)	87%	92%
Silicalite (no Al <sub>2</sub> O <sub>3</sub> )	91%	98%

As expected, the zeolites used in this work have large adsorptivity for the organic substrate and their adsorption capacities increase with the increase of SiO<sub>2</sub>/Al<sub>2</sub>O<sub>3</sub> ratio. It can also be seen from Fig. 5-4 that adsorption capacity of ZSM-5 (SiO<sub>2</sub>/Al<sub>2</sub>O<sub>3</sub>=50) zeolite reaches a limit at approximately 10<sup>-4</sup>M. According to calculations shown in Appendix 2, acetophenone at this concentration doesn't completely cover the zeolite surface (35% of the BET surface). Thus, it can be assumed that this surface coverage by acetophenone corresponds to saturation of some specific adsorption sites on the surface of the zeolite.

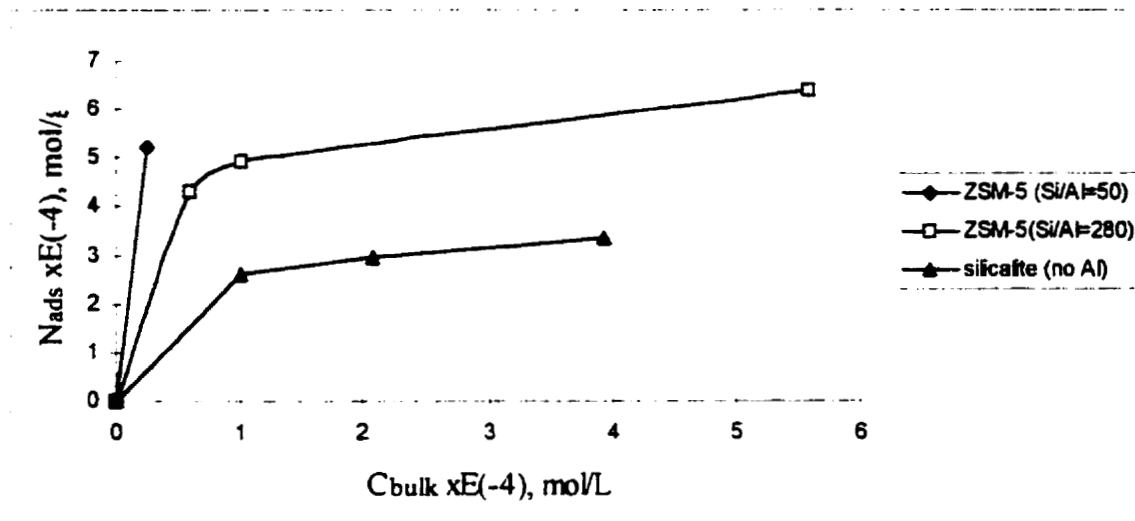


Fig. 5-4. Dark adsorption isotherm of acetophenone on different zeolites.

#### 5.4. Light Intensity Measurements by ferrioxalate actinometry

Before commencing irradiation experiments, it was necessary to evaluate the absolute light intensity of the irradiation. Chemical actinometry was used to measure the light intensity. It is a common practice to use photochemical reactions of certain solutions as a standard for which the quantum yield of corresponding product at a given wavelength has been established. The absolute light intensity can be then obtained by measuring a product formed by photodissociation from reactant. The advantage of utilizing chemical actinometers is that the actinometer can be irradiated under similar conditions to those of the photochemical reactions to be investigated. The commonly used potassium ferrioxalate system  $K_3[Fe^{III}(C_2O_4)_3] \cdot 3H_2O$  was used for photochemical research<sup>5,1</sup>. It has good sensitivity for wavelengths from 254 nm to 480 nm.

When potassium ferrioxalate is exposed to irradiation, ferrous ion  $Fe^{2+}$  is formed. It can be determined spectrophotometrically by the complexation with 1,10 phenanthroline (*phen*) to form the red colored  $[Fe^{II}(\text{phen})_3]^{2+}$  that has absorption maximum at the wavelength 510 nm. The quantum yields  $\phi_{Fe^{2+}}$  for the production of  $Fe^{2+}$ , accurately known in the blue region of the visible spectrum, allow a simple and

rapid actinometric measurements of light intensity during irradiation. The number of ferrous ions formed during irradiation ( $N_{Fe^{2+}} / \text{sec}$ ) and therefore, the light intensity,  $I$ , that is the number of photons emitted per second by Xe-Hg lamp, can be calculated using the Eqn (5.4-1)

$$N_{Fe^{2+}} / \text{sec} = \frac{V_1 \cdot V_3 \cdot N_A \cdot A_{510}}{V_2 \cdot \epsilon_{Fe^{2+}} \cdot l \cdot I} \quad (5.4-1)$$

where  $V_1$  - volume of irradiated actinometer solution;

$V_2$  - volume of an aliquot taken for analysis;

$V_3$  - total volume of flask where the aliquot was diluted;

$N_A$  - Avogadro's number;

$A_{510}$  - measured absorbance of  $[Fe^{II}(\text{phen})_3]^{2+}$  at 510 nm;

$\epsilon_{Fe^{2+}}$  - molar extinction coefficient of  $Fe^{2+}$  complex ( $1.11 \cdot 10^4$  L / mole cm);

$t$  (sec) - time irradiated;

$l = 1$  cm - pathlength

Calculation of the light intensity,  $I$ , were done by Eqn (5.4-2)

$$I(\text{photons} / \text{sec}) = \frac{N_{Fe^{2+}} / \text{sec}}{\phi_{Fe^{2+}} \cdot I_f} \quad (5.4-2)$$

where  $\phi_{Fe^{2+}}$  is a quantum yield for  $Fe^{2+}$  formation ( $1.21 @ 350$  nm), and  $I_f$  is a fraction of the light absorbed by actinometer ( $1.0$  for wavelengths below  $400$  nm).

Aqueous solutions required for the light intensity measurement include:

1. 0.1% 1,10 phenanthroline stored in the dark to prevent photodecomposition of the phenanthroline
2. Buffer diluted to 500 ml:
  - 41 g sodium acetate trihydrate
  - 5 ml conc.  $H_2SO_4$
3. Ferrioxalate solution prepared in the dark:

0.295 g potassium ferrioxalate dissolved in 100 ml 0.1 M H<sub>2</sub>SO<sub>4</sub>

In this investigation, a 30 ml of ferrioxalate solution was irradiated. A 3.00 ml aliquot of irradiated actinometer was quantitatively transferred into a 50.00 ml volumetric flask containing 1.5 ml of buffer and then diluted up to the mark with distilled water. The complex was placed in the dark for one hour prior to analysis. When developed, the solution was analyzed for the absorbance at 510 nm.

Actinometry showed that the whole photon spectrum (photons/sec ) obtained from Xe-Hg lamp powered to 180 W is  $4.2 \cdot 10^{17}$  photons per second. According to a reference provided by PTI Inc, the lamp output is 46.6% in 330-580 nm range.

### 5.5. Photoactivity of TiO<sub>2</sub> supported on ZSM-5

Photodegradation reactions of acetophenone catalyzed by supported and unsupported titanium oxide were studied in this work. For the beginning, to ensure the validity of experimental results, photoactivity of unsupported TiO<sub>2</sub> (Degussa P-25) catalyst was measured and compared with data described by Xu (1995)<sup>1,15</sup>. The extent of acetophenone photodegradation is shown in Fig. 5-5. Present results, obtained from both HPLC and GC, agree with each other within 4% and are 15% lower than measurements done on P25 before. The difference is easily explained by the decrease of the overall light intensity of the irradiation source with time (from  $5.1 \cdot 10^{17}$  to  $4.2 \cdot 10^{17}$  photons/second ).

Photoactivity of supported TiO<sub>2</sub> catalysts was studied next using photodegradation of acetophenone as the test reaction. The loss of acetophenone in the bulk was fitted to Eqn (5.5-1) representing pseudo-first order kinetics.

$$\ln[C'(t)] = -kt + \ln[C_0] \quad (5.5-1)$$

where  $C_0$  is the concentration of acetophenone in the solution after dark adsorption process,  $C'(t)$  is its concentration at a time  $t$  of irradiation, and  $k$  is the apparent rate constant. The apparent rate constant,  $k$ , was not physically interpreted in these

experiments but used as a parameter to measure relative efficiency of acetophenone degradation under different conditions. It is easily obtainable from experimental data since in graphical interpretation,  $k$  is the slope of the curve representing Eqn (5.5-1) plotted as  $\ln[C_0/C(t)]$  versus  $t$ .

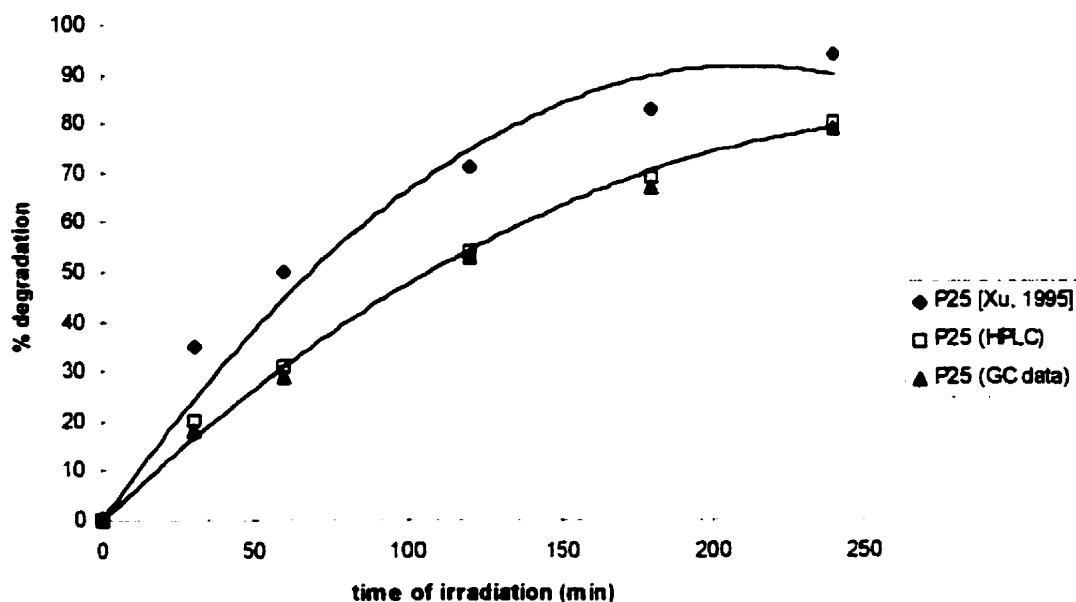


**Fig.5-5.** Photodegradation of acetophenone by  $\text{TiO}_2$  (P25). Initial concentration of acetophenone was 50ppm, mass of the catalyst - 2g/L.

The results of measuring the photoactivity of supported  $\text{TiO}_2$  catalysts show little dependence on the loading of  $\text{TiO}_2$ . The rate constant,  $k$ , reaches its maximal value at 2.5 wt. % loading of titania as shown in Fig. 5-6. This observation is in agreement with previous work<sup>1,15</sup> where the rate constant was reported to increase with the weight of titanium oxide and approach a limit at above about 1g/L. It is interpreted that the limit is approached at a titania loading that is sufficient to use all available photons emitted at a given intensity. Since all available light is already being utilized, no further addition of the photocatalyst can increase the rate of the reaction.

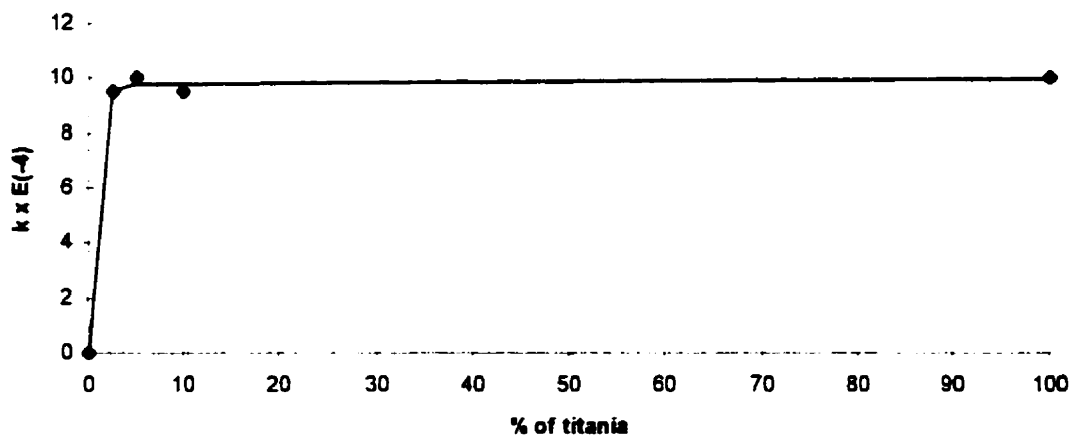


**Fig. 5-6.** Photoactivity of titania supported on ZSM-5 ( $\text{SiO}_2/\text{Al}_2\text{O}_3=50$ ). Initial concentration of acetophenone was 120 ppm.

Dependence of the catalyst activity on the extent of the substrate adsorption was investigated next. Photocatalytic activity of the catalysts was measured at different initial concentrations of acetophenone. Since adsorption of acetophenone on ZSM-5 zeolite is large, the initial concentration of substrate was chosen to be more than 50 ppm (0.4 mM) so as to be able to monitor the change of acetophenone concentration in the bulk solution with time of irradiation.

Photoactivity of the unsupported  $\text{TiO}_2$  catalyst was found to be independent of the concentration of acetophenone. On the other hand, photoactivity of the supported catalyst varies with different acetophenone concentrations. Fig. 5-7 reflects bigger initial rate of substrate decomposition at a higher initial concentration of acetophenone. At the same time, the individual curves show that the higher the initial concentration, the faster the initial reaction rate decreases. Such behavior suggests that Fig. 5-7 is not simply a reflection of acetophenone loss. In earlier papers<sup>1,15, 5,2</sup>, contribution of a secondary photolysis was considered to be significant in systems similar to acetophenone solution. The efficiency of the overall reaction depends on the relative adsorption of the substrate and its product and their relative reactivity. One of the major contributors to the decline in the rate of acetophenone photodegradation might be competition between the reagent and the product for active sites on the surface of the zeolite. The first order kinetics,

usually applied to  $\text{TiO}_2$  photocatalysis, is not applicable here, since it implies strong adsorption of the reagent and minimal adsorption of the product.

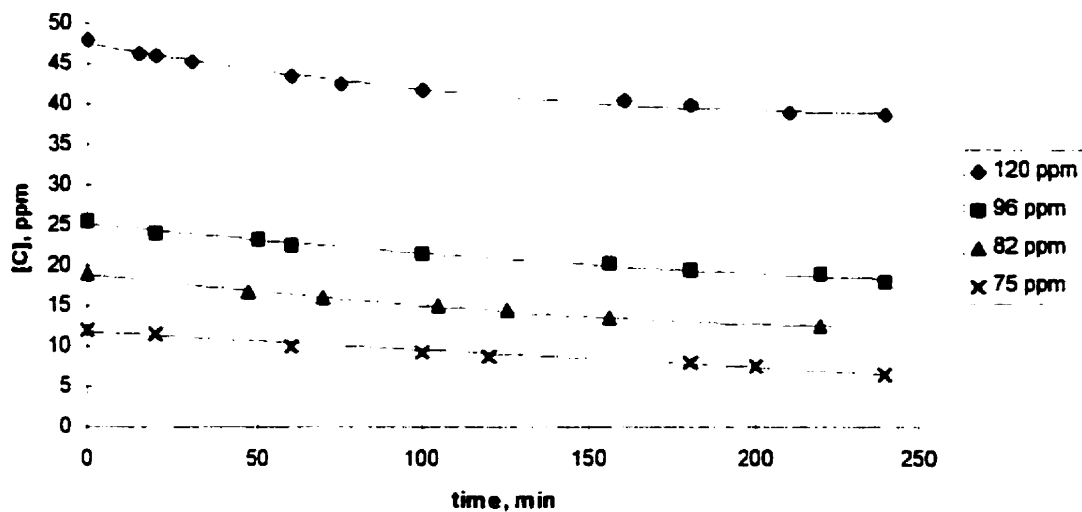


Fig. 5-7. Dependence of the extent of acetophenone photodegradation on its initial concentration.

## Chapter Six

# Application of Supported Photocatalyst for Oxidation of Organics and Decolorization of Pulp Mill Effluents

### 6.1. Introduction

Governments in North America and Europe are beginning to develop a “certified forest product” approach that leads to more stringent requirements on discharges of wastewater from pulp and paper mills. Effective management of wastes is a key component of the “life cycle” dimension of sustainable forest management. To comply with evolving regulatory standards, and to adopt environmental stewardship as corporate responsibility, Canada’s pulp and paper industry is encouraged to take the initiative in significant technological innovations.

As always, a waste management process faces the law of conservation of mass and consideration must be given to the fate of the products of a treatment process. If contaminants are removed from the aqueous phase to render water safe for discharge or useable for recycle, an early question is into what phase are they delivered? For example, adsorption and biological treatment change water pollution to solid waste management problems. The central attraction of advanced oxidation (AO) processes is that organic contaminants are commonly oxidized to CO<sub>2</sub>. The relatively small amounts of organic matter, and the ultimate fate that organic matter might experience under other treatment regimes, does not imply a significant contribution to greenhouses gases. Thus, the advanced oxidation processes offer an attractive option to use the gas phase as the carbon sink.

Our research program has addressed the use of advanced oxidation, specifically schemes based on TiO<sub>2</sub> photocatalysis, in treatment of streams in pulp and paper processing. Our concept encompasses both independent use of AO and use of AO as a supplement to conventional biological treatment processes.

## 6.2. Experimental Section

### 6.2.1. Materials

The present work examined both synthetic and “real” pulp mill white water samples (MWW) from Howe Sound Pulp and Paper Mill supplied to us by UBC group of Prof. J.N. Saddler. The synthetic white water, called a “model” highly recycled white water<sup>6,1</sup>, was made from fresh Spruce-Pine-Fir chips obtained from Canadian Forest Product Ltd. Thermomechanical pulp was made from these chips in PAPRICAN’s pilot plant using a Sunds Defibrator TMP 300 single disk laboratory refiner. The “model” white water was prepared by washing the TMP with distilled water in a batch process. In each batch, 3.6 kg of pulp was washed with 180 L of distilled water at 60° C for 20 min., with stirring. The pulp suspension was dewatered using a screw press to about 45% consistency and the water was collected as white water. The collected white water was used to wash a fresh batch of TMP in order to obtain a recycled white water. After 5 washes, the “model” white water was collected and referred to as the “highly recycled white water”. The MWW contains carbohydrates, lignins, resins and fatty acids, as well as lignans, sterols, steryl esters, and triglycerids. Total concentration of organic matter is 2 - 3%.

Photocatalysts for this research were chosen from a series of catalysts prepared by Dr. A. Starosud in a program conducted in partnership with Trojan Technologies (London, ON). The efforts at Calgary were directed towards the development of an integrated photocatalyst-adsorbent matrix. The integrated matrix approach is a concept that combines adsorption with advanced oxidation by photocatalysis. There is an additional opportunity to gain in photocatalytic efficiency since the problem of encounter of substrate with the photoactive site is reduced from three-dimensional to two-dimensional diffusion. However, the high organic content of the white waters did not require the high adsorption capacity of some of the new catalysts. The optimum catalyst in our series proved to be the “UC-210” material with TiO<sub>2</sub> (P25) from Degussa loaded on silica gel from Grace Davison. Colloidal silica Ludox HS-40 from Aldrich Chemical

Company was used as a solvent. The advantage of the UC series materials is that they retain  $\text{TiO}_2$  reactivity while being based on an inexpensive core that makes them attractively low cost. A parallel unsupported  $\text{TiO}_2$  (P25) powder was also used throughout this study to compare with the supported samples.

### **6.2.2. Photolysis procedures**

Preliminary experiments were performed in sealed test tubes containing 30ml of slurry and a head space of approximately 2ml that were rotated under a 40 W fluorescent bulb with emission centered at 350 nm. The light source had an average intensity  $4 \times 10^{-8}$  einsteins /s. A flow cell ( similar to a fluidized bed reactor) in a Rayonet reactor from Southern New England Nuclear was implemented next. In this latter case, the photocatalyst was retained in the cell by glass wool and centered within the irradiation zone consisting of a ring of 16 75W fluorescent coated Hg tubes which emitted light centered at 350 nm. The average intensity in the cell was  $1.5 \times 10^{-7}$  einsteins /s. The volume of the reaction zone was 10 ml and a total volume of 250 ml of solution was circulated in the flow reactor.

For comparison, some photolysis runs were conducted using UV /  $\text{H}_2\text{O}_2$  scheme. In these experiments, different amount of  $\text{H}_2\text{O}_2$  ( from 0.1% up to 5% of the sample volume ) were added directly into the test tube or into the flow cell where the mixture of MWW and  $\text{H}_2\text{O}_2$  underwent similar to above mentioned irradiation. Finally, a combined scheme using small initiating amounts of  $\text{H}_2\text{O}_2$  with UC-210 was explored. A mixture of 0.2g UC-210, 0.5%  $\text{H}_2\text{O}_2$ , and MWW sample was irradiated the same way to compare with previous experiments.

### **6.2.3. Analytical methods**

High Performance Liquid Chromatography (HPLC) has been employed for monitoring photoproducts and intermediates. The instrument was Waters 600 with  $\text{C}_{18}$  column operated under the following conditions: wavelength of UV detector set up at

240 nm, 50:50 mixture of CH<sub>3</sub>CN and H<sub>2</sub>O used as eluent with flow rate equal to 1.00 ml / min.

The effectiveness of photodegradation of organics was evaluated by comparing chromatograms before and after timed irradiation intervals, to ascertain any changes. Aliquots of 1 ml were drawn from the sample solution and 20 $\mu$ l was injected. Since the samples are complex mixtures, the chromatograms do not provide detailed information about the composition of MWW. However, they provide valuable qualitative information such as indicating differences in degradation pathways under different reaction conditions. As well, disappearance of certain reactant peaks and appearance of certain intermediate peaks provide crude approximations for kinetic parameters. The qualitative HPLC approach had to be adopted for analysis of large numbers of runs because a detailed analysis of the composition of the white waters (see below) is too complex to be applied to results from large numbers of runs.

Detailed analysis of colloidal and dissolved substance content on the samples was done at UBC<sup>6.1</sup>. The white water was extracted with methyl *t*-butyl ether (MTBE) to separate the lipophilic extractives from the highly water solubles<sup>6.2</sup>. Total dissolved and colloidal substances (TDCS) were measured based on dry weight, by oven-drying the water sample at 105 $\pm$ 3 $^{\circ}$  to constant weight. The carbohydrates present in the freeze dried white water samples were measured by HPLC<sup>6.3</sup>. The lignin content was determined as acid-insoluble lignin of the freeze dried extractives from white water sample (Tappi standard method T222). The ash content was measured according to Tappi standard method T211. The extractive groups, resin and fatty acids, lignans, steryl esters, and triglycerides were measured by gas chromatography<sup>6.2</sup>. The water surface tension was measured by the capillary method<sup>6.4</sup>.

## 6.3. Results

### 6.3.1. *Qualitative evaluation using rotating tube reactor*

HPLC analysis of the irradiated MWW, both synthetic and “real”, in the rotating tube indicated that extensive photocatalytic oxidation was definitely taking place at an average light intensity of  $4 \times 10^{-8}$  einsteins /s. Some decolorization of the MWW had been achieved as well. Results of a typical HPLC analysis are shown in Fig. 6-1. Irradiated samples show a decrease in the more non-polar and an increase in the more polar organics, comparing to the initial MWW. These changes are more obvious with an increase of the photocatalyst loading as shown in Fig. 6-2.

Since irradiation of waters to which hydrogen peroxide is added is an alternative method for photochemical initiation of oxidation, reactivity using photocatalysts was compared to the  $H_2O_2$  / UV scheme. HPLC analysis showed that both approaches were effective in degrading major components of white water samples, but the pathways were different. This is clearly indicated by the different peak distribution in the chromatograms shown in Fig. 6-3.

The comparability of reactions with the photocatalyst or peroxide suggested exploration of the effectiveness of a mixed approach. Comparing the chromatograms over specific time-frame (Fig. 6-4 - 6-6), although the compounds were not identified, one could notice crucial qualitative differences in the amount of photodegradation occurring among samples irradiated with photocatalyst alone, hydrogen peroxide alone, and in the case of their combination.  $TiO_2$  photocatalysis enhanced by  $H_2O_2$  proved to be significantly superior to either scheme alone. In this case of combined treatment, no more than traces of organics were found in the sample after 6 days of irradiation under 40 W bulb (Fig. 6-6). Also, the sample completely lost color. Half-life, based on the estimation of the initial component with retention time equal 1.04 min., was approximated as 0.5 day.

Fortunately, it turns out that enhancement of  $TiO_2$  reactions does not require stoichiometric amounts of hydrogen peroxide. Fig. 6-7 shows that the rate of decomposition has a maximum at 1 % of  $H_2O_2$  in the mixture. With less amount of  $H_2O_2$ , the reaction goes slower, but when the concentration of hydrogen peroxide is bigger than 1%, it seems to suppress further destruction of the components. Moreover, further additions of  $H_2O_2$ , after a time for the initial small charge to be consumed, does not

produce any increase on reactivity in the presence of the photocatalyst. Fig. 6-8 - 6-9 show that everyday injections of hydrogen peroxide, being a continuous source of new hydroxyl radical, lead to the formation of the biggest amount of a component with retention time equal 1.15 min but these injections also prevent this component from further destruction. Fig. 6-9 also shows that interruption of  $H_2O_2$  injections allows this component to degrade as before.

Thus,  $H_2O_2$  functions as an initiator only at the outset of irradiation. A main limit of the  $H_2O_2$  technology is the cost of hydrogen peroxide. Since only a small initiator addition is required in the presence of the photocatalyst, cost of its use can remain low.

A remarkable feature of figures 6-4 - 6-6 is that, once again, the pattern of peaks for  $TiO_2$  photocatalysis enhanced by  $H_2O_2$  is novel. The pathway of oxidation is not equivalent to either that with UC-210 acting alone, or  $H_2O_2$  acting alone. Comparing the action of hydrogen peroxide alone with that with the combined approach, one can notice that the intermediate component with retention time equal 1.15 min was produced in both cases during very first day of irradiation but then, it behaved differently over time. In the latter case, this component concentration went through the maximum on a second day of irradiation and later decrease to almost zero after 6 days of irradiation, while in the former case this component, once formed, didn't seem to decompose even after 10 days of irradiation. Taken together, these experiments suggest an organic chain mechanism of oxidation that is taking place. The hydrogen peroxide acts as a initiator, which generates organic radicals, which then react with intermediates from photocatalyzed oxidation to generate a radical chain and faster overall oxidation.

Similar experiments have been made with commercial P25  $TiO_2$  alone as well as in combination with hydrogen peroxide (Fig. 6-10 - 6-11). The pathways of reactions were apparently similar for cases when supported photocatalyst, UC-210, was used alone and in a mixed approach. At initial stage, photocatalysis of MWW was faster with unsupported  $TiO_2$ , although it can be explained by the presence of a larger amount of photocatalyst. Since equal loading of catalysts were used throughout the experiments, the real concentration of unsupported  $TiO_2$  was 20 times more then for the supported  $TiO_2$ . However, the initial extent of photodegradation by unsupported  $TiO_2$  has not been

significantly increased over a time of the irradiation while supported  $\text{TiO}_2$  left only traces of organics after 6 days of irradiation. It's worth mentioning that unsupported  $\text{TiO}_2$  itself became very dark at the end of the experiments which can be explained by contamination of its surface that prevents it from further activity.

### ***6.3.2. Product analysis of output from flow reactor***

Flowing samples were irradiated in the Rayonet based flow reactor for up to 96 hours using the combined UC-210 /  $\text{H}_2\text{O}_2$  scheme in comparison to use of UC-210 alone and 1%  $\text{H}_2\text{O}_2$  alone. Detailed analyses, which characterized the major components of the white water, were performed at UBC on the final samples from these runs. The results confirm successful mineralization of dissolved and colloidal substances in white water samples. The successful oxidation of colloidal material is an especially important result since it might be assumed that only dissolved organic matter could reach reactive sites on the solid state photocatalyst. Results of analyses, where “%” represent degree of loss of each of the important classes of the input stream treated in a Rayonet system for 96 hours, are collected in Table 6-1.

## **6.4. Conclusion**

The experiments to date clearly demonstrate that photocatalysis using UC-210 can achieve oxidation of both dissolved and colloidal organic matter in a white water system at interesting rates. Color reduction can also be achieved. We foresee two points in current mill operation where it will be of interest to design a photochemical reactor. One is for the acid stream. This will require a high rate configuration with high intensity UV lamps. The other is as a supplement and enhancement of treatment ponds. Pond residence times are long enough to allow consideration of solar radiation as the light source.

**Table 6-1.** Analyses of samples from treatment of Mill White Water from Howe Sound mill in flow reactor for 96 h.

Contaminant	Initial MWW	UC-210		1% H <sub>2</sub> O <sub>2</sub>		UC-210+1% H <sub>2</sub> O <sub>2</sub>	
	mg / L	mg / L	%	mg / L	%	mg / L	%
Total dissolved & colloid organics	2360	1120	48	340	14	160	7
Lignin	100	80	80	7.5	7.5	15	15
Carbohydrates	1560	670	43	n / d	0	n / d	0
Extractive resins & fatty acids*	14	20.5	146	58.3	416	15.4	110
Sterols & Lignans	88	34.3	39	26.6	30	16.4	19
Steryl Esters & Triglycerids	16	12.3	77	11.3	71	9.9	62

\* There is noticeable early production of resins and fatty acids from larger MWW substances although the extent is quite different in the different cases.

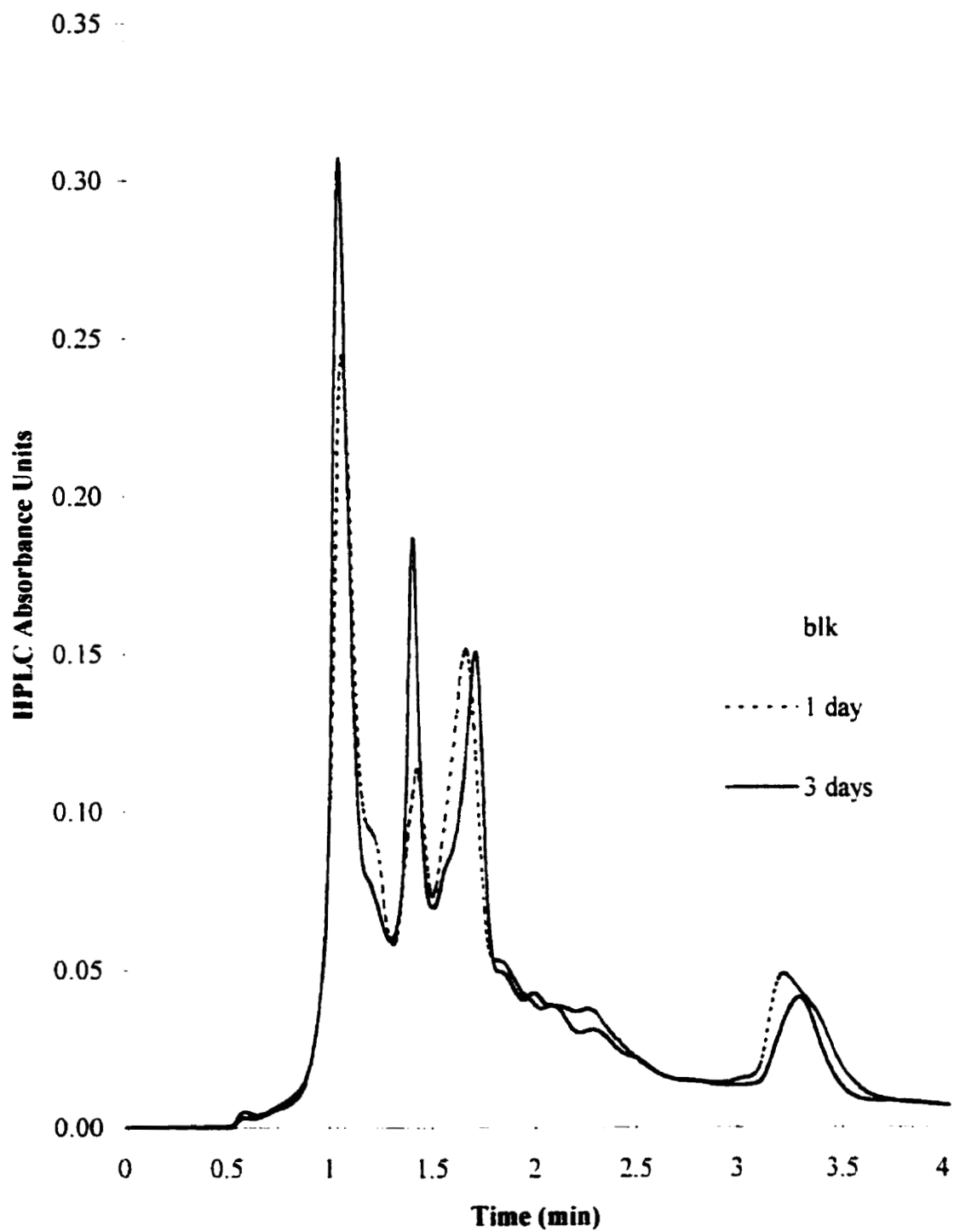


**Fig. 6-1.** HPLC Chromatograms Showing Photolysis Products of MWW after 1 and 3 days in the Rotating Tube with 0.5 g of UC-210.

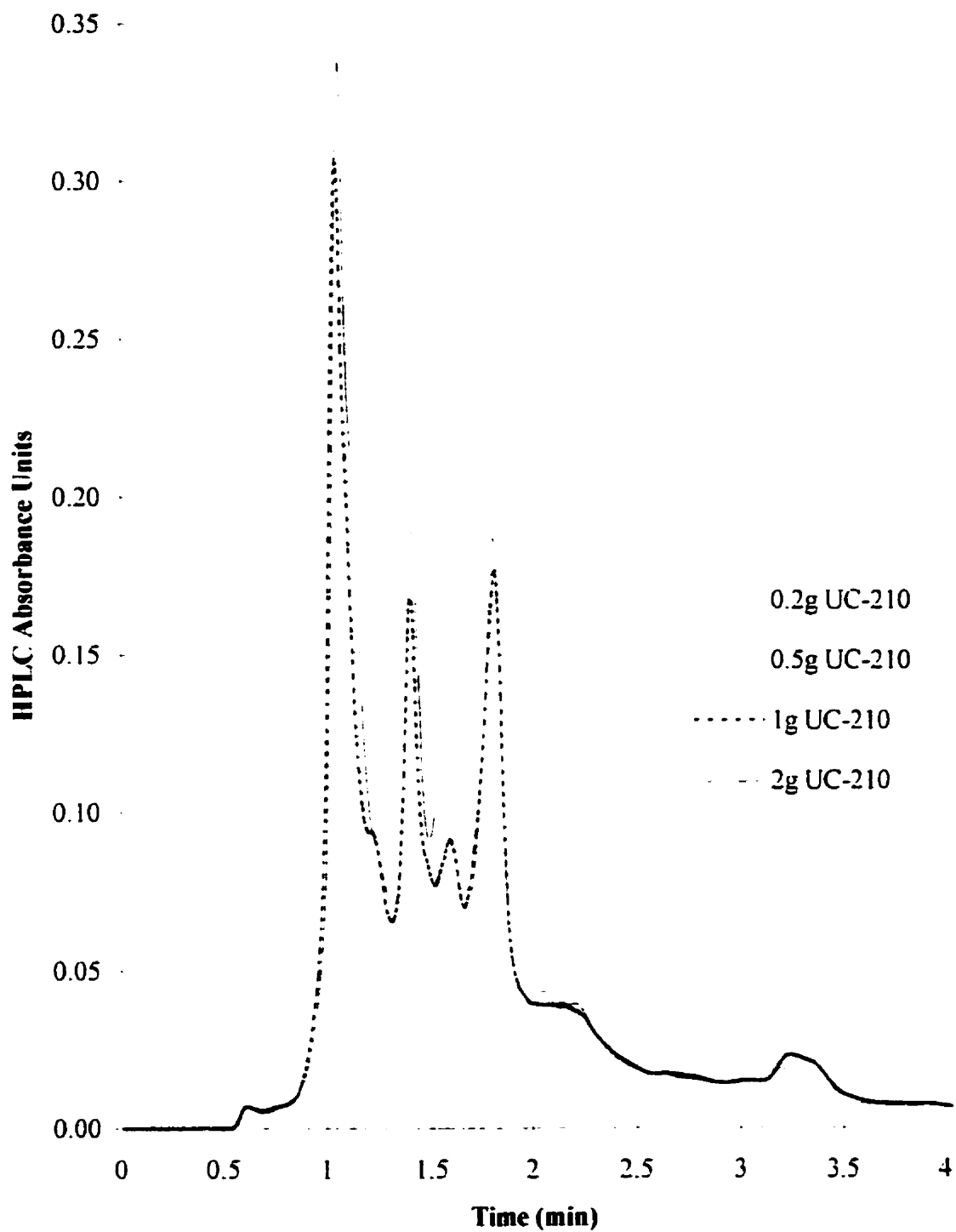


**Fig. 6-2.** HPLC Chromatograms Showing Photolysis Products of MWW under Rotating Irradiation with different loading of Material 210 after 10days.

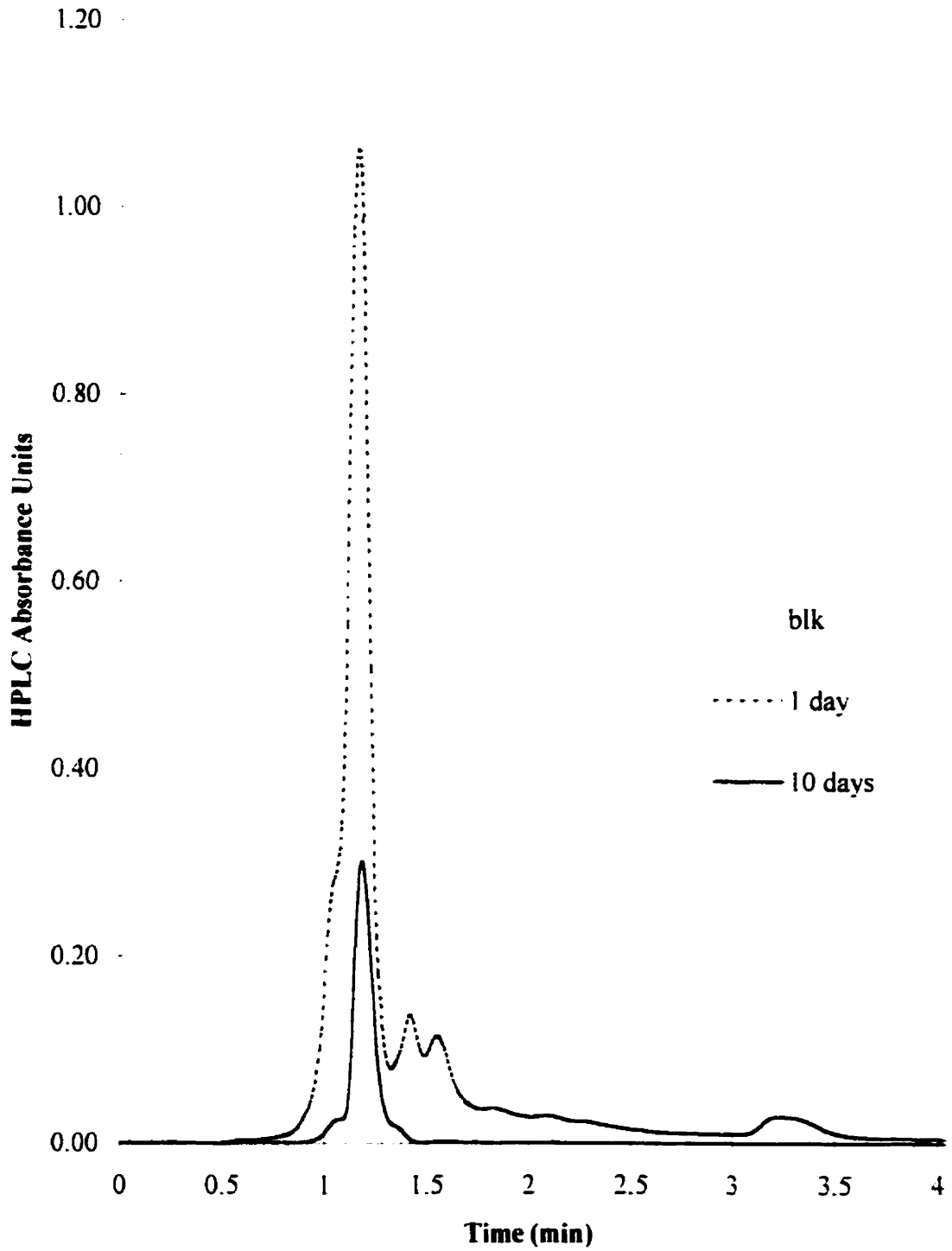


**Fig. 6-3.** HPLC Chromatograms Showing Photolysis Products of MillWW with 0.5% H<sub>2</sub>O<sub>2</sub> after 1 and 10 days under Rotating Irradiation.

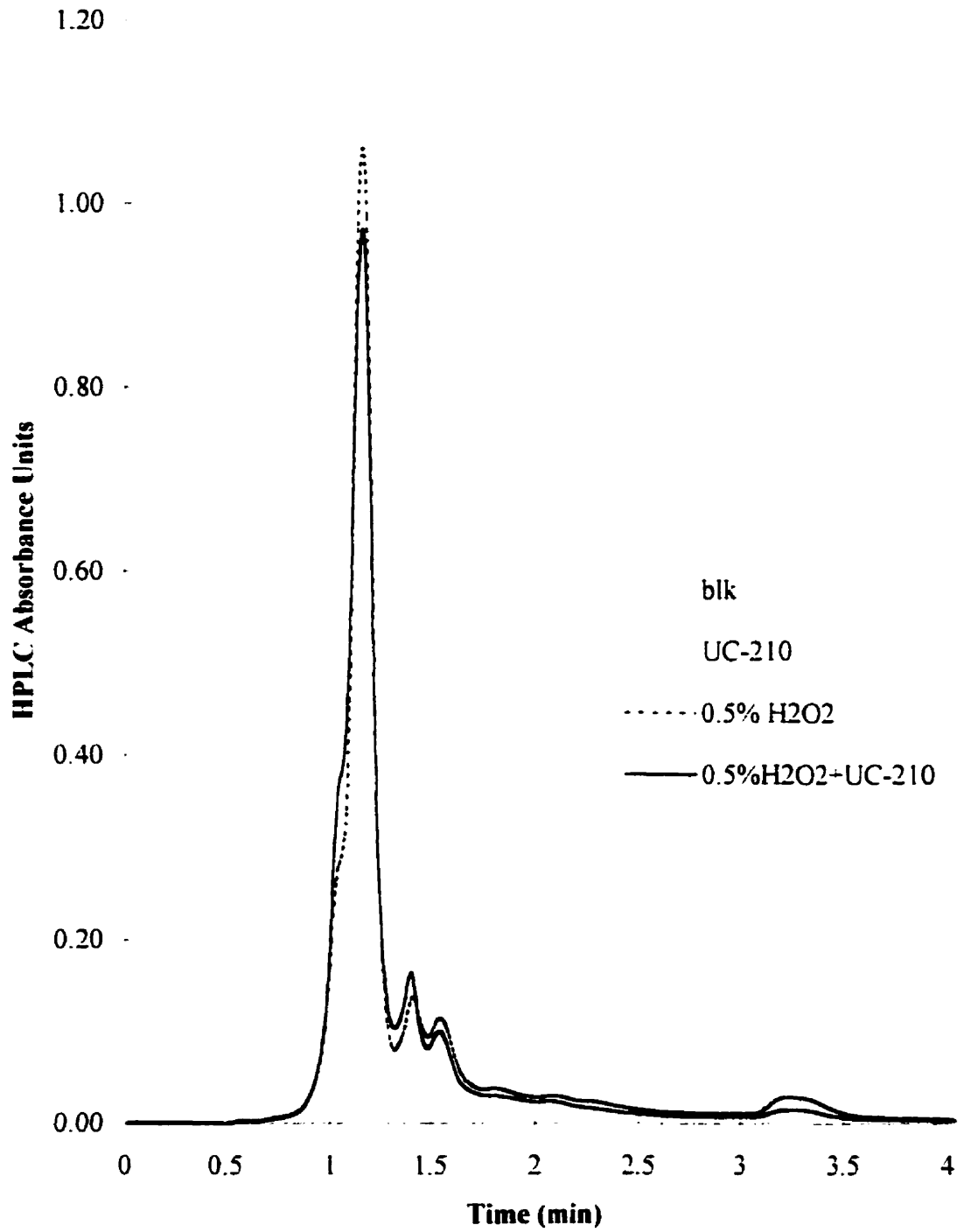


**Fig. 6-4.** HPLC Chromatograms Showing Photolysis Products of MillWW with 0.5g UC-210 and 0.5% H<sub>2</sub>O<sub>2</sub> after 1 day under Rotating Irradiation.

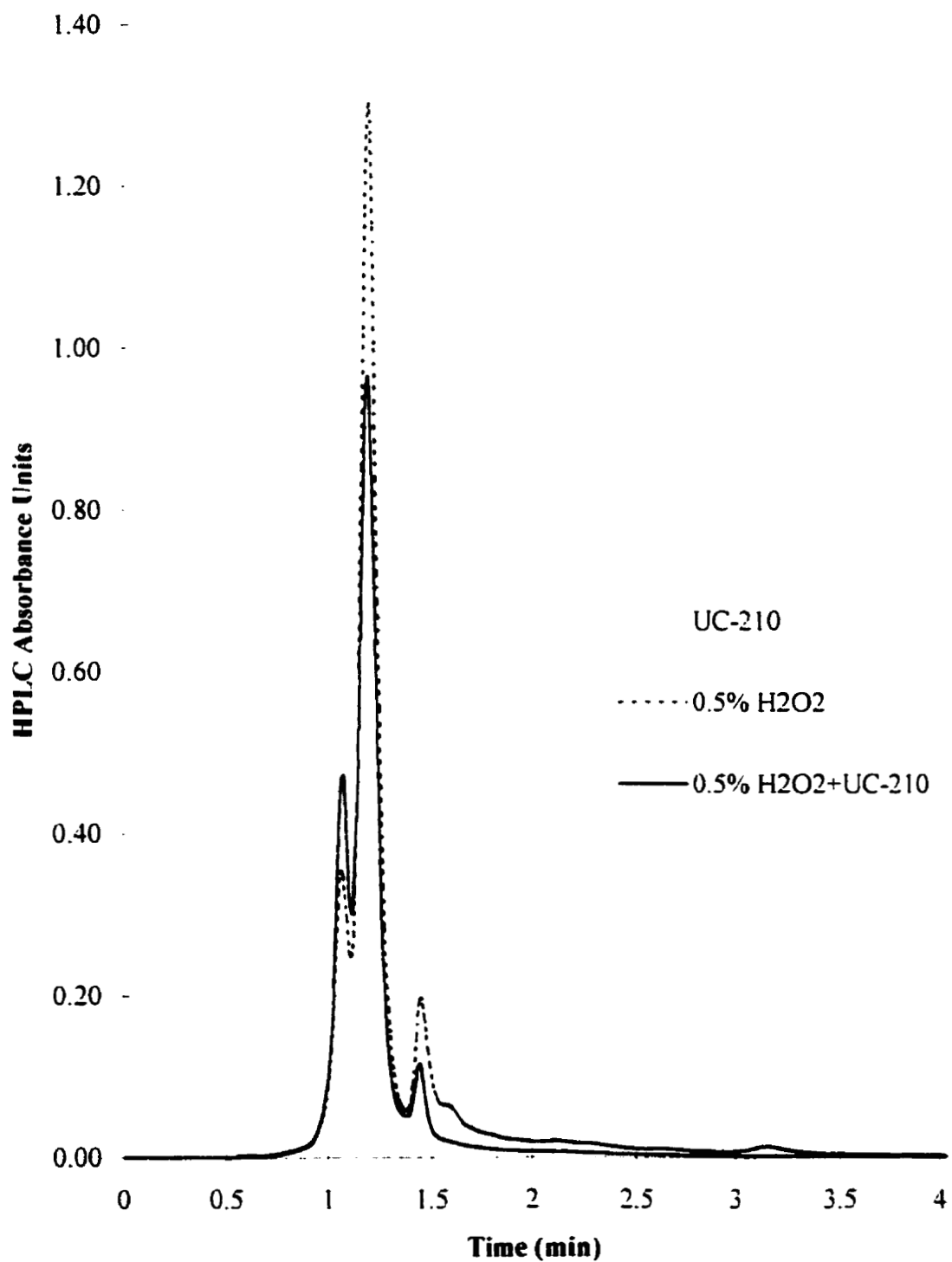


**Fig. 6-5.** HPLC Chromatograms Showing Photolysis Products of MWW with 0.5g UC-210 and 0.5% H<sub>2</sub>O<sub>2</sub> after 2 days under Rotating Irradiation.

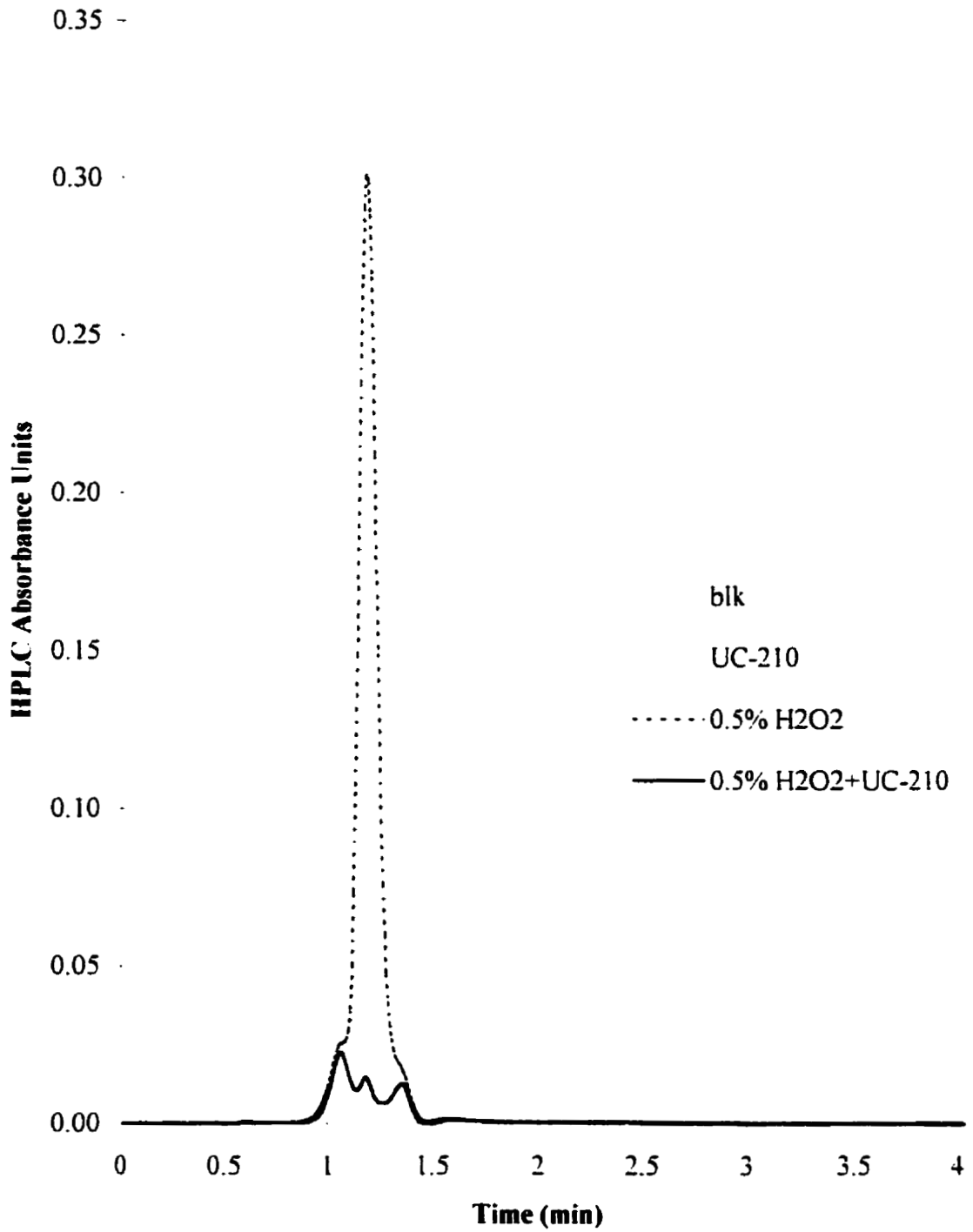


**Fig. 6-6.** HPLC Chromatograms Showing Photolysis Products of MillWW with 0.5g UC-210 and 0.5% H<sub>2</sub>O<sub>2</sub> after 6 days under Rotating Irradiation.

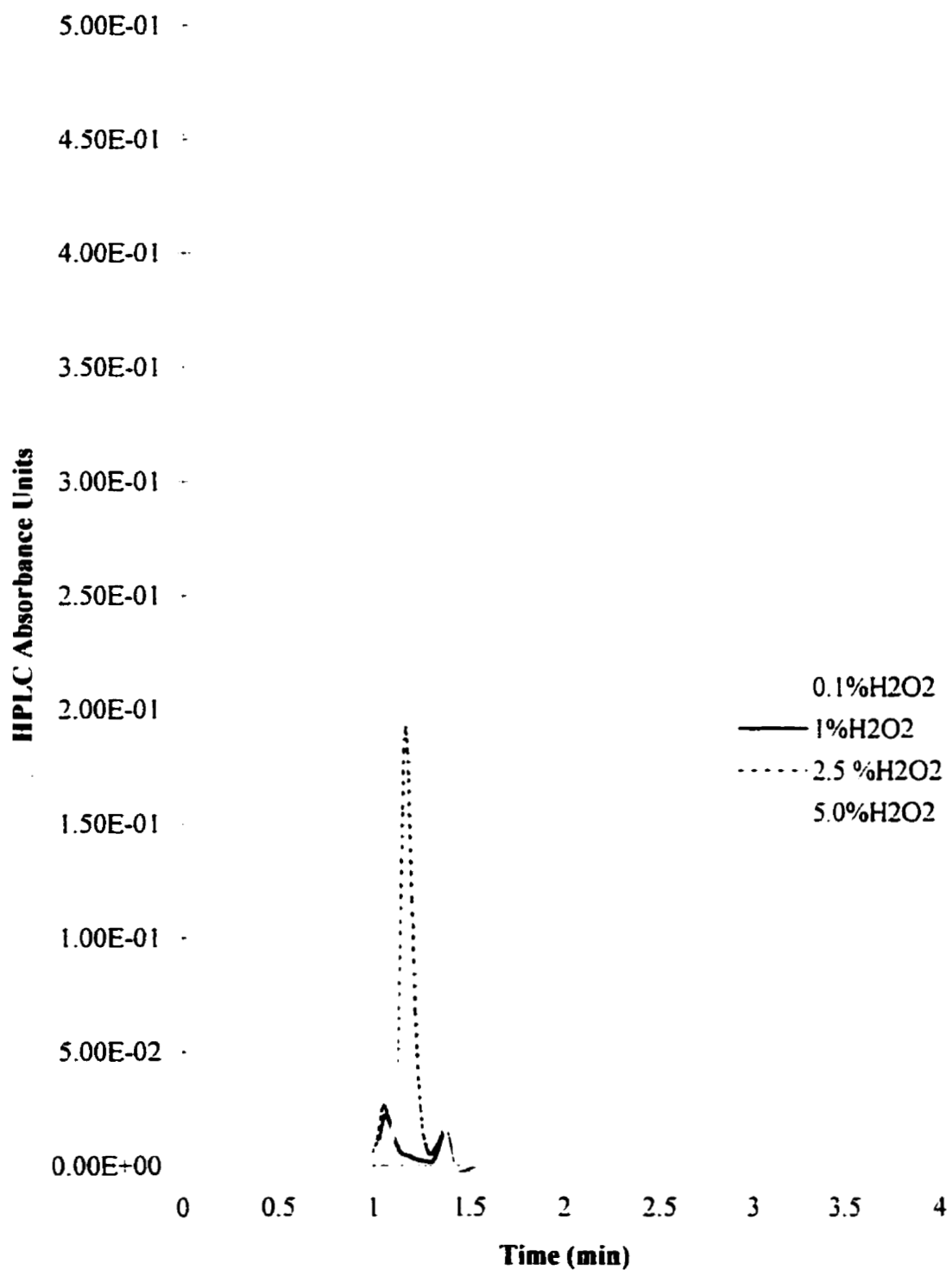


**Fig. 6-7.** HPLC Chromatograms Showing Photolysis Products of MWW under Rotating Irradiation with UC-210 and different% H<sub>2</sub>O<sub>2</sub> after 8 days.

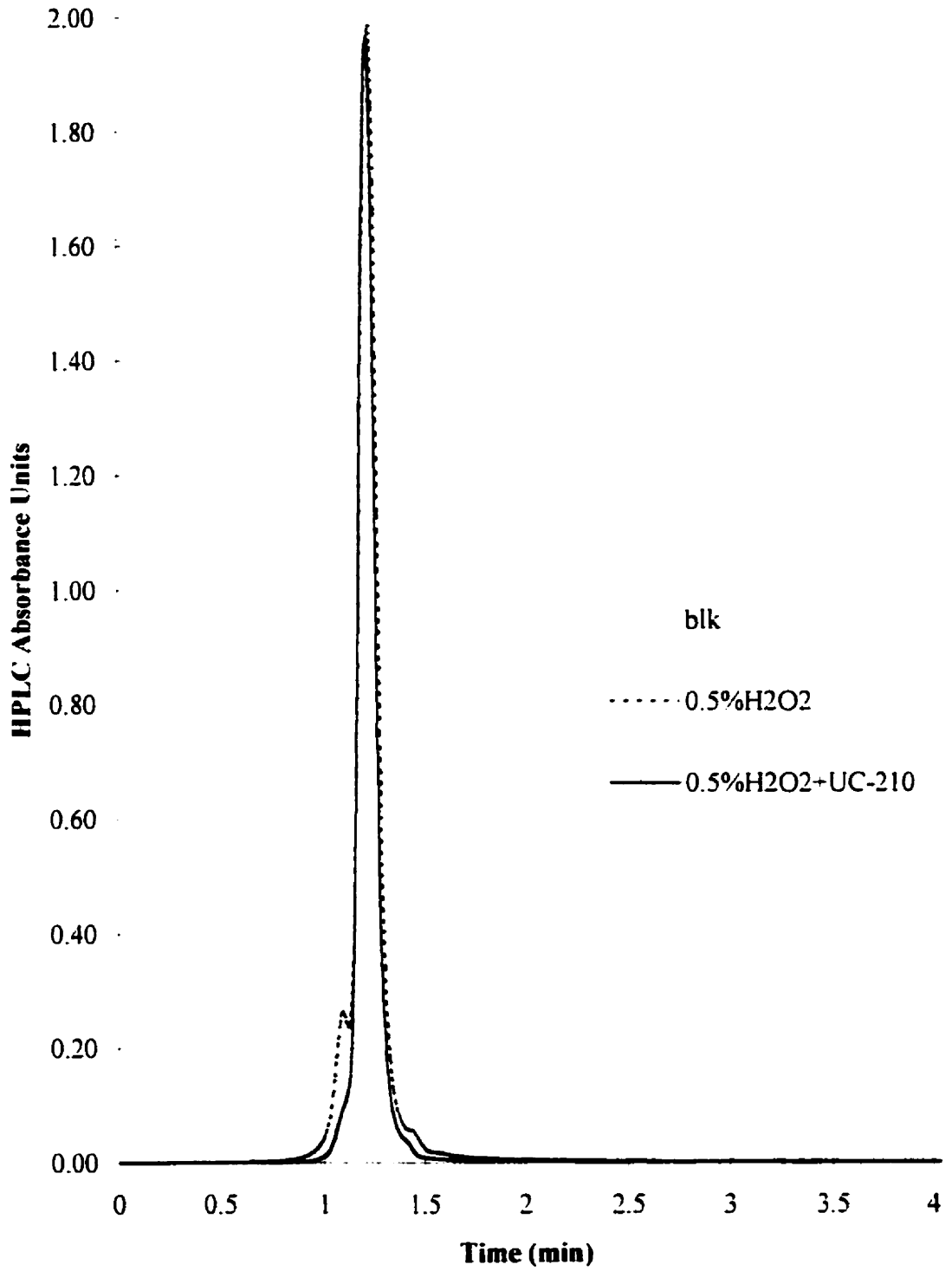


**Fig. 6-8.** HPLC Chromatograms Showing Photolysis Products of MillWW with 0.5g UC-210 and everyday injections of 0.5% H<sub>2</sub>O<sub>2</sub> after 4 days under Rotating Irradiation.

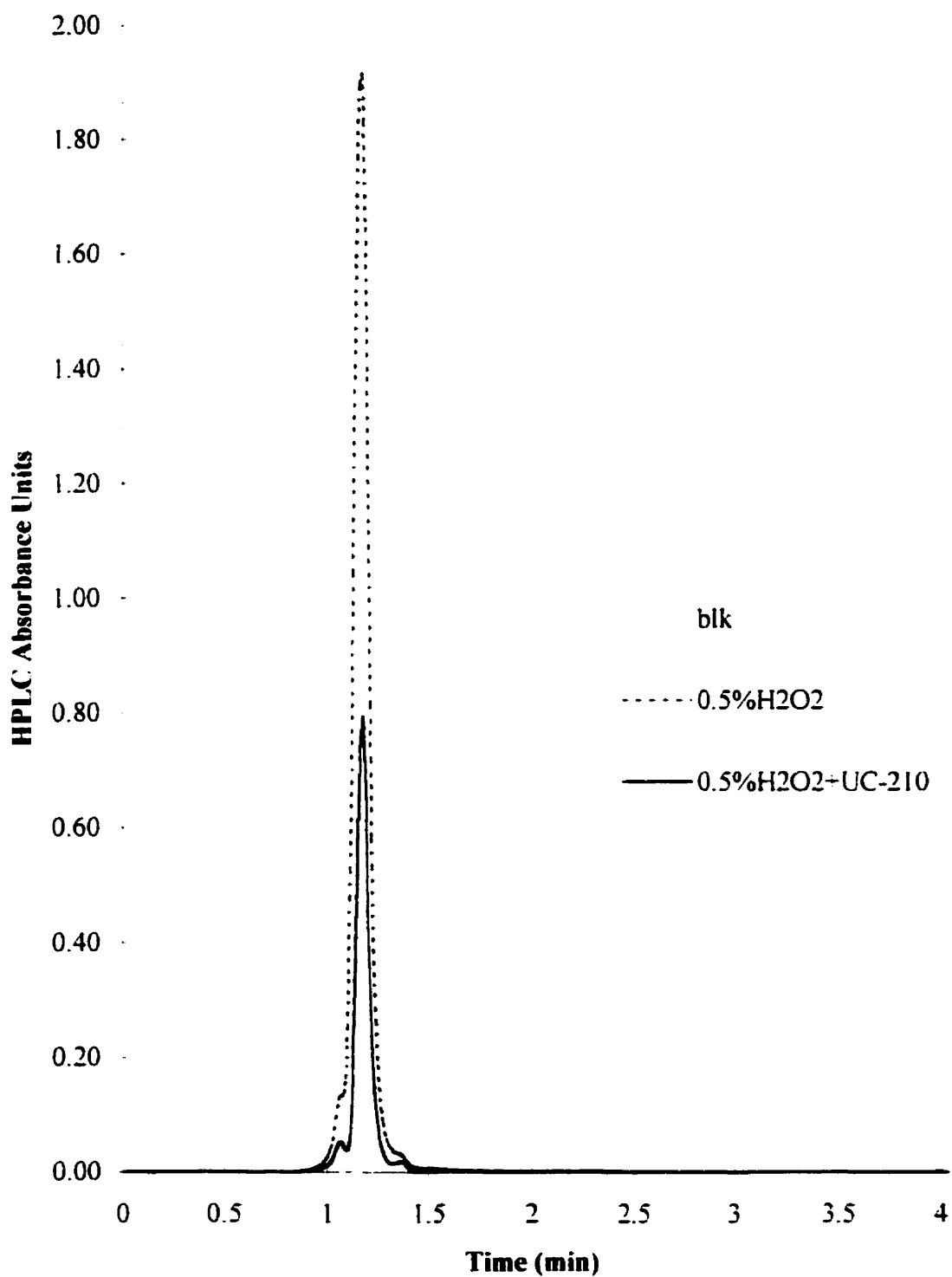


**Fig. 6-9.** HPLC Chromatograms Showing Photolysis Products of MW with 0.5g UC-210 and everyday injections of 0.5% H<sub>2</sub>O<sub>2</sub> for the first 4 days and without injections for the last 4 days under rotating irradiation.

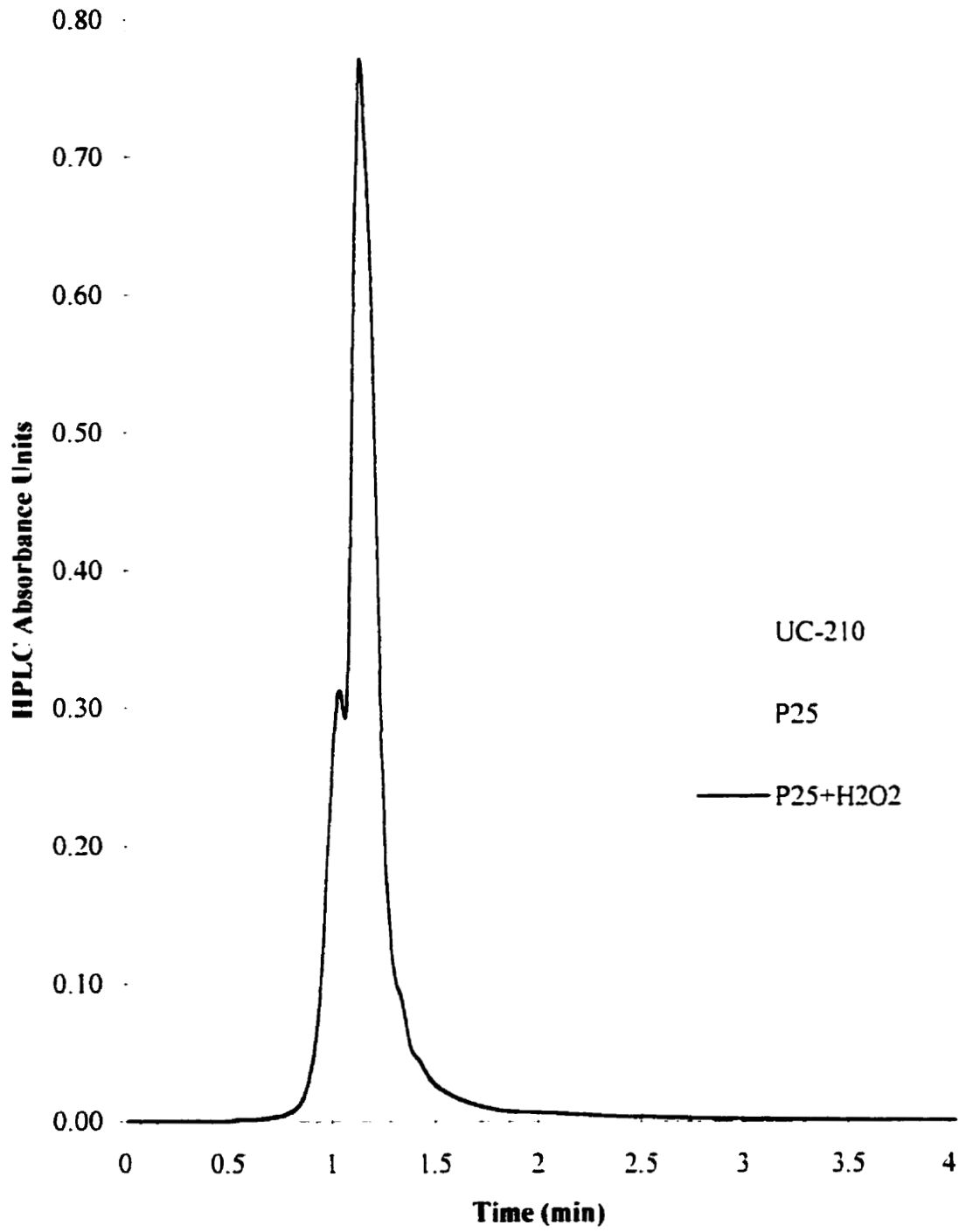


**Fig. 6-10.** HPLC Chromatograms Showing Photolysis Products of MWW with 0.2g UC-210 or Degussa P25 and 0.5% H<sub>2</sub>O<sub>2</sub> after 2 days under Rotating Irradiation .

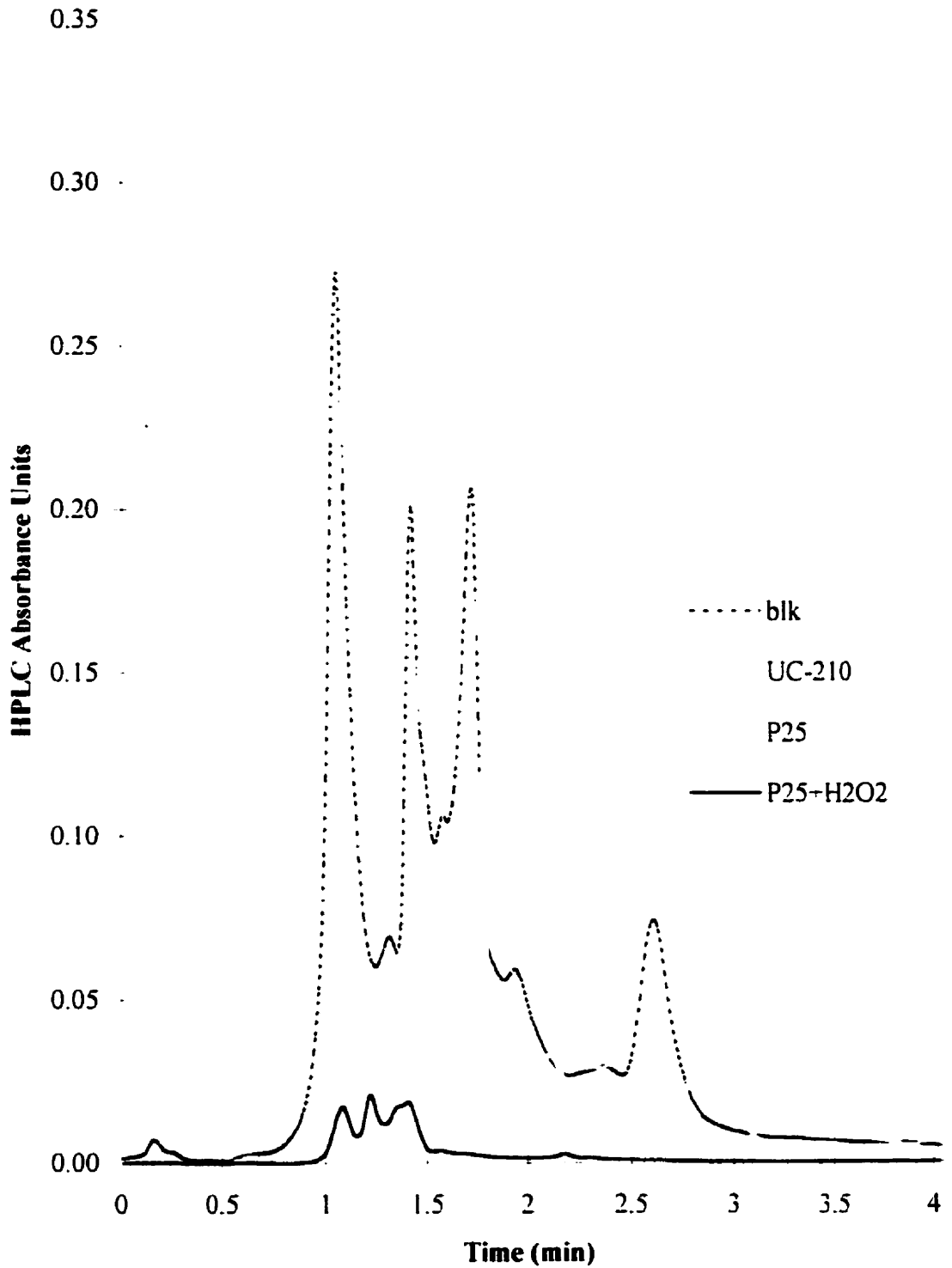


**Fig. 6-11.** HPLC Chromatograms Showing Photolysis Products of MWW with 0.2g UC-210 or Degussa P25 and 0.5% H<sub>2</sub>O<sub>2</sub> after 11 days under Rotating Irradiation .

## Chapter Seven

### CONCLUSION

Loading of  $\text{TiO}_2$ , as little as 2.5 wt. %, on the zeolite ZSM-5 produced a photocatalyst of efficiency competitive with the best commercial  $\text{TiO}_2$  used in the quantity similar to the total catalyst weight of titania in ZSM-5<sup>115</sup>. Successful manipulation of such system required further elucidation of high titania activity at a low loading level. In the present work, the photocatalytic activity of titanium oxide supported on the highly siliceous zeolites from ZSM-5 family is correlated with the physical characteristics of the composite photocatalyst such as the nature of bonding between  $\text{TiO}_2$  and a zeolite surface; the character and structure of a photoactive site; and the distribution of photocatalytic sites over the particle.

The physical state of the titanium oxide supported on ZSM-5 zeolites is characterized by Solid State Nuclear Magnetic Resonance Spectroscopy, Energy Filtered Transmission Electron Microscopy, Scanning Electron Microscopy, X-ray Diffraction, and BET surface area measurement.

Comparison of 90° pulse  $^{29}\text{Si}$  MAS NMR spectra with  $^1\text{H}$  -  $^{29}\text{Si}$  CP-MAS spectra allows measurement of -OH groups, displaced from the zeolite surface by Si-O-Ti chemisorption. The coverage by 2.5 wt. %  $\text{TiO}_2$  is 16-18% of the BET surface area. A theoretical monolayer of anatase  $\text{TiO}_2$  loaded to 2.5 wt. % was calculated to cover 10% to 20% of the BET surface depending upon the orientation of the anatase unit cell. Loading  $\text{TiO}_2$  above 2.5 wt. % leads to further growth of the titania phase without further -OH displacement and increase of the coverage of the surface until the critical loading level is achieved. Energy filtered TEM shows that  $\text{TiO}_2$  growth occurs at irregularities on the ZSM-5 surface.

Photodegradation of acetophenone is chosen as a test reaction for the investigation of the photocatalytic activity of the composite photocatalysts. The rate of the reaction is found to be independent of the loading levels of  $\text{TiO}_2$  but variable with different initial acetophenone concentrations. Secondary photolysis caused reagent-

product competition for active sites on the surface of the zeolite and, thus, contributed to the overall rate of the acetophenone photodegradation.

The zeolites chosen for this work have large adsorptivity for acetophenone and their adsorption capacities increase with the increase of  $\text{SiO}_2/\text{Al}_2\text{O}_3$  ratio. The adsorption capacity of the zeolite ZSM-5 ( $\text{SiO}_2/\text{Al}_2\text{O}_3=50$ ) reaches its limit at the concentration of  $10^{-4}$  mol/L which correspond to 35% coverage of the BET surface of the zeolite.

A consistent interpretation can be given for the CP-MAS NMR, EFTEM, XRD, BET, HPLC, and GC data. Titanium dioxide is found to be chemically bound to the surface of ZSM-5 via elimination of -OH between the surface of  $\text{TiO}_2$  and the zeolite. Titania does not distribute evenly or randomly over the surface.  $\text{TiO}_2$  growth is preferentially anchored at specific defect sites on the support. When the loading exceeds 2.5 wt. %  $\text{TiO}_2$ , a phase with anatase like structure at least over short range, grows.

The remarkable photochemical characteristics of the  $\text{TiO}_2$  film, covering no more than 20% of the zeolite surface with a single unit cell thickness, is its capacity to harvest all the photons entering a reactor with this catalyst loading despite the fact that this loading includes much less  $\text{TiO}_2$  than is required to harvest all photons when the photocatalyst is  $\text{TiO}_2$  alone<sup>1,15</sup>. The plausible explanation is that the zeolite particles with very low absorbance ( $\sim 0$ ) for 350 nm photons scatter the photons among the particles until absorbance by  $\text{TiO}_2$  can occur. Scattering minimizes loss from the irradiated zone.

Present research, based on  $\text{TiO}_2$  photocatalysis, is applied for the treatment of streams in pulp and paper processing. The experiments demonstrate that the specially designed UC-210 catalyst can produce almost complete photodegradation of organic matter (up to 93%) in Mill White Water achieved after 6 days at an average light intensity of  $4 \times 10^{-8}$  einsteins /s corresponding to approximately 10 hours of sun exposure on a sunny day. Color reduction can also be achieved. Our concept encompasses both independent use of  $\text{TiO}_2$  photocatalysis and use of it as a supplement to conventional biological treatment processes.

## References

### Chapter One

- 1.1. Environment Canada at <http://www.ec.gc.ca/water/index.htm> (August, 1999).
- 1.2. Wise, D. L., and Trantolo, D.J. *Process Engineering for Pollution Control and Waste Minimization*, Marcel Dekker, Inc. New York, 1994.
- 1.3. Peterson, D., Watson, D., and Winterlin, W., *Journal of Environmental Science and Health*, B, 1988, 23, 587.
- 1.4. Venkatardi, R., Peters, R.W., *Hazard. Waste Hazard. Mater.* 1993, v.10, No. 2, 107.
- 1.5. Hidaka, H., and Zhao, J. *Colloids and Surfaces*, 1992, 67, 165.
- 1.6. Richardson, S.D., Thruston, A.D., Collette, T.W., Patterson, K.S., Lykins, B.W., Ireland, J.C. *Environ. Sci. Technol.*, 1996, v.30, No. 11, 3327.
- 1.7. Vogelpohl, A., Geissen, S.U. *Water Sci. Technol.* 1997, v.35, No.4, 273.
- 1.8. Gupta, H., Tanaka, S. *Water Sci. Technol.* 1995, v.31, No. 9, 47.
- 1.9. Lepore, G.P., Persaud, L., and Langford, C.H. *J Photochem. Photobiol.*, A, 1996, 1.
- 1.10. Lepore, G.P., Pant, B.C., and Langford, C.H. *Can. J. Chem.*, 1993, 71, 2051.
- 1.11. Matthews, R.W. *Res. Water*, 1991, 25, 1169.
- 1.12. Anpo, M., Nakaya, H., Kodama, S., Kubokama, Y., Domen, K., Onishi, T., *J. Phys. Chem.* 1986, 90, 1633.
- 1.13. Yoneyama, H., Haggaa, S., Yamanaka, S. *J. Phys. Chem.* 1989, 93, 4833.
- 1.14. Yamashita, H., Honda, M., Harada, M. *J. Phys. Chem.* 1998, 102, 10707.
- 1.15. Xu, Y. and Langford, C.H., *J. Phys. Chem.* 1995, 99, 11501.
- 1.16. Xu, Y. and Langford, C.H., *J. Phys. Chem.* 1997, 101, 3115.
- 1.17. Lipmaa, E., Magi, M., Samoson, A., Tarmak, M., and Engelhardt, G. *J. Amer. Chem. Soc.* 1981, 103, 4992.
- 1.18. Carr, S.W. *Chem. Mater.* 1997, 9, 1927.
- 1.19. Hendzel, M.J. and Bazett-Jones, D. P. *Journal of Microscopy*, 1995, 182, 1.
- 1.20. Ottensmeyer, F.P. *J. Ultrastruct. Res.* 1984, 88, 121.

**Chapter Two**

- 2.1. Schiavello, M., Eds. *Heterogeneous Photocatalysis*; John Wiley & Sons Ltd. New York, 1997.
- 2.2. Howe, R.F., and Gratzel, M. *J. Phys. Chem.* **1987**, *91*, 3906.
- 2.3. Jaeger, C.C., and Bard, A.J. *J. Phys. Chem.* **1979**, *83*, 3146.
- 2.4. Ceresa, E.M., Burlamacchi, L., and Visca, M. *J. Mater. Sci.* **1983**, *18*, 289.
- 2.5. Turchi, C.S., Ollis, D. *J. of Catalysis*, **1990**, *122*, 178.
- 2.6. Izumi, I., Dunn, W.W., Wilbourn, K.O., Fan, F.-R., and Bard, A.J. *J. Phys. Chem.*, **1980**, *84*, 3207.
- 2.7. Hashimoto, K., Kawai, T., and Sakata, T. *J. Phys. Chem.*, **1984**, *88*, 4083.
- 2.8. Matthews, R.W. *J. Chem. Soc. Faraday Trans. I*, **1984**, *80*, 457.
- 2.9. Al-Ekabi, H., and Serpone, N. *J. Phys. Chem.*, **1988**, *92*, 5726.
- 2.10. Matthews, R.W. *J. Catal.* **1988**, *11*, 264.
- 2.11. Cunnigham, J., and Al-Sayyed, G. *J. Chem. Soc. Faraday Trans.* **1990**, *86 (23)*, 3935.
- 2.12. Cunnigham, J., and Srijaranai, S. *J. Photochem. Photobiol. A: Chem*, **1991**, *58*, 361.
- 2.13. Chen, H.Y., Zahraa, O., Bouchy, M., Thomas, F., and Bottero, J.Y. *J. Photochem. Photobiol. A: Chem*, **1995**, *85*, 179.
- 2.14. Emeline, A.V., Rudakova, A.V., Ryabchuk, V.K., and Serpone, N. *J. Phys. Chem. B*, **1998**, *102*, 10906.
- 2.15. Harris, R.K. *Nuclear Magnetic Resonance Spectroscopy; A physiochemical view*, Longman Science & Technical, Essex, England, **1986**.
- 2.16. Drago, R.S., *Physical Methods in Chemistry*, W.B. Saunders Company, Philadelphia, **1977**.
- 2.17. Abraham, R.J., and Loftus, P. *Proton and Carbon-13 NMR Spectroscopy: An Integrated Approach*, Heyden and Son Ltd. Great Britain, **1978**.
- 2.18. Sanders, J.K.M., and Hunter, B.K. *Modern NMR Spectroscopy; A guide for Chemists*, Oxford University Press, New York, **1993**.

- 2.19. Hennel, J.W., and Klinowski, J. *Fundamentals of Nuclear Magnetic Resonance*, Longman Scientific and Technical, UK, 1993.
- 2.20. Shaw, D. *Fourier Transform NMR Spectroscopy*, Elsevier, New York, 1976.
- 2.21. Benn, R., and Günter, H. *Angew. Chem. Int. Ed. Engl.* 1983, 22, 350.
- 2.22. Fyfe, C.A. *Solid State NMR for Chemists*, C.F.C. Press, Guelph, Ontario, 1983.
- 2.23. Engelhardt G. and Michel, D. *High-Resolution Solid State NMR of Silicates and Zeolites*; Wiley: Chichester, England, 1987.
- 2.24. Ernst, R. *Bulletin of Magnetic Resonance*, 1992, 16, 5.
- 2.25. Stejskal, E.O., and Memory, J.D. *High Resolution NMR in the Solid State*, Oxford University Press, New York, Oxford, 1994.
- 2.26. Marks, D., and Vega, S. *J. Magn. Reson. Ser. A* 1996, 118, 157.
- 2.27. Goldman, M. *Spin Temperature and Nuclear Magnetic Resonance in Solids*, Clarendon Press, Oxford, UK, 1970.
- 2.28. *Introduction to Analytical Electron Microscopy*, Eds.: Hren, J.J., Goldstein, J.I., and Joy, D.C., Plenum Press, New York and London, 1979.
- 2.29. Crozier, P.A., *Ultramicroscopy* 1995, 4, 157. Crozier 96 -17

### Chapter Three

- 3.1. Fyfe, C.A., Gies, H., Kokotailo, G.T., Pasztor, C., Strobl, H., and Cox, D.E. *J. Am. Chem. Soc.* 1989, 111, 2470.
- 3.2. Engelhardt G., Lohse, U., Samoson, A., Magi, M., Tarmak, M., and Lipmaa, E. *Zeolites*, 1982, 2, 59.
- 3.3. Fyfe, C.A., Thomas J.M., Klinowski, J., and Gobbi, G.C. *Angew. Chem. Int. Ed. Engl.* 1983, 22, 259.
- 3.4. Dessau, R.M., Schmitt, K.D., Kerr, G.T., Woolery, G.L., and Alemany, L.B. *J. Catal.* 1978, 104, 484.
- 3.5. Meinhold, R.H. and Bibby, D.M. *Zeolites*, 1990, 10, 74.
- 3.6. Pruski, M. dela Rosa, L., and Gerstein, B.C. *Energy Fuels*, 1990, 4, 160.
- 3.7. Adamson, A.W. *Physical Chemistry of Surfaces*, 5<sup>th</sup> Ed., J. Wiley & Sons, New York, 1990, Chap.XVI.

- 3.8. Sindorf, D.W., and Maciel, G.E. *J. Phys. Chem.* **1982**, *86*, 5208.
- 3.9. Starke, P., Trettin, R., and Grimmer, A.-R. *Z. Chem.* **1986**, *26*, 114.
- 3.10. Starosud, A., Bazett-Jones, and D. P., Langford, C.H. *Chem. Commun.* **1997**, *1*, 443.
- 3.11. JCPDS-international Centre for Diffraction Data, **1996**.

#### Chapter Four

- 4.1. Jalava, J.P., Heikkila, L., Hovi, O., Laiho, R., Hiltunen, E., Hakanen, A., and Harma, H. *Ind. Eng. Chem. Res.* **1998**, *37*, 1317.
- 4.2. Lepore, G.P. *Titanium Dioxide Photocatalysis*. Ph.D Thesis. The University of Calgary, **1994**.
- 4.3. Crozier, P.A. and McCartney, M.R. *J. Catal.*, **1996**, *163*, 245.
- 4.4. Taylor, D.E., Walter, E.G., Sherburne, R., and Bazett-Jones, D. P. *J. Ultrastruct. Res.*, **1988**, *99*,18.

#### Chapter Five

- 5.1. D., Sawyer, J.Jr., Roberts, *Experimental Electrochemistry for chemists*, John Wiley, **1974**.
- 5.2. Lepore, G.P., Pant, B.C., and Langford, C.H. *Can. J. Chem.* **1993**, *71*, 2051

#### Chapter Six

- 6.1. Zhang, X., Cai, Y., Stebbings, D., Beatson, R.P., and Saddler, J.N. *In Enzymic Degradation of Insoluble Carbohydrates*, Eds. Saddler, John N.; Penner, Michael H., ACS: Washington, D.C., Eng. **1995**, C151.
- 6.2. Orsa, F., and Holmbom, B. *J. Pulp Paper Sci.*, **1994**, *20(12)*, J361.
- 6.3. de Jong, E., Wong, K.K.Y., and Saddler, J.N. *The Mechanism of Xylanase Prebleaching of Kraft Pulp: An Examination Using Model Pulps Prepared by Depositing Lignin and Xylan on Cellulose Fibers*. *Holzforchung*, **1997**, *51(1)*, 19.
- 6.4. Shoemaker, D.P., Garland, C.W., Stinfield, J.I., and Nibler, J.W. *Experiments in Physical Chemistry*, 4-th ed., McGraw-Hill, New York. **1981**, 329.

## APPENDIX

### Parameters

Specific surface area of ZSM-5:	$s_{ZSM-5} = 315 \text{ m}^2/\text{g}$
Loading of ZSM-5	$m_{ZSM-5} = 2 \text{ g/L}$
Specific surface area of acetophenone	$s_{AP} = 3.7 \cdot 10^{-19} \text{ m}^2 \text{ per molecule}$
Concentration of acetophenone	$C = 1 \cdot 10^{-3} \text{ mole/L (130 ppm)}$
Avogadro's Number	$N_A = 6.023 \cdot 10^{23} \text{ mol}^{-1}$
Molecular weight of $\text{TiO}_2$	$M_{\text{TiO}_2} = 80 \text{ g/mole}$
Loading of $\text{TiO}_2$	$m_{\text{TiO}_2} = 0.025 \text{ g per 1 g of ZSM-5}$
Anatase unit dimensions	$a = 4A^{\circ} \quad b = 4A^{\circ} \quad c = 9A^{\circ}$

### 1. Estimation of Titanium Dioxide on the Surface of ZSM-5

Surface area of $\text{TiO}_2$ unit cell (short facet)	$s^1_{\text{TiO}_2} = 1.6 \cdot 10^{-19} \text{ m}^2$
Surface area of $\text{TiO}_2$ unit cell (long facet)	$s^2_{\text{TiO}_2} = 3.6 \cdot 10^{-19} \text{ m}^2$
Number of $\text{TiO}_2$ particles	$N = m_{\text{TiO}_2} \cdot N_A / M_{\text{TiO}_2} = 1.9 \cdot 10^{20} \text{ g}^{-1}$
Surface area of $\text{TiO}_2$ (short facet)	$S^1_{\text{TiO}_2} = s^1_{\text{TiO}_2} \cdot N = 30.4 \text{ m}^2/\text{g}$
Surface area of $\text{TiO}_2$ (long facet)	$S^2_{\text{TiO}_2} = s^2_{\text{TiO}_2} \cdot N = 68.4 \text{ m}^2/\text{g}$
% coverage of ZSM-5 by $\text{TiO}_2$ (short facet)	$(S^1_{\text{TiO}_2} / s_{ZSM-5}) \cdot 100\% = 10\%$
% coverage of ZSM-5 by $\text{TiO}_2$ (long facet)	$(S^2_{\text{TiO}_2} / s_{ZSM-5}) \cdot 100\% = 21\%$

### 2. Estimation of Acetophenone on the Surface of ZSM-5

Surface area of ZSM-5	$S_{ZSM-5} = s_{ZSM-5} \cdot m_{ZSM-5} = 630 \text{ m}^2/\text{L}$
Surface area of acetophenone	$S_{AP} = s_{AP} \cdot C \cdot N_A = 223 \text{ m}^2/\text{L}$
% coverage of ZSM-5 by acetophenone	$(S_{AP} / S_{ZSM-5}) \cdot 100\% = 35\%$